Investigation of Coherent Structures in Unsteady Car Aerodynamics

Martin Alexander Peichl

TECHNISCHE UNIVERSITÄT MÜNCHEN
Fakultät für Maschinenwesen
Lehrstuhl für Aerodynamik und Strömungsmechanik

Investigation of Coherent Structures in Unsteady Car Aerodynamics

Martin Alexander Peichl

Vollständiger Abdruck der von der Fakultät für Maschinenwesen der Technischen Universität München zur Erlangung des akademischen Grades eines

Doktor-Ingenieurs (Dr.-Ing.)

genehmigten Dissertation.

Vorsitzender:		Prof. Dr.-Ing. Veit St. Senner
Prüfer der Dissertation:	1.	Priv.-Doz. Dr.-Ing. habil. Thomas Indinger
	2.	Prof. Makoto Tsubokura, Ph.D. Kobe University, Japan

Die Dissertation wurde am 05.04.2019 bei der Technischen Universität München eingereicht und durch die Fakultät für Maschinenwesen am 04.09.2019 angenommen.

Martin Peichl
Chair of Aerodynamics and Fluid Mechanics
Technical University of Munich
Boltzmannstr. 15
85748 Garching bei München
Germany

© Martin Peichl, 2019

All rights reserved. No part of this publication may be reproduced, modified, re-written, or distributed in any form or by any means, without the prior written permission of the author.

Typesetting LaTeX

To Judith

Abstract

A distinguishing characteristic of the flow around cars are large-scale coherent structures. Understanding the interactions of structures in the flow promises a considerable potential for aerodynamics optimizations. In this thesis, selected methods are assessed for their capability to identify coherent structures in simulation data and to describe interactions of structures. The methods are assessed theoretically and adapted for an application in car aerodynamics where necessary. The most suitable methods are applied to four test cases of different complexity and realism: The first test case is a cube mounted on the surface of a channel. The second test case is composed of variants of the SAE body, a highly simplified generic vehicle geometry. The third test case is the DrivAer body, a detailed generic vehicle body. And the fourth case analyses a convertible type car geometry based on a production car.

It was shown that none of the classical vortex detection methods under investigation – *Q-Criterion*, Δ-*Criterion*, λ_2-*Criterion*, λ_{ci}-*Criterion* and *Shear Maximizing Decomposition* (also called *Triple Decomposition of Motion*) – is well suited for the investigation of unsteady car aerodynamics flow fields. The modal decompositions under investigation – *Proper Orthogonal Decomposition* (POD) and *Dynamic Mode Decomposition* (DMD) – are shown to be applicable in the investigation of unsteady car aerodynamics flow fields. With the proposed pre and post-processing, the DMD was found to be best suited for the investigation of unsteady coherent structures as well as for the investigation of their interactions.

Acknowledgments

I would like to thank Priv.-Doz. Dr.-Ing. habil. Thomas Indinger and Prof. Dr.-Ing. Nikolaus A. Adams for the opportunity to carry out my doctoral research project at the Chair of Aerodynamics and Fluid Mechanics of Technical University of Munich. I would also like to thank Prof. Makoto Tsubokura for the scientific exchange during the project and for taking the role of external reviewer. I would like to thank my former colleagues at the Chair of Aerodynamics and Fluid Mechanics most notably Steffen Mack, Muzio Grilli, Lukas Haag, Michael Gestrich, Aaron Endres, Daiki Matsumoto, Marco Kiewat, Simon Huber, Angelina Heft, Bastian Schnepf, Christopher Collin, Daniel Gaudlitz, Patrick Nathen, Volker Tritschler and Felix Diegelmann for their support, the scientific discussions and the encouraging atmosphere.

I would like to express my gratitude to my industry partner AUDI AG especially Dr. Moni Islam and Dr. Gerhard Wickern for their assistance and financial support.

The author also gratefully acknowledges the Gauss Centre for Supercomputing e.V. for funding this project by providing computing time on the GCS Supercomputer SuperMUC at Leibniz Supercomputing Centre.

Table of contents

List of Figures

List of Tables

1 Introduction

Substantial progress in the aerodynamic drag reduction of vehicles is becoming increasingly difficult. The potential of the classical method of optimizing individual parts of the vehicle like the optimization of the car underbody, the wheels, the side mirrors etc. is largely exploited. While the focus of research in car aerodynamics has shifted in parts to an optimization of the iterative development process to allow for a faster development, one of the most important unsolved questions of car aerodynamics is the complex aerodynamic interaction of local flow phenomena.

To investigate the local flow mechanisms and their interactions, selected methods are assessed for their capability to detect coherent structures in simulation data and to characterize their interactions. Proposed modifications and extensions to methods not currently used in car aerodynamics allow for their application in the aerodynamics development process.

1.1 Methodology

Due to limited computing resources and a lack of efficient unsteady simulation solutions as well as a lack of efficient unsteady measurement technics, the car aerodynamics de-

velopment of the past was concentrated on a rough optimization of the car shape and a largely independent optimization of individual parts of the vehicle. As a consequence, unsteady phenomena as well as the interactions of local flow phenomena were usually not taken into account. With the need of a higher degree of aerodynamic optimization and the availability of advanced unsteady simulation technics, unsteady simulations became a standard method in the car development leading to a high accuracy of simulation results and the possibility to investigate the unsteady flow.

Most of the methods to investigate structures in flow fields currently in use in car aerodynamics are not targeted to the investigation of complex unsteady flow phenomena and interactions. In this thesis, the classical and most commonly used methods to identify vortices in flow field data – Q-Criterion, Δ-Criterion, λ_2-Criterion and λ_{ci}-Criterion – are reassessed. In addition, a less well known classical vortex detection method, the so called Triple Decomposition of Motion is assessed. Applied as methods to identify and study interactions of unsteady flow phenomena, the Proper Orthogonal Decomposition (POD) and the Dynamic Mode Decomposition (DMD) are investigated in detail.

1.1.1 Challenges

The turbulent flow around a car shaped body is made up of distinguished features that form connected regions, the so called *coherent structures*. The coherent structures in the flow around a car are three dimensional, usually unsteady and exist in a wide range of time and length scales. The structures interpenetrate and interact with each other. While some large and time independent structures can be localized relatively easily and are characteristic for the flow of a wide range of different car shapes, the vast majority of structures are more difficult to identify and can change considerably with small changes of the car geometry. Although these structures are usually smaller and lower in energy than the dominant structures, they can have a strong influence on the overall flow by interacting with the dominant structures. With a successively more detailed aerodynamic optimization, the low energy structures and their interactions with the structures of high energy are becoming increasingly more important. It is not uncommon that investigations of isolated local flow phenomena lead to considerably different results when repeated with slightly changed geometries or boundary conditions. An isolated optimization of individual parts of the geometry does not converge towards the global optimum and the optimization of the complete geometry leads to an exponentially increasing number of geometry variants due to the aerodynamic interaction of the different parts. Selecting the parameters for wind tunnel optimization based on the knowledge of interactions could considerably reduce the number of geometry variants necessary and allow for a faster and more detailed aerodynamic optimization.

1.1.2 Approach

One of the most successful approaches in car aerodynamics research is the usage of simplified, generic vehicle shapes. Highly simplified, generic vehicles like the *Ahmed Body* (Ahmed et al. [1]) or the *SAE Body* (Cogotti [19]) have been used in the past to study fundamental flow phenomena common to a certain class of car geometries. While these geometries were useful in the investigation of fundamental flow phenomena, they cannot be used in the investigation of the aerodynamic details of production cars. To overcome this restriction another class of generic vehicle geometries has been employed the so called realistic generic vehicles. A representative of this class of generic vehicles is the *DrivAer Body* (Heft et al. [38], Mack et al. [68]). The DrivAer Body resembles a typical midsized passenger car and is geometrically derived from two production vehicles – the *Audi A4* (B8, since 2007) and the *BMW 3 series* (E90/91, since 2005) [39]. The realistic generic vehicle models are especially suited for the investigation of aerodynamic interactions like the interaction of the flow through the engine compartment and the flow in the wheel houses. While the realistic generic geometries allow identifying the principles of the flow on a detailed level, the validity of findings is often limited to small changes in the geometry and therefore not generally transferable to production vehicles. As a consequence, studies on variants of generic car geometries become less relevant for flow phenomena of increasing complexity and nonlinearity.

An alternative to the identification of fundamental transferable flow phenomena in the flow around generic car geometries is a method-based approach. Instead of parameter studies with different simplified geometries, the topology of the flow around a single, fully detailed geometry is investigated. While the objective of investigations on generic vehicles is the identification of transferable mechanisms, the objective of the method-based approach is to identify the important mechanisms in the flow around one geometry without considering transferability to other geometries. The scientific progress is represented here by the capabilities of the method rather than by a description of a transferable phenomenon. This allows extending the subject of investigations to arbitrarily complex geometries and arbitrarily complex flows. Examples of studies following a method-based approach are the usage of adjoint methods for gradient-based optimization in car aerodynamics by Othmer [81], the investigations of the unsteady A-pillar vortex system using a *Proper Orthogonal Decomposition (POD)* of velocity and vorticity fields by Levy and Brancher [64] or the decomposition of the wake flow of a detailed generic car geometry with a *Dynamic Mode Decomposition (DMD)* by Peichl et al. [83]. While the adjoint methods give a direct measure of the sensitivity to geometry modifications, the application of reduced order models and decompositions, such as the POD or the DMD, allow isolating individual flow processes and their associated coherent structures from the flow field and providing information of relationships in the flow.

1.1.3 Implementation

Following the described method-based approach, this thesis investigates and adapts the capabilities of selected methods to be used in the car aerodynamics development process. The application of the methods is shown in four test cases of different complexity.

Methods In chapter 2, the methods used in this thesis are introduced and described. Alongside the numerical and experimental methods, the core methods for the identification of coherent structures are discussed and evaluated in detail. Proposed modifications to the methods are described and recommendations for their application are given.

Vortex Identification In chapter 2.4 of the thesis, requirements to vortex identification methods applied to automotive aerodynamics flow fields are formulated. The most popular vortex detection methods, *Q-Criterion*, Δ-*Criterion*, λ_2-*Criterion*, λ_{ci}-*Criterion*, as well as a less well known vortex detection method, the *Shear Maximizing Decomposition* (also called *Triple Decomposition of Motion*) are introduced.

The methods are first theoretically evaluated based on simple canonical flow examples and then applied to the flow around a car and analyzed based on the three tensors of the shear maximizing decomposition.

The methods can be shown to fail for some canonical flows or show false positives for others. It is concluded, that none of the investigated methods can be used for quantitative analyses of vortices in car aerodynamics.

Modal Decompositions In chapter 2.5 the Proper Orthogonal Decomposition (POD) and the Dynamic Mode Decomposition (DMD) are described and evaluated theoretically. The methods are implemented for fully distributed memory parallel processing to allow for an application to the entire vehicle flow field. The POD is introduced based on a Singular Value Decomposition. To account for ambiguous results due to the sign indeterminacy of the POD, an algorithm to estimate a physically meaningful sign is introduced.

The Dynamic Mode Decomposition according to Schmid [92] and Rowley et al. [89] is introduced and described in detail. To allow for an application of the DMD to car aerodynamics flow fields a pre-processing procedure is proposed. It is shown that the DMD analysis would fail for most car aerodynamics investigations without the proposed procedure.

A comparison of the Proper Orthogonal Decomposition with the Dynamic Mode Decomposition shows a superiority of the DMD for most applications in car aerodynamics.

Applications The methods introduced and assessed theoretically in chapter 2 are applied to test cases of different geometry complexity in the chapter 3. For each test case, the time averaged flow is investigated first. The dominant coherent structures of the time averaged flow are described in detail as a basis for the unsteady investigation. Subsequently, a detailed analysis of the unsteady flow is executed.

The applications are presented in the chapters 3.1 *Surface Mounted Cube*, 3.2 *SAE Car Model*, 3.3 *DrivAer Car Model* and 3.4 *Convertible Car Model*:

Surface Mounted Cube As a simple example of a bluff body flow, the flow around a cube mounted on the surface of a channel is analyzed. The results are compared to results from literature.

SAE Car Model In this test case, the SAE car body is investigated in four different configurations. Applying the DMD, an interaction of the wake flow with the struts of the test model can be shown.

DrivAer Car Model As an example of a realistic generic vehicle, the flow around the DrivAer body is studied. Here, a connection between the unsteady coherent structures in the flow and unsteady force fluctuations acting on the model is established by a DMD analysis of force and velocity fields.

Convertible Car Model The flow around an open roof convertible type car model is analyzed as an example of a detailed vehicle geometry. A flow oscillation found in previous wind tunnel tests could be isolated using the Dynamic Mode Decomposition. The oscillation could be explained as an interaction of the wake flow with the shear layer from the wind screen and the air in the passenger compartment.

1.2 Coherent Structures

While structures and organized motions were long apparent in flowing fluids, the concept of coherent structures as a scientific approach to explain the organized motion in a turbulent fluid flow can be traced back to the 1950s with the description of hairpin vortices in turbulent boundary layers by Theodorsen [104] (cited in, amongst others, Aubry et al. [4], Zhou et al. [112] or Elavarasan and Meng [27]). In the following years, a large number of mathematical methods and algorithms were proposed to describe coherent structures. Although considerable progress was made in the identification and description of coherent structures, a commonly accepted definition of coherent structures still does not exist. Instead, the identification schemes are progressively tailored to specific questions whereby the underlying mathematical model of the scheme serves as the definition of the coherent structure.

The most widely used schemes are vortex identifications schemes with the most popular schemes being the *Q-Criterion* (Hunt et al. [42]) and the λ_2-*Criterion* (Jeong and Hussain [47]). The *Proper Orthogonal Decomposition (POD)* (Lumley [66], Sirovich [96]) can be found to be used mainly in research projects. In addition to these, a multitude of specialized schemes and identification procedures can be found in the literature. An overview of identification schemes is given by Haimes and Kenwright [36], Roth [88], Jiang et al. [50], Pobitzer et al. [85], Kolář et al. [57], Haller [37] or Tu [106]. Comparisons of selected identification schemes were published in Bonnet et al. [10], Chakraborty et al. [13], Chen et al. [14] or Cucitore et al. [22]. In this thesis, identification schemes are investigated for their potential for car aerodynamics investigations. The Q-criterion(Hunt et al. [42]), Δ-criterion (Chong et al. [18]), λ_2-criterion (Jeong and Hussain [47]), λ_{ci}-criterion (Zhou et al. [112]) and a shear maximizing decomposition of the velocity gradient tensor (Kolář [55]) are investigated for time averaged flows around cars. The *Proper Orthogonal Decomposition (POD)* (Lumley [66], Sirovich [96]) and *Dynamic Mode Decomposition (DMD)* (Schmid [92], Rowley et al. [89]) are used to investigate unsteady flow fields.

Frame Dependence of Coherent Structures

Coherent structures, as connected regions of organized motion in a fluid, are inherently frame dependent. A coherent structure, characterized in one reference frame can be different or totally absent in another frame of reference. This effect is shown in Fig. 1.1 on a time averaged, two dimensional flow over a backward facing step. The flow in Fig 1.1a is shown in the frame of the geometry. The flow in Fig. 1.1b is shown in the frame of the bulk velocity. Structures, clearly visible in the frame of the geometry cannot be seen in the frame of bulk velocity due to the superposition of the flow field of the structure and the translational velocity relative to the frame of reference.

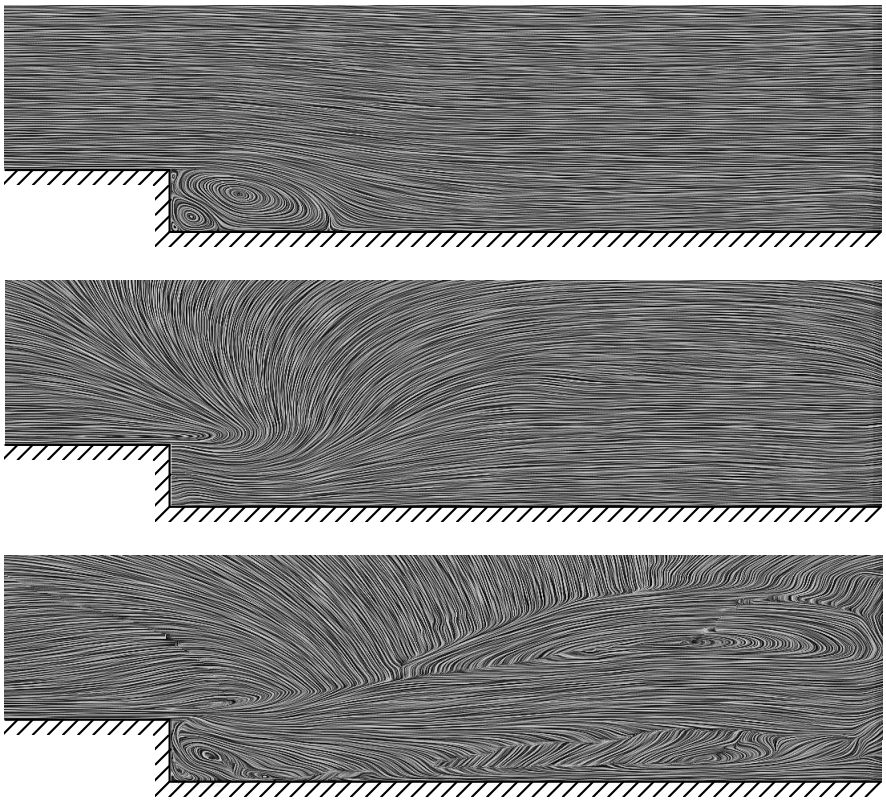

(a) Flow in the frame of the geometry.

(b) Flow in the frame of the bulk velocity.

(c) Orientation of simple shear (Galilean invariant).

Figure 1.1: Line Integral Convolution (LIC) of a time averaged, 2D flow over a backward facing step. Flow from left to right.

Due to the problem of frame dependence, most methods to identify coherent structures rely on Galilean invariant or frame-indifferent descriptions of the flow. In Fig. 1.1c the flow is visualized based on the orientation of simple shear, computed from a shear maximizing decomposition of the velocity gradient tensor (see section 2.4.2 for details). The orientation of simple shear is Galilean invariant and is able to show the vortices in the wake of the step as well as the vortex on top of the step. In addition to these, it shows a large vortex downstream the step that is not present in the above pictures. Although not objective, the method is able to detect coherent structures with different frames of reference.

Frame-indifference or *objectivity* in fluid mechanics is often discussed in the context of constitutive functions and material properties. The *principle of material frame-indifference* or *principle of material objectivity* was introduced by Truesdell and Noll in [105]. It was later formulated by Noll as:

> *"The constitutive laws governing the internal interactions between the parts of the system should not depend on whatever external frame of reference is used to describe them."* [76].

Noll distinguishes between internal and external frames and defines an internal frame as a frame that can be constructed from the system itself. This formulation of objectivity allows two approaches for a frame indifferent description of coherent structures. One is a description of the structure in its own frame of reference, while another approach is a description that produces the same result independent of the frame of reference and would therefore produce the same result in the internal frame of the coherent structure.

A single, isolated coherent structure can be fully described by both approaches. But in turbulent bluff body flows, as in car aerodynamics, coherent structures exist in cascades of interpenetrating structures of different time and length scales. In the turbulent wake flow of a bluff body, a multitude of coherent structures exist with different frames of reference at one point in time and space. An objective detection scheme of the second type that considers all coherent structures independent of coordinate system combines all structures at one point in time and space to one single result and will not be able to distinguish between the structures. Another conceptual problem of objective detection schemes of the second type is the fact that they cannot distinguish between a rigid body rotation in the flow field and a rotation of the reference frame. Objective detection schemes that consider all coherent structures independent of coordinate system therefore lend themselves more to the detection of the boundaries of coherent structures than to the description of the structures themselves.

Apart from the discussion of the necessity and usefulness of objective detection schemes for the detection of coherent structures, there is also an ongoing discussion about the principle of frame-indifference itself. Two of the latest contributions to this discussion are Frewer [29] and Liu and Sampaio [65]. Frewer gives a detailed historic review on the principle of material frame-indifference with a discussion of the most influential contributions and provides a framework for the mathematical formulation of material frame-indifference. Liu and Sampaio comment on the different concepts of frame-indifference and material frame-indifference.

Coherent structures in the flow around car geometries

Coherent structures in the flow around car geometries are, at least implicitly, subject of a large number of research papers. To give an overview of documented structures in the recent literature, papers are selected that focus more explicitly on the description of coherent structures around cars.

Steady and time averaged coherent structures

Starting point for investigations on the topology of the time averaged flow around the so called Ahmed body is the study of Ahmed et al. in [1]. Ahmed et al. experimentally

investigate the flow topology with pressure and velocity measurements in the wake as well as friction line visualizations using oil paint. Guilmineau [35] builds on this study with investigations of different rear slant angles using friction lines, velocity profiles and streamline visualizations of URANS simulations. Gilliéron et al. [33] investigate the formation of C-pillar vortices on the Ahmed body by a variation of the slant angle using static pressure tabs and friction line visualizations. Thacker et al. [103] investigate the effect of flow separation at the rear slant of the Ahmed body on the recirculation zone and the longitudinal C-pillar vortices employing PIV measurements in the wake of the geometry. Strachan et al. [102] study the influence of a moving ground on the vortical structures in the wake of an Ahmed body mounted on a model support system using Laser Doppler Anemometry (LDA). Krajnović [59] investigates the effect of vortex generators upstream the rear slant on the structures in the wake of the Ahmed body using plots of velocity, vorticity, Reynolds stresses, contours of the surface pressure coefficient and stream line visualizations of LES simulations. Vortical structures around a generic wheel in a wheelhouse are investigated by Regert and Lajos [86] using RANS and URANS simulations. The structures are visualized using a vortex skeleton method, isosurfaces of the second invariant of the velocity gradient tensor and isosurfaces of total pressure. Flow structures behind the front wheel arch and behind an antenna on the vehicle roof are studied by Bonitz et al. [9] on a detailed notchback geometry with a focus on their influence on flow separation using RANS simulations.

Unsteady coherent structures

Unsteady coherent structures around the Ahmed body are investigated by Vino et al. [107] using smoke flow visualization, surface oil flow visualization, unsteady surface pressure measurements and multi-hole, high frequency response pressure probe measurements. Krajnović and Davidson [61, 62] investigate the unsteady flow around the Ahmed body using LES simulations with special attention on the difference between the unsteady flow and the resulting time averaged flow. Wang et al. [108] use Particle Image Velocimetry (PIV) measurements to study the time averaged and unsteady flow in the near wake of the Ahmed body at different rear slant angles. Kohri et al. [52] study the vortex shedding at the rear of the Ahmed body at a critical rear slant angle of 30° using hot-wire measurements and Particle Image Velocimetry (PIV) measurements.

Hoarau et al. [40] investigate the unsteady behavior of the A-pillar vortex at a 30° slanted geometry using Laser Doppler Velocimetry (LDV) and surface pressure measurements. Levy and Brancher [64] study the flow around a similar geometry using Particle Image Velocimetry (PIV) measurements and Proper Orthogonal Decompositions (POD) to isolate the flow structures. Gilhome et al. [32] investigate a vortex shedding process from the rear of a generic notchback geometry using surface pressure measurements, skin friction visualization and smoke flow visualization. Peichl et al. [84] study the unsteady coherent

structures in the wake of a detailed generic notchback geometry employing a Dynamic Mode Decomposition (DMD) analysis on velocity fields of a Detached Eddy Simulation (DES). Fuller and Passmore [30] study the influence of C-pillar geometry on the wake topology of a simplified geometry of fastback type using surface pressure and Particle Image Velocimetry (PIV) measurements. Coherent structures around a smooth, isolated rotating wheel in contact with a moving ground are investigated by Croner et al. [21] with Particle Image Velocimetry (PIV) and URANS simulations. Structures in the wake of an external rear view mirror are investigated by Kim and Han [51] using hot-wire measurements and Laser Doppler Velocimetry (LDV) measurements.

In a joint two-part investigation, Okada et al. [77] and Nakashima et al. [75] study the influence of unsteady coherent structures on the straight-ahead driving stability of notchback type cars. Okada et al. conduct on-road and wind tunnel tests employing pressure measurements, hot-wire and Particle Image Velocimetry (PIV) measurements as well as force measurements and measurements of ride height changes. Nakashima et al. study the underlying mechanisms on a simplified notchback geometry employing LES simulations with different pitch angles and with a forced oscillating pitching motion. The effect of unsteady coherent structures on driving stability were subsequently studied in detail in a series of publications by Cheng et al. [15, 16, 17] on simplified and detailed notchback geometries.

2 Methods

The chapter on methods first introduces the definitions, basics and methodological approaches employed in the present work. It then discusses the core methods, evaluates their theoretical potential for car aerodynamics investigations and gives recommendations for their application in the car aerodynamics development process.

2.1 Definitions

Physical and mathematical quantities that are used throughout this work are briefly introduced in this chapter. Deviations from the definitions, given here, are indicated in the text.

The mathematical quantities – scalars, vectors and tensors – are indicated in the text as follows:

Scalars: Non-bold letters or symbols.

Vectors: Bold lowercase letters or symbols.

Tensors: Bold uppercase letters or symbols.

Car Coordinate System

The car coordinate system is a right handed Cartesian coordinate system with the positive x direction in the direction of the main flow and the positive z direction pointing upwards. The coordinate system is located, as shown in Fig. 2.1, with $x = 0$ symmetrically between front and rear axle, $y = 0$ symmetrically between the wheels and $z = 0$ on the ground.

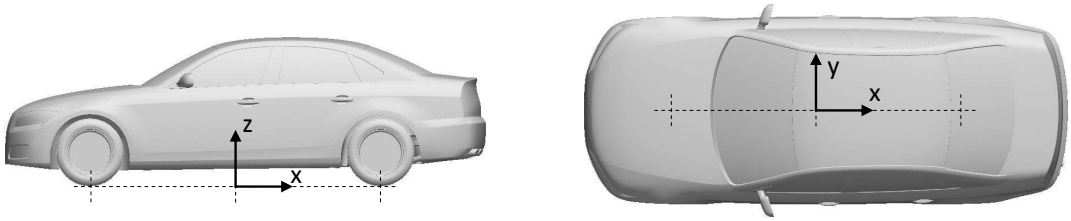

Figure 2.1: Position and orientation of the car coordinate system.

A positive drag force F_D points in positive x, a positive lift force F_L points in positive z direction. The Moments are defined as roll moment M_x around the x axis, pitch moment M_y around the y axis and yaw moment M_z around the z axis.

Dimensionless Numbers

Reynolds Number

The *Reynolds number* evaluates the ratio of inertial and viscous forces. With the characteristic length scale L, the characteristic velocity U and the kinematic viscosity ν:

$$Re = \frac{UL}{\nu}. \tag{2.1}$$

If not indicated otherwise, the Reynolds number is formed with the length of the car and the free stream velocity U_∞.

Strouhal Number

The *Strouhal number* is a non-dimensional measure of the frequency. The frequency f is non-dimensionalized with the characteristic length scale L and the characteristic velocity U:

$$Sr = f\frac{L}{U}. \tag{2.2}$$

If not indicated otherwise, the Strouhal number is formed with the free stream velocity U_∞.

Full Scale Frequency

The full scale frequency f^* resembles the frequencies as they would occur in a Reynolds similar, full scale flow. The frequency f in the flow around a model geometry with the scale factor ϕ is corrected according to the Strouhal similarity with the square of the scale factor ϕ.

$$f^* = f\phi^2 \tag{2.3}$$

Force coefficients

The *force coefficients* normalize the forces acting on the geometry. The forces are normalized by the dynamic pressure $\frac{\rho}{2}U_\infty^2$ and the frontal area A_x. The drag force coefficient c_D is computed with the drag force F_x, the side force coefficient c_S with the side force F_y and the lift force coefficient c_L with the lift force F_z:

$$c_{F,x} = c_D = \frac{F_x}{\frac{\rho}{2}U_\infty^2 A_x}, \qquad c_{F,y} = c_S = \frac{F_y}{\frac{\rho}{2}U_\infty^2 A_x}, \qquad c_{F,z} = c_L = \frac{F_z}{\frac{\rho}{2}U_\infty^2 A_x}. \tag{2.4}$$

Moment coefficients

The *moment coefficients* are the normalized moments acting on the geometry. The moments M_i are normalized by the dynamic pressure $\frac{\rho}{2}U_\infty^2$, the frontal area A_x and the wheelbase l_{wb} of the vehicle.

$$c_{M,x} = \frac{M_x}{\frac{\rho}{2}U_\infty^2 A_x l_{wb}}, \qquad c_{M,y} = \frac{M_y}{\frac{\rho}{2}U_\infty^2 A_x l_{wb}}, \qquad c_{M,z} = \frac{M_z}{\frac{\rho}{2}U_\infty^2 A_x l_{wb}}. \tag{2.5}$$

Pressure coefficient

The *pressure coefficient* c_p is the normalized difference between the local pressure p and the ambient pressure p_∞. The pressure difference is normalized by the free stream dynamic pressure $\frac{\rho}{2}U_\infty^2$:

$$c_p = \frac{p - p_\infty}{\frac{\rho}{2}U_\infty^2}. \tag{2.6}$$

Dimensionless Wall Distance

The *dimensionless wall distance* y^+ is a measure of the distance to a wall in a boundary layer. It is defined with the geometric distance to the wall y_w, the friction velocity u_τ, the kinematic viscosity ν, the wall shear stress τ_w and the density ρ as:

$$y^+ = \frac{y_w u_\tau}{\nu} = \frac{y_w}{\nu}\sqrt{\frac{\tau_w}{\rho}}. \tag{2.7}$$

Courant-Friedrichs-Lewy Number

The *Courant-Friedrichs-Lewy number* (CFL) (Courant et al. [20]), also called *Courant number*, evaluates the ratio of the convective transport in the flow per time step Δt to the cell length Δx:

$$CFL = \Delta t \sum_{i=1}^{n} \frac{u_{x_i}}{\Delta x_i}. \tag{2.8}$$

Two different implementations of the CFL number are employed for the unstructured grids in use. The cell-CFL number CFL_c is computed for a cell with the normal vector of a cell face $\mathbf{s}_f$, the velocity through the face $\mathbf{u}_f$ and the cell volume V_c (see Fig. 2.2):

$$CFL_c = \frac{\Delta t}{2} \frac{\sum_f |\mathbf{s}_f \cdot \mathbf{u}_f|}{V_c}. \tag{2.9}$$

The face-CFL number CFL_f is evaluated for a face with the vector between the cell centers of the adjacent cells $\mathbf{d}$ (see Fig. 2.2):

$$CFL_f = \Delta t \frac{|\mathbf{s}_f \cdot \mathbf{u}_f|}{|\mathbf{s}_f|\,|\mathbf{d}|} \tag{2.10}$$

The face-CFL number is used for the CFL-based blending between discretization schemes. If not indicated otherwise, the CFL number is computed according to Eq. 2.9.

2.2 Numerical Methods

The numerical approach, followed in this thesis, is presented in this chapter. The details of the simulation setups of individual test cases are discussed in the respective sections in chapter 3. If not indicated otherwise, simulations have been executed with OpenFOAM®Version 2.2, Weller et al. [110].

The solution algorithm used in the numerical computations is the so called *PISO* algorithm (*Pressure-Implicit with Splitting of Operators*) of Issa [45]. The momentum equation is computed by a linear system solver with *Gauß-Seidel* smoothing. For the pressure equation, either a *Preconditioned Conjugate Gradient* solver (PCG) with *Diagonal-based Incomplete Cholesky* preconditioner (DIC) or a *Generalized Geometric-Algebraic Multigrid* solver (GAMG) is used.

2.2.1 Discretization

Using the *finite volume method*, the governing equations are discretized to be solved on unstructured grids. The discussion of the discretization approaches is based on Jasak [46], Greenshields [79] and Gestrich [31].

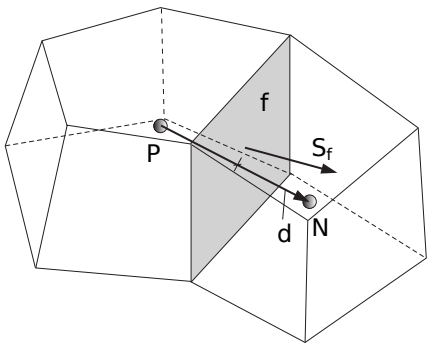

Figure 2.2: Parameters in finite volume discretization (Greenshields [79]).

The nomenclature of the discretization parameters are shown in Fig. 2.2. The figure shows a control volume with center point P and a neighboring control volume with center point N. The vector between the center points is $\mathbf{d}$. Indicated in gray, is the face f and its corresponding normal vector $\mathbf{s_f}$.

The description of the discretization procedure is based on the generic conservation equation 2.11 with the scalar quantity Φ.

$$\underbrace{\frac{\partial}{\partial t}\int_V \Phi dV}_{temporal\ variation} + \underbrace{\int_V \frac{\partial u_j \Phi}{\partial x_j} dV}_{convection} - \underbrace{\int_V \frac{\partial}{\partial x_j}\left(\Gamma \frac{\partial \Phi}{\partial x_j}\right) dV}_{diffusion} = \underbrace{\int_V S_\Phi dV}_{source} \tag{2.11}$$

Temporal discretization

The discretization of the time derivative in equation 2.11 is carried out employing a second order, implicit method (see, e.g. Ferziger and Peric [28]).

$$\frac{\partial}{\partial t}\int_V \Phi dV = \frac{3(\Phi V)^n - 4(\Phi V)^{n-1} + (\Phi V)^{n-2}}{2\Delta t} \tag{2.12}$$

The method is sometimes referred to as *Second Order Backward Euler* (e.g. Menter [72]).

Convection term

The convection term in equation 2.11 is discretized with the sum of the volume flow rate F through the faces of the control volume

$$\int_V \frac{\partial u_j \Phi}{\partial x_j} dV = \int_S d\mathbf{s} \cdot (\mathbf{u}\Phi) = \sum_f \mathbf{s}_f \cdot \mathbf{u}_f \Phi_f = \sum_f F\Phi_f. \tag{2.13}$$

The quantity Φ_f at the face centers has to be interpolated from the cell centers. With the linear interpolation

$$\Phi_f = f_x \Phi_P + (1 - f_x)\Phi_N. \tag{2.14}$$

Here, Φ_P is the value of the quantity at the cell center of the owner cell of the face, Φ_N is the value at the cell center of the neighbor cell and $f_x = \overline{fN}/\overline{PN}$ is the weighting factor of the interpolation. An alternative to the central interpolation is an upwind discretization approach. For an upwind discretization, the flow through the faces Φ_f is replaced by the value of the cell center upstream the face. With

$$\Phi_f = \begin{cases} \Phi_P \text{ if } F \geq 0 \\ \Phi_N \text{ if } F < 0. \end{cases} \tag{2.15}$$

In car aerodynamics simulations, a purely central discretization of convection terms is usually not possible or reasonable as the central discretization requires a considerably high grid density to avoid numerical oscillations. A pure upwind discretization is also not possible, as it introduces a high amount of numerical dissipation. The preferred discretization schemes are therefore hybrid schemes with as little upwind contribution as possible. The convection schemes used in the test cases are cited in the individual sections of chapter 3.

Diffusion term

The diffusion term of equation 2.11 in its discretized form with the diffusion coefficient Γ_f on the cell face is

$$\int_V \frac{\partial}{\partial x_j}\left(\Gamma\frac{\partial\Phi}{\partial x_j}\right)dV = \int_S d\mathbf{s}\cdot\left(\Gamma\frac{\partial\Phi}{\partial x_j}\right) = \sum_f \Gamma_f\mathbf{s}_f\cdot\left(\frac{\partial\Phi}{\partial x_j}\right)_f. \tag{2.16}$$

On orthogonal grids, the gradient in equation 2.16 can be computed by a linear interpolation with the neighboring cells

$$\mathbf{s}_f\cdot\left(\frac{\partial\Phi}{\partial x_j}\right)_f = |\mathbf{s}_f|\,\frac{\Phi_N-\Phi_P}{|\mathbf{d}|}. \tag{2.17}$$

For non-orthogonal grids, were the vector $\mathbf{d}$ between the cell centers is not perpendicular to the face between the cells, the interpolation has to be corrected.

$$\mathbf{s}_f\cdot\left(\frac{\partial\Phi}{\partial x_j}\right)_f = \mathbf{\Delta}\cdot\frac{\Phi_N-\Phi_P}{|\mathbf{d}|} + \mathbf{k}\cdot\left(\frac{\partial\Phi}{\partial x_j}\right)_f \tag{2.18}$$

The first term on the right hand side of Eq. 2.18 is the orthogonal contribution. The second term on the right hand side is the non-orthogonal correction. The vectors $\mathbf{\Delta}$ and $\mathbf{k}$ have to fulfill the relation $\mathbf{s}_f = \mathbf{\Delta} + \mathbf{k}$ and are computed by the *over-relaxed approach* described in Jasak [46].

The gradient $\left(\frac{\partial\Phi}{\partial x_j}\right)_f$ in the second term on the right hand side of Eq. 2.18 is computed by a Gauss integration

$$\int_V \frac{\partial\Phi}{\partial x_i}dV = \int_S d\mathbf{s}\Phi = \sum_f \mathbf{s}_f\Phi_f. \tag{2.19}$$

The values of the quantity Φ_f on the faces are computed by a second order linear interpolation.

Source term

To discretize nonlinear source terms, the source term $S_\Phi(\Phi)$ is linearized according to Jasak [46]

$$S_\Phi(\Phi) = Su + Sp\,\Phi, \tag{2.20}$$

where Su and Sp can depend on Φ. The volume integral is computed by a product of the cell volume and the value of the quantity at the cell center

$$\int_V S_\Phi(\Phi) dV = Su\, V_P + Sp\, V_P\, \Phi_P. \tag{2.21}$$

2.2.2 Turbulence Modeling

To model the unresolved turbulent fluctuations in the flow, a *Detached-Eddy Simulation* approach (DES) is followed. The DES is a hybrid method of an *Unsteady Reynolds-Averaged-Navier-Stokes* (URANS) and a *Large Eddy Simulation* method (LES). The DES is based on one set of equations for the entire fluid domain. If the equations act as URANS or LES simulation is controlled by the DES length scale:

$$L_{DES} = \min\left(L_{URANS}, C_{DES}\Delta\right). \tag{2.22}$$

The length scale is computed from the turbulent length scale of the URANS simulation L_{URANS} and the product of the cell size Δ and a constant C_{DES}. Close to a wall, the URANS length scale L_{URANS} is smaller than the product $C_{DES}\Delta$ and the equations act as a URANS simulation. At a distance to the wall, the URANS length scale L_{URANS} becomes larger and the model acts as a LES model reducing the turbulent viscosity and resolving larger turbulence structures. The discussion of the turbulence modeling approach in this chapter is based on Spalart and Allmaras [97], Spalart et al. [98, 100] and Gestrich [31].

Spalart-Allmaras Detached-Eddy Simulation Model

The Detached-Eddy simulation model used in this thesis is based on the *Spalart-Allmaras* model of Spalart and Allmaras [97]. The one equation model computes the modified viscosity $\tilde{\nu}$ with the transport equation

$$\frac{\partial \tilde{\nu}}{\partial t} + \frac{\partial u_j \tilde{\nu}}{\partial x_j} = C_{b1}\tilde{S}\tilde{\nu} + \frac{1}{C_\sigma}\left[\frac{\partial}{\partial x_j}\left((\nu + \tilde{\nu})\frac{\partial \tilde{\nu}}{\partial x_j}\right) + C_{b2}\left(\frac{\partial \tilde{\nu}}{\partial x_j}\right)^2\right] - C_{w1} f_w \left[\frac{\tilde{\nu}}{\tilde{d}}\right]^2. \tag{2.23}$$

The modified viscosity $\tilde{\nu}$ is connected to the turbulence viscosity ν_t by the function f_{v1} with $\chi = \tilde{\nu}/\nu$:

$$\nu_t = \tilde{\nu} f_{v1}, \qquad f_{v1} = \frac{\chi^3}{\chi^3 + C_{v1}^3}. \tag{2.24}$$

In the production term $C_{b1}\tilde{S}\tilde{\nu}$ on the right hand side of Eq. 2.23, $\tilde{S}$ is:

$$\tilde{S} = \Omega f_{v3} + \frac{\tilde{\nu}}{\kappa^2 \tilde{d}^2} f_{v2}, \tag{2.25}$$

with the invariant of the rotation tensor $\Omega = \sqrt{2\boldsymbol{\Omega}_{ij}\boldsymbol{\Omega}_{ij}}$. In the implemented version of the model, the functions f_{v2} and f_{v3} include modifications of Ashford [3] over the original formulation of the model to avoid a negative production term and enhance the numerical stability of the model:

$$f_{v2} = \left(1 + \frac{\chi}{C_{v2}}\right)^{-3}, \qquad f_{v3} = \frac{(1 + \chi f_{v1})(1 - f_{v2})}{\chi}. \tag{2.26}$$

The function f_w in the destruction term $C_{w1} f_w \left[\frac{\tilde{\nu}}{\tilde{d}}\right]^2$ of Eq. 2.23 is:

$$f_w = g\left[\frac{1 + C_{w3}^6}{g^6 + C_{w3}^6}\right]^{1/6}, \quad g = r + C_{w2}(r^6 - r), \quad r = \frac{\tilde{\nu}}{\tilde{S}\kappa^2 \tilde{d}^2}. \tag{2.27}$$

The coefficients of the turbulence model, as used in the simulations, are listed in table 2.1:

Table 2.1: Coefficients of the *Spalart-Allmaras* turbulence model

C_σ	C_{b1}	C_{b2}	C_{v1}	C_{v2}	C_{w1}	C_{w2}	C_{w3}	κ
2/3	0.1355	0.622	7.1	5.0	3.239	0.3	2.0	0.41

In the original DES variant of Spalart et al. [98] the turbulence length scale $\tilde{d}$ was taken as the minimum of the turbulent length scale of the URANS simulation d_w which is equal to the distance to the nearest wall, and the cell length Δ:

$$\tilde{d} = \min(d_w, C_{DES}\Delta). \tag{2.28}$$

The constant C_{DES} was calibrated by Shur et al. [95] to $C_{DES} = 0.65$. The cell length is the maximum length of the cell in the grid directions:

$$\Delta = \max(\Delta_x, \Delta_y, \Delta_z). \tag{2.29}$$

In this DES variant, the length scale $\tilde{d}$ is determined by the geometry and the grid only. A problem of this approach is that the grid in the velocity boundary layer can be fine enough to reduce the modeled turbulence viscosity considerably, but not fine enough to sufficiently

resolve the coherent turbulence structures. This effect leads to an underestimated sum of the modeled Reynolds stresses and the resolved stresses called *Modelled-Stress Depletion* (MSD) (see e.g. Spalart et al. [100], Spalart [99] or Sagaut et al. [91]).

In a study of the flow around an Ahmed body, Menter and Kuntz [73] documented an unphysical separation of the flow described as *Grid-Induced Separation* due to a high grid resolution in the boundary layer and the resulting MSD effect. To avoid the separation, Menter and Kuntz proposed to use a shielding function for the boundary layer region of the flow. In [100], Spalart et al. proposed a shielding function for the *Spalart-Allmaras* DES model. The computation of the turbulence length scale $\tilde{d}$ in the new DES variant modifies to:

$$\tilde{d} = d_w - f_d \max(0, d_w - C_{DES}\Delta). \tag{2.30}$$

The shielding function f_d is computed according to Eq. 2.31 with a limit to r_d of $r_d \leq 10$:

$$f_d = 1 - \tanh([8r_d]^3), \qquad r_d = \frac{\nu_t + \nu}{\sqrt{\frac{\partial u_i}{\partial x_j}\frac{\partial u_i}{\partial x_j}}\kappa^2 d_w^2}. \tag{2.31}$$

The modified variant of the *Spalart-Allmaras* DES model (SA DES) is called the *Spalart-Allmaras Delayed-Detached-Eddy Simulation* model (SA DDES). The so called *trip-terms* included in the *Spalart-Allmaras* model described in Spalart and Allmaras [97] are not implemented in solver used in the simulations. The trip-terms were intended for laminar-turbulent transition flows and are not necessary for the flows under investigation.

Wall Function

To model the turbulent near wall flow, a continuous wall model for the viscous sublayer, the buffer layer and the logarithmic part of the boundary layer is used. The velocity profile is described by the wall model of Spalding [101]:

$$y^+ = u^+ + \frac{1}{E}\left[e^{\kappa u^+} - 1 - \kappa u^+ - \frac{1}{2}(\kappa u^+)^2 - \frac{1}{6}(\kappa u^+)^3\right]. \tag{2.32}$$

With the constants $E = 9.8$ and $\kappa = 0.41$ and the dimensionless wall distance y^+ and the dimensionless velocity u^+:

$$y^+ = \frac{y_w u_\tau}{\nu}, \qquad u^+ = \frac{u_{||}}{u_\tau}. \tag{2.33}$$

The wall normal distance of the first grid point y_w and the relative velocity parallel to the wall in the first grid point $u_{||}$ are taken from the simulation. The friction velocity u_τ is computed iteratively by a Newton-Raphson method following the procedure

$$u_\tau^n = u_\tau^{n-1} - \frac{f}{f'}, \tag{2.34}$$

with the function f and its derivative f' according to de Villiers [25]:

$$f = u^+ - y^+ + \frac{1}{E}\left[e^{\kappa u^+} - 1 - \kappa u^+ - \frac{1}{2}(\kappa u^+)^2 - \frac{1}{6}(\kappa u^+)^3\right], \tag{2.35}$$

$$f' = \frac{\partial f}{\partial u_\tau} = -\frac{u^+}{u_\tau} - \frac{y^+}{u_\tau} + \frac{1}{E}\left[-\frac{\kappa u^+}{u_\tau}e^{\kappa u^+} + \frac{\kappa u^+}{u_\tau} + \frac{1}{u_\tau}(\kappa u^+)^2 + \frac{1}{2u_\tau}(\kappa u^+)^3\right]. \tag{2.36}$$

With the friction velocity u_τ, the wall shear stress τ_w and the turbulence viscosity ν_t at the wall can be computed:

$$u_\tau = \sqrt{\frac{\tau_w}{\rho}} = \sqrt{(\nu_t + \nu)\left|\frac{\partial u_i}{\partial y_w}\right|}. \tag{2.37}$$

The wall model is applicable for grids with the first off-the-wall grid point in either the viscous region, the buffer layer or the logarithmic layer. The model is strictly valid only in equilibrium boundary layers with zero pressure gradient.

2.2.3 Modeling of Porosity

The loss of momentum of the flow, passing through a porosity, is modeled with the *Darcy-Forchheimer Equation*. For a homogeneous porous media, the Darcy-Forchheimer equation reads:

$$\frac{\mathbf{s}}{\rho} = -(\nu\, d + \frac{|\mathbf{u}|}{2}\, f)\, \mathbf{u}. \tag{2.38}$$

The equation accounts for the viscous losses and for inertial losses in the flow. The coefficients d and f are usually determined experimentally by measurements of the pressure drop in the porosity region. The model is treated as a source term in the Navier-Stokes equations.

2.3 Experimental Methods

To validate the numerical methods and simulation setups used in this thesis, wind tunnel experiments have been conducted. In this chapter, the experimental setup including the wind tunnels, the aerodynamic test model and the main elements of the instrumentation are presented.

2.3.1 Wind tunnels

Flow measurements of the DrivAer body have been executed in two different wind tunnel facilities (results see chapter 3.3). The experiments took place in wind tunnel A at the Chair of Aerodynamics and Fluid mechanics at Technical University of Munich (TUM) and in the aeroacoustics wind tunnel of AUDI AG.

Wind Tunnel at TUM

The wind tunnel A at the Chair of Aerodynamics and Fluid mechanics at Technical University of Munich (TUM) is a low-speed, closed return model scale wind tunnel. It can be configured with a closed or open test section and can be equipped with a stationary floor or with a single belt rolling road system. For car aerodynamics investigations, the tunnel is used with an open test section and with rolling road system.

The nozzle cross-section of the tunnel is $4.32\,m^2$, it is equipped with Seifert wings to reduce the influence of shear layers. The length of the test section is $4.8\,m$. The belt of the rolling road system is 1.39 m wide. To remove the boundary layer from the nozzle exit, the tunnel has an adjustable, passive boundary layer scoop system. The turbulence intensity of the tunnel, given by Eq. 2.39, is $I_x = I_y = I_z < 0.4\%$.

$$I = \frac{1}{U_\infty} \cdot \sqrt{\frac{1}{3} \cdot \left(u'^2 + v'^2 + w'^2\right)} \tag{2.39}$$

With the free stream velocity U_∞ and the root-mean-square of the turbulent velocity fluctuations u', v' and w'.

The Model Support System (MSS) for car aerodynamics investigations consists of a top sting that holds the car model from above and of four arms that hold the wheels on the rolling road simulation belt. The top sting is mounted on a traversing system for all three spatial axes. In addition to the automatic traversing along the axes, it is also possible to adjust the pitch and yaw angle of the model by manually adjusting the top sting. The four wheel arms reach from the sides into the air stream and are mounted on a rail system. The wheel arms allow for a positioning in x and y direction. For an adjustment

of the camber angle and the toe angle, the angles of the arms are adjustable. The contact pressure of the wheels on the belt is also adjustable at the wheel arms. The blockage ratio, according to Eq. 2.40, of the DrivAer model and the MSS in the wind tunnel is approx. 12% (Mack et al. [67]).

$$BR = \frac{A_{ref}}{A_{nozzle}} \tag{2.40}$$

With the frontal area of the model including the model support system A_{ref} and the exit area of the nozzle A_{nozzle}. A detailed description of the wind tunnel as well as the axial distribution of the static pressure coefficient along the center line of the test section compared to different wind tunnels can be found in Mack et al. [67].

Wind tunnel at Audi

The aeroacoustics wind tunnel at Audi is a closed return full scale wind tunnel used for aerodynamic as well as for aeroacoustic investigation and optimization of cars. It is equipped with a five belt rolling road system. The nozzle cross-section of the tunnel is $11\,m^2$, the length of the test section is adjustable from $9\,m$ to $10\,m$. For the experimental investigations with the 40% DrivAer model, only the middle belt of the rolling road system has been used. The middle belt is $1\,m$ wide and $5.5\,m$ long. The aeroacoustics wind tunnel has a boundary layer suction system with multiple, separately adjustable chambers to remove the boundary layer caused by the nozzle. The turbulence intensity given by Eq. 2.39 is $I_x = I_y = I_z < 0.3\%$ (Wickern and Lindener [111]). For investigations with the DrivAer model, the same model support system has been used as in wind tunnel A at TUM. The blockage ratio, according to Eq. 2.40, of the DrivAer model and the model support system in the wind tunnel is approx. 5%. A detailed description of the aeroacoustics wind tunnel at Audi as well as the axial pressure distribution of the Audi aeroacoustics wind tunnel compared with the pressure distributions in ten other European wind tunnels can be found in Wickern and Lindener [111].

2.3.2 Aerodynamic Test Model

The aerodynamic test model is a 40% model of the DrivAer geometry (www.drivaer.com, [38, 68]). The model is built with a carbon fiber outer shell and an aluminum frame. The side mirrors are removable and the rear end shapes as well as underbody shapes are changeable. The wheels are not physically connected to the car body and are held by wheel arms as described above. The wheels are driven by the motion of the ground simulation belt.

Instrumentation

The main force balance is an internal, six-component force balance mounted inside the vehicle. It connects the model to the top sting and measures lift and drag forces as well as roll, yaw and pitch moments. Drag forces of the wheels are measured by separate balances in the wheel arms. The rotational speed of the wheels is measured by an inductive sensor. By measuring the speed of the wheels and the speed of the ground simulation belt, slip between the wheels and the belt can be monitored and the contact pressure of the wheels on the belt can be adjusted. The lift forces of the wheels are not measured.

The model can be equipped with up to 400 static pressure taps. The pressure taps have a bore diameter of $0.3\,mm$, connected by tubes to pressure scanners and a digital service module. The signals from the sensors are transmitted to the data acquisition computers in the control room of the wind tunnel by cables, routed through the top sting. The processing of sensor data is done by in-house software written in the visual programming language LabVIEW$^{\text{TM}}$ by National Instruments (Mack et al. [68]).

2.4 Vortex Identification

Arguably, the most important class of coherent structures in car aerodynamics are vortices. Largely stationary vortices like the A-pillar or C-pillar vortices or the recirculation vortices in the near wake can redirect the main flow around a car and alter the pressure distribution on the car surface. Unsteady vortices store and transport energy and dissipate it in the wake flow, contributing to the drag of the vehicle. As the turbulent flow around a car geometry is full of interpenetrating vortices, it can be challenging to isolate individual vortices from the flow field. Besides the use of basic flow variables as velocity, pressure or vorticity, more suitable vortex detection methods are in use.

2.4.1 Requirements for Automotive Aerodynamics Flow Fields

Automotive aerodynamics flow fields typically consist of a large number of vortices with a wide range of length and time scales. Due to the development of the boundary layers and their separation as shear layers, the flow contains a high amount of shear. While the flow is redirected around the car geometry, a high amount of elongational motion (irrotational straining) is also present in the flow. These effects together with the demands of the aerodynamics development process form the special requirements to vortex detection methods for automotive aerodynamics. The requirements for vortex detection methods for automotive aerodynamics flow fields are:

- The detection method should implement a clear and consistent physical concept of a vortex.
- The method should be able to describe the geometry of vortices and identify vortex core lines.
- It should be able to quantify the local intensity of the swirling motion in the vortices.
- The result of the detection method should provide the possibility to be used for further computations.
- The method should be applicable to three dimensional flow fields.
- The method should be valid for compressible flows and flows with variable density.
- The result of the method should be independent of reference frame (objective).

Although there is no consensus about the definition of a vortex, it is obvious that a detection method should have a clear physical meaning. For canonical flows, were there

is a consensus whether they contain vortices, the method should neither fail to show vortices nor show false positives. As the bluff body flow around a car contains cascades of interpenetrating vortices, an important requirement for car aerodynamics flow fields is the ability of the method to quantify the local intensity and orientation of the swirling motion and, as a result, provide the ability to describe the geometries of the vortices. While the majority of vortex detection methods has been developed to indicate the presence of a vortex, the focus in car aerodynamics is more on the quantification of the effect of vortices. Therefore, the result of the method should be a three dimensional field that can be used for further computations of local or integrated properties of the vortices. As car aerodynamics flow fields are usually incompressible, the applicability to compressible flows is not always required. In the case of heat transfer problems, were buoyancy effects have to be considered, the method has to be applicable for variable density and compressible flows. For a method to be applicable in the whole aerodynamics development process, including heat transfer problems, a method should be preferred that is valid for compressible flows and flows of variable density. A general claim to vortex detection methods is frame invariance (or objectivity). As most of the methods relying on the velocity gradient tensor are Galilean invariant, an invariance to transformations in rotating coordinate systems is usually harder to achieve. While frame invariance can be of importance in the simulation of cornering motions, or in the rotating frame used to model wheel rotation, a Galilean invariant method is acceptable for most problems found in car aerodynamics. From a fundamental point of view, an unsteady vortex is a Lagrangian coherent structure and should, therefore, be described by a Lagrangian description.

2.4.2 Vortex Detection Methods

The most common vortex detection methods, Q-criterion, Δ-criterion, λ_2-criterion and λ_{ci}-criterion are presented in this section. In addition, a less well known decomposition of the velocity gradient tensor is presented and discussed in more detail.

Q-Criterion

The Q-criterion (Hunt et al. [42]), also called the Okubo-Weiss-criterion as it was independently developed by Okubo [78] and Weiss [109] for two dimensional flows, is the second invariant of the velocity gradient tensor for incompressible flows. The second invariant of the velocity gradient tensor

$$II_{\nabla \mathbf{u}} = \frac{1}{2}\left((\mathrm{tr}(\nabla \mathbf{u}))^2 - \mathrm{tr}((\nabla \mathbf{u})(\nabla \mathbf{u}))\right) \tag{2.41}$$

simplifies with the incompressibility requirement $\mathrm{tr}(\nabla \mathbf{u}) = 0$ to the Q-criterion

$$Q = II_{\nabla \mathbf{u}} = \frac{1}{2}\left(\mathrm{tr}((\nabla \mathbf{u})(\nabla \mathbf{u}))\right). \tag{2.42}$$

With the antisymmetric part of the velocity gradient tensor $\Omega = \frac{1}{2}\left(\nabla \mathbf{u} - (\nabla \mathbf{u})^T\right)$, the symmetric part of the velocity gradient tensor $S = \frac{1}{2}\left(\nabla \mathbf{u} + (\nabla \mathbf{u})^T\right)$ and the tensor norm $\|\Omega\| = (\mathrm{tr}(\Omega\Omega^T))^{\frac{1}{2}}$ the Q-criterion can be written as

$$Q = \frac{1}{2}(\|\Omega\|^2 - \|S\|^2). \tag{2.43}$$

In equation 2.43, the physical meaning of the Q-criterion becomes apparent. The criterion evaluates the balance between the vorticity and the irrotational straining in the flow. The vorticity is represented by the magnitude of the vorticity tensor $\|\Omega\|$, the irrotational straining is represented by the magnitude of the strain tensor $\|S\|$.

In [42], Hunt et al. define two criteria to be fulfilled in a vortex. The first criterion demands the irrotational straining to be small compared to the vorticity and the second criterion requires a pressure minimum. Typically, the second criterion is not considered and a vortex is defined by the Q-criterion as a region were the value of Q is larger than a positive threshold value Q_V.

$$Q > Q_V \tag{2.44}$$

Due to the incompressibility requirement $\mathrm{tr}(\nabla \mathbf{u}) = 0$, the Q-criterion is not applicable to compressible flows.

Δ-Criterion

Chong et al. [18] define a vortex as a region in the flow, were the velocity gradient tensor $\nabla \mathbf{u}$ has complex eigenvalues. Eigenvalues λ_i of the velocity gradient tensor are complex in regions, were the discriminant D of the characteristic polynomial of the velocity gradient tensor is negative. The characteristic polynomial of $\nabla \mathbf{u}$ is

$$\lambda^3 + P\lambda^2 + Q\lambda + R = 0. \tag{2.45}$$

The discriminant D of the characteristic polynomial is

$$D = P^2Q^2 - 4Q^3 - 4P^3R - 27R^2 + 18PQR \tag{2.46}$$

The coefficient $P = -\nabla \cdot \mathbf{u}$ is zero for incompressible flow. With $P = 0$, the discriminant of the characteristic polynomial D simplifies to

$$D = -4Q^3 - 27R^2. \tag{2.47}$$

Deviating from the mathematical definition of the discriminant of the characteristic polynomial, the Δ-criterion is typically defined with Q according to equation 2.42 or 2.43 and $R = -Det(\nabla \mathbf{u})$ as

$$\Delta = -\frac{D}{108} = \left(\frac{1}{3}Q\right)^3 + \left(\frac{1}{2}Det(\nabla \mathbf{u})\right)^2. \tag{2.48}$$

According to equation 2.48, a vortex is defined by the Δ-criterion as a region were the value of Δ is larger than zero.

$$\Delta > 0 \tag{2.49}$$

As the Q-criterion, the Δ-criterion is not applicable to compressible flows due to the incompressibility requirement $P = \nabla \cdot \mathbf{u} = 0$ in equation 2.47.

λ_2-Criterion

The λ_2-Criterion (Jeong and Hussain [47]) is based on the assumption that a vortex core coincides with a pressure minimum in the absence of irrotational straining and viscous effects. By taking the gradient of the incompressible Navier–Stokes equation and discarding the terms of irrotational straining, viscous effects and vorticity transport, the pressure Hessian can be formulated as:

$$\nabla (\nabla p) = -\rho(S^2 + \Omega^2). \tag{2.50}$$

A local minimum of the so modified pressure in a plane requires two negative eigenvalues of the symmetric tensor $S^2 + \Omega^2$. Ordering the eigenvalues as $\lambda_1 \geq \lambda_2 \geq \lambda_3$, this corresponds to a negative second eigenvalue λ_2:

$$\lambda_2(S^2 + \Omega^2) < 0 \tag{2.51}$$

The λ_2-Criterion is derived for incompressible flows and is not applicable to compressible flows.

λ_{ci}-Criterion

Zhou et al. [112] start from the vortex definition of Chong et al. [18] who define a vortex as a region in the flow with complex eigenvalues of the velocity gradient tensor. Zhou et al. show that the imaginary part of the complex conjugate pair of eigenvalues of the velocity gradient tensor equates to the local swirling strength of the flow. The λ_{ci}-criterion defines a vortex as a region in the flow with non-zero imaginary part of the complex eigenvalue pair of the velocity gradient tensor. Consistent with the definition of Zhou et al. [112] the swirling strength is defined by the square of the imaginary part:

$$\lambda_{ci}^2 > 0 \tag{2.52}$$

The λ_{ci}-criterion is applicable to incompressible and compressible flows.

Shear Maximizing Decomposition of the velocity gradient tensor

The velocity gradient tensor $\nabla\mathbf{u}$ can be decomposed into a shear rate tensor $(\nabla\mathbf{u})_{SH}$, a rate of elongation tensor $(\nabla\mathbf{u})_{EL}$ and a rate of rotation tensor $(\nabla\mathbf{u})_{RR}$.

$$\nabla\mathbf{u} = (\nabla\mathbf{u})_{SH} + (\nabla\mathbf{u})_{EL} + (\nabla\mathbf{u})_{RR} \tag{2.53}$$

The shear rate tensor $(\nabla\mathbf{u})_{SH}$ describes a *simple shearing motion*. The rate of elongation tensor describes an *irrotational straining motion* and the rate of rotation tensor describes the rotation of fluid particles around a common center in the form of a *rigid body rotation*. The shear rate tensor $(\nabla\mathbf{u})_{SH}$ itself is a superposition of irrotational straining $\mathbf{S}_{SH}$ and the rotation of fluid particles around themselves $\mathbf{\Omega}_{SH}$. With the Cauchy-Stokes decomposition, the shear rate tensor can be decomposed as $(\nabla\mathbf{u})_{SH} = \mathbf{S}_{SH} + \mathbf{\Omega}_{SH}$.

For two dimensional relative motions near a point, the decomposition is straight forward and described e.g. in the textbook of Batchelor [6] (Chapter 2.3: *Analysis of the relative motion near a point*). For three dimensional relative motions, the decomposition is more complex and an analytical solution is not yet available. This is due to the fact that the relative orientation of elongation, shear and rotation is arbitrary in three dimensional relative motions. In addition, there are three principal axes of elongation in three dimensional flows compared to two in two dimensional flows. Three shear planes are possible in three dimensions compared to one possible shear plane in two dimensions.

In [53], Kolář reintroduces the method as *Triple Decomposition of Motion* (TDM) for vortex identification in two dimensional flows. He uses the magnitude of the rotation tensor $||(\nabla\mathbf{u})_{RR}||$ as a vortex criterion which he calls the *residual vorticity*.

In [54] and [55], Kolář introduces a procedure to compute the decomposition for three dimensional flows numerically: When the shear planes of the $(\nabla \mathbf{u})_{SH}$ tensor are aligned with the coordinate axes, the shear rate tensor can be computed by

$$(\nabla \mathbf{u})_{SH} = \begin{pmatrix} 0 & \frac{\partial u}{\partial y} - sign(\frac{\partial u}{\partial y}) min(\frac{\partial u}{\partial y}, \frac{\partial v}{\partial x}) & \bullet \\ \frac{\partial v}{\partial x} - sign(\frac{\partial v}{\partial x}) min(\frac{\partial v}{\partial x}, \frac{\partial u}{\partial y}) & 0 & \bullet \\ \bullet & \bullet & 0 \end{pmatrix}. \tag{2.54}$$

Equation 2.54 stems from a geometrical interpretation of three dimensional shearing motions. The non-specified off-diagonal elements (dot symbols) are constructed strictly analogous to the specified elements. A residual tensor $(\nabla \mathbf{u})_{RES}$ is computed from the velocity gradient tensor and the shear rate tensor.

$$\begin{aligned} (\nabla \mathbf{u})_{RES} &= \nabla \mathbf{u} - (\nabla \mathbf{u})_{SH} \\ &= \begin{pmatrix} \frac{\partial u}{\partial x} & sign(\frac{\partial u}{\partial y}) min(\frac{\partial u}{\partial y}, \frac{\partial v}{\partial x}) & \bullet \\ sign(\frac{\partial v}{\partial x}) min(\frac{\partial v}{\partial x}, \frac{\partial u}{\partial y}) & \frac{\partial v}{\partial y} & \bullet \\ \bullet & \bullet & \frac{\partial w}{\partial z} \end{pmatrix}. \end{aligned} \tag{2.55}$$

The rate of elongation tensor $(\nabla \mathbf{u})_{EL}$ and the rigid body rotation tensor $(\nabla \mathbf{u})_{RR}$ are computed by a Cauchy-Stokes decomposition of the residual tensor

$$(\nabla \mathbf{u})_{RES} = (\nabla \mathbf{u})_{EL} + (\nabla \mathbf{u})_{RR}, \tag{2.56}$$

with $(\nabla \mathbf{u})_{EL}$ being the symmetric and $(\nabla \mathbf{u})_{RR}$ being the antisymmetric part of the decomposition.

The Equations 2.54 to 2.56 are only applicable in a reference frame, were the shear planes of the shear rate tensor are aligned with the coordinate axes. Kolář calls this frame the *basic reference frame* (BRF). To find this frame, an objective function f is defined

$$
\begin{aligned}
f &= f(\alpha, \beta, \gamma) \\
&= ||(\nabla \mathbf{u})||^2 - ||(\nabla \mathbf{u})_{RES}||^2 \\
&= \frac{1}{2}\left|\left(\frac{\partial u}{\partial y}\right)^2 - \left(\frac{\partial v}{\partial x}\right)^2\right| + \frac{1}{2}\left|\left(\frac{\partial v}{\partial z}\right)^2 - \left(\frac{\partial w}{\partial y}\right)^2\right| + \frac{1}{2}\left|\left(\frac{\partial w}{\partial x}\right)^2 - \left(\frac{\partial u}{\partial z}\right)^2\right|
\end{aligned} \tag{2.57}
$$

The objective function $f(\alpha, \beta, \gamma)$ has its maximum in the so called basic reference frame. To maximize the objective function, each tensor in the tensor field is rotated individually around its Euler angles α, β and γ. In this thesis, a simplex algorithm is used to solve the optimization problem. For a flow field with 66 million cells and an abort criterion of the optimization algorithm of $\alpha = \beta = \gamma = 0.001°$, the decomposition takes approximately 130 *cpu h*. As the optimization problem has to be solved individually for every tensor of the tensor field, the method is well suited for parallel implementation. The code used in this study is not optimized for runtime performance.

In the publications of Kolář, the decomposition is called the *Triple Decomposition of Motion* (TDM). This name is somewhat unspecific and is also used for other decompositions of the velocity gradient tensor (e.g Chen et al. [14]). As the name has been in use before the publications of Kolář, the method will be described as *Shear Maximizing Decomposition* (SMD) in this thesis. Using the magnitude of the tensor of rigid body rotation as a vortex criterion, a vortex is defined by the SMD as

$$
||(\nabla \mathbf{u})_{RR}|| > 0. \tag{2.58}
$$

The SMD is applicable to incompressible and compressible flows. A comment on compressibility effects and vortex identification can be found in Kolář [58]. The connection between integral vortex strength and the Shear Maximizing Decomposition is discussed in Kolář [56].

An additional advantage of the SMD is the possibility to use the tensors of the decomposition for further computations. As an example, the dissipation of momentum from the shear rate tensor $(\nabla \mathbf{u})_{SH}$ and from the rigid body rotation tensor $(\nabla \mathbf{u})_{RR}$ is shown in Fig. 2.3. The dissipation from simple shear accounts for 91.7 % of the total dissipation of momentum in the flow. The spacial change of rigid body rotation accounts for 8.3% of the dissipation.

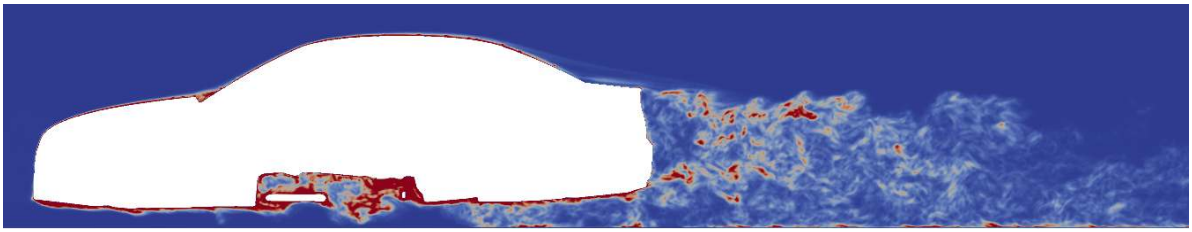

(a) Dissipation of momentum from $(\nabla \mathbf{u})_{SH}$

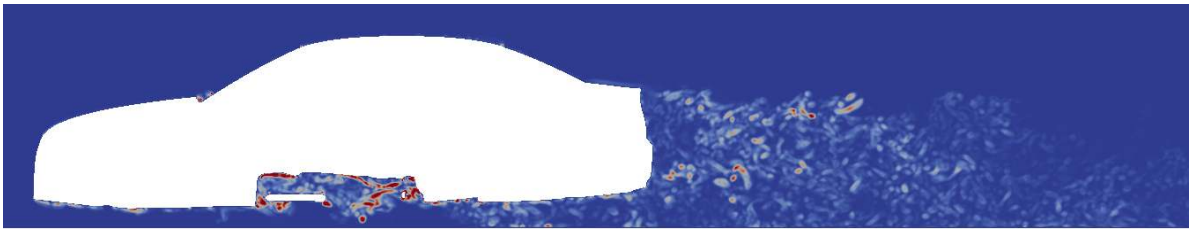

(b) Dissipation of momentum from $(\nabla \mathbf{u})_{RR}$

Figure 2.3: Dissipation of momentum from the shear rate tensor $(\nabla \mathbf{u})_{SH}$ and the rate of rigid body rotation tensor $(\nabla \mathbf{u})_{RR}$ normalized by density. The colors correspond to the same range of values in both pictures. Blue: 0 m/s^2, red: 50 m/s^2.

2.4.3 Evaluation of Detection Methods

As already apparent from the mathematical definitions shown in chapter 2.4.2, vortices are described differently by the individual vortex criteria. In this chapter, the criteria are compared and evaluated for their applicability in car aerodynamics. Figure 2.4 shows isosurfaces of the criteria for the time averaged flow around the DrivAer body. The isovalues are chosen visually with respect to the size of the longitudinal vortices from the side mirrors.

Compared to the Q-criterion, the vortices extracted by the Δ-criterion have larger diameter in general. More vortices are visible on the trunk deck and in the near wake. The vortices from the side mirrors are underpredicted by the Δ-criterion. As the isovalues are chosen with respect to the size of the longitudinal vortices from the side mirrors, other vortices are overemphasized when compared to the Q-criterion. The isosurface of the λ_2-criterion is similar to the isosurface of the Q-criterion. Differences are visible at the rear edge of the trunk deck in the $y = 0$ plane of the model. The isosurface of the λ_{ci}-criterion is also similar compared to the Q-criterion. Only minor quantitative differences are visible. The $||(\nabla U)_{RR}||$-criterion emphasizes the dominant vortices more clearly. As the isovalue is chosen by the size of the a dominant vortex, less dominant vortices are underpredicted. Due to the emphasis on strong vortices, the topology of the vortices is more clearly resolved, as can be seen in the case of the vortex system at the bottom of the windshield. Here, the $||(\nabla U)_{RR}||$-criterion shows a split of the vortex tube in two vortices. The contribution of the near surface flow to the isosurfaces is due to the curvature of the

(a) Q-Criterion: $Q = 200s^{-2}$
($Q_{min} = -3.4 \cdot 10^9 s^{-2}$, $Q_{max} = 5.1 \cdot 10^8 s^{-2}$)

(b) Δ-Criterion: $\Delta = 7 \cdot 10^5 s^{-6}$
($\Delta_{min} = -1.5 \cdot 10^{27} s^{-6}$, $\Delta_{max} = 1.7 \cdot 10^{26} s^{-6}$)

(c) λ_2-Criterion: $\lambda_2 = -200s^{-2}$
($\lambda_{2,min} = -9.0 \cdot 10^8 s^{-2}$, $\lambda_{2,max} = 1.0 \cdot 10^9 s^{-2}$)

(d) λ_{ci}-Criterion: $\lambda_{ci} = 14s^{-1}$
($\lambda_{ci,min} = 0s^{-1}$, $\lambda_{ci,max} = 1.3 \cdot 10^4 s^{-1}$)

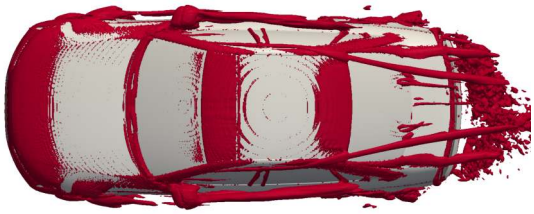

(e) $||(\nabla U)_{RR}||$-Criterion: $||(\nabla U)_{RR}|| = 10s^{-1}$
($||(\nabla U)_{RR}||_{min} = 0s^{-1}$, $||(\nabla U)_{RR}||_{max} = 7.5 \cdot 10^3 s^{-1}$)

Figure 2.4: Comparison of vortex criteria. Isovalues chosen visually with respect to the size of the longitudinal vortices from the side mirrors.

geometry. In the case of the $||(\nabla U)_{RR}||$-criterion, this effect is also reduced due to the emphasis of the criterion on more dominant vortices.

Canonical Flow Examples

For a better understanding of the behavior of the different vortex criteria, the criteria are applied to simple canonical flow examples. In addition to the conceptual challenges of vortex definition, sketched in the introduction (chapter 1.2), the individual vortex detection methods can be shown to fail for some canonical flows or show false positives for others.

Simple Shear Flow

The general case of the simple shear flow in three dimensions is a flow with constant variation of the velocity components along the coordinate axis in a Cartesian coordinate system. With the constants C_i and C_{ii}, the two possible flow fields for three shear planes are:

$$\mathbf{u}_1(x,y,z) = \{u(y),\ v(z),\ w(x)\} = \{y\,C_{uy} + C_u,\ z\,C_{vz} + C_v,\ x\,C_{wx} + C_w\} \tag{2.59}$$

and

$$\mathbf{u}_2(x,y,z) = \{u(y),\ v(z),\ w(x)\} = \{z\,C_{uz} + C_u,\ x\,C_{vx} + C_v,\ y\,C_{wy} + C_w\} \tag{2.60}$$

The velocity gradient of this type of flow is constant and of the form:

$$\nabla\mathbf{u}_1(x,y,z) = \begin{pmatrix} \frac{\partial u}{\partial x} & \frac{\partial u}{\partial y} & \frac{\partial u}{\partial z} \\ \frac{\partial v}{\partial x} & \frac{\partial v}{\partial y} & \frac{\partial v}{\partial z} \\ \frac{\partial w}{\partial x} & \frac{\partial w}{\partial y} & \frac{\partial w}{\partial z} \end{pmatrix} = \begin{pmatrix} 0 & C_{uy} & 0 \\ 0 & 0 & C_{vz} \\ C_{wx} & 0 & 0 \end{pmatrix} \tag{2.61}$$

and

$$\nabla\mathbf{u}_2 = \begin{pmatrix} 0 & 0 & C_{uz} \\ C_{vx} & 0 & 0 \\ 0 & C_{wy} & 0 \end{pmatrix} \tag{2.62}$$

The flow field of the three dimensional simple shear flow according to equations 2.59 and 2.60 has parallel stream lines and therefore does not contain any vortices. Applying the vortex criteria of chapter 2.4.2 to this flow with non-zero constants ($C_{ii} \neq 0$) results in:

$$\begin{array}{lcll} Q & = & 0 & (no\ vortex) \\ \Delta & > & 0 & (vortex) \\ \lambda_2 & < & 0 & (vortex) \\ \lambda_{ci} & > & 0 & (vortex) \\ ||(\nabla U)_{RR}|| & = & 0 & (no\ vortex) \end{array} \tag{2.63}$$

In a simple shear flow, the magnitudes of vorticity and irrotational straining are equal. As the Q-criterion evaluates the balance of vorticity and irrotational straining, the Q-criterion is always zero for the simple shear flow. For a vortex to be present, the Q-criterion requires a value larger than a positive threshold value Q_v. With a value of $Q = 0$ the Q-criterion

correctly indicates the absence of vortices in the flow. The vortex criteria Δ, λ_2 and λ_{ci} misinterpret the flow as a vortex. As the rotation in the simple shear flow is a rotation of fluid particles around themselves, the rigid body rotation in the flow $||(\nabla U)_{RR}||$ is zero. If $||(\nabla U)_{RR}||$ is used as a vortex criterion, it is correct in this case.

Potential Vortex

The flow field of a potential vortex in a cylindrical coordinate system with the tangential velocity u_θ, the radius r and a constant C is:

$$\mathbf{u}(r) = \{u_\theta(r),\ 0,\ 0\} = \{\frac{C}{r},\ 0,\ 0\} \tag{2.64}$$

The gradient of the velocity field of the potential vortex is symmetric and of the form:

$$\nabla\mathbf{u}(r,\theta,z) = \begin{pmatrix} \frac{\partial u_r}{\partial r} & \frac{1}{r}\frac{\partial u_r}{\partial \theta} - \frac{u_\theta}{r} & \frac{\partial u_r}{\partial z} \\ \frac{\partial u_\theta}{\partial r} & \frac{1}{r}\frac{\partial u_\theta}{\partial \theta} + \frac{u_r}{r} & \frac{\partial u_\theta}{\partial z} \\ \frac{\partial u_z}{\partial r} & \frac{1}{r}\frac{\partial u_z}{\partial \theta} & \frac{\partial u_z}{\partial z} \end{pmatrix} = \begin{pmatrix} 0 & -\frac{C}{r^2} & 0 \\ -\frac{C}{r^2} & 0 & 0 \\ 0 & 0 & 0 \end{pmatrix} \tag{2.65}$$

Applying the vortex criteria of chapter 2.4.2 to the flow field of the potential vortex for $r \neq 0$ and $C \neq 0$ results in:

$$\begin{array}{lcll} Q & < & 0 & (no\ vortex) \\ \Delta & < & 0 & (no\ vortex) \\ \lambda_2 & > & 0 & (no\ vortex) \\ \lambda_{ci} & = & 0 & (no\ vortex) \\ ||(\nabla U)_{RR}|| & = & 0 & (no\ vortex) \end{array} \tag{2.66}$$

In the case of a purely elongational motion of the potential flow, all vortex criteria fail to interpret the flow as a vortex.

Shear Vortex

The shear vortex is a vortex with a uniform velocity profile across the radius r and a gradient consisting of simple shear only. The flow field of the shear vortex in a cylindrical coordinate system with the tangential velocity u_θ and a constant C is:

$$\mathbf{u}(r) = \{u_\theta(r),\ 0,\ 0\} = \{C,\ 0,\ 0\} \tag{2.67}$$

The gradient of the velocity field of the shear vortex is of the form:

$$\nabla \mathbf{u}(r,\theta,z) = \begin{pmatrix} \frac{\partial u_r}{\partial r} & \frac{1}{r}\frac{\partial u_r}{\partial \theta} - \frac{u_\theta}{r} & \frac{\partial u_r}{\partial z} \\ \frac{\partial u_\theta}{\partial r} & \frac{1}{r}\frac{\partial u_\theta}{\partial \theta} + \frac{u_r}{r} & \frac{\partial u_\theta}{\partial z} \\ \frac{\partial u_z}{\partial r} & \frac{1}{r}\frac{\partial u_z}{\partial \theta} & \frac{\partial u_z}{\partial z} \end{pmatrix} = \begin{pmatrix} 0 & -\frac{C}{r} & 0 \\ 0 & 0 & 0 \\ 0 & 0 & 0 \end{pmatrix} \tag{2.68}$$

Applying the vortex criteria of chapter 2.4.2 to the flow field of the shear vortex for $r \neq 0$ and $C \neq 0$ results in:

$$\begin{array}{lcll} Q & = & 0 & (no\ vortex) \\ \Delta & = & 0 & (no\ vortex) \\ \lambda_2 & = & 0 & (no\ vortex) \\ \lambda_{ci} & = & 0 & (no\ vortex) \\ ||(\nabla U)_{RR}|| & = & 0 & (no\ vortex) \end{array} \tag{2.69}$$

As in the case of the potential vortex, all vortex criteria fail to interpret the flow field of the shear vortex as a vortex.

Bias of vortex criteria

The above examples of canonical flows are unlikely to exist in a turbulent bluff body flow in larger regions and for relevant time spans. Interpreting a relative motion, described by the velocity gradient tensor, as a superposition of basic relative motions like the rate of rotation, the shear rate or the rate of elongation, it becomes clearer how the vortex criteria are biased by these basic relative motions. By taking the *Lamb–Oseen* vortex as a model of a real vortex tube, the influence of the basic relative motions can be shown. The flow field of the *Lamb–Oseen* vortex is:

$$\mathbf{u}(r,t) = \{u_\theta(r,t),\ 0,\ 0\} = \left\{ \frac{\Gamma}{2\pi r}\left(1 - \exp\left(-\frac{r^2}{r_c^2(t)}\right)\right),\ 0,\ 0 \right\}. \tag{2.70}$$

With the tangential velocity u_θ, the radius r, the circulation Γ, the core radius of the vortex r_c and the time t. The radial velocity profile of the *Lamb–Oseen* vortex for one point in time is shown in figures 2.5 and 2.6 (thick solid line). The radius of the maximum value of the tangential velocity u_θ is indicated by a vertical dashed line.

In Fig. 2.5, the magnitude of the tensor of rigid body rotation $||(\nabla U)_{RR}||$ (dashed line), the magnitude of the shear rate tensor $||(\nabla U)_{SH}||$ (dotted line) and the magnitude of the rate of elongation tensor $||(\nabla U)_{EL}||$ (dash-dotted line) computed from the two dimensional Shear Maximizing Decomposition are shown. The values are normalized by the maximum of the magnitude of the rigid body rotation tensor. In the inner region of the vortex, the rigid body rotation clearly dominates the other relative motions but rapidly falls to zero at the maximum value of tangential velocity. Here, the shear has its maximum value, the

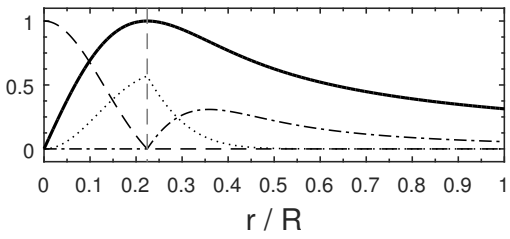

Figure 2.5: Radial profile of the *Lamb–Oseen* vortex. Tangential velocity u_θ: thick solid line, $||(\nabla U)_{RR}||$: dashed line, $||(\nabla U)_{SH}||$: dotted line, $||(\nabla U)_{EL}||$: dash-dotted line.

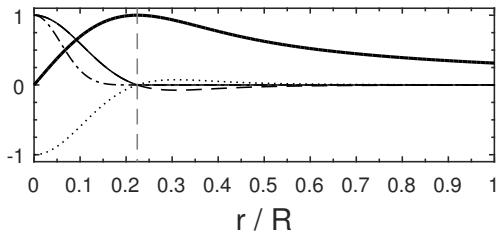

Figure 2.6: Radial profile of the *Lamb–Oseen* vortex. Tangential velocity u_θ: thick solid line, λ_{ci}-criterion: thin solid line, Q-criterion: dashed line, λ_2-criterion: dotted line, Δ-criterion: dash-dotted line.

elongational motion is zero. In the outer region of the vortex, no rigid body motion is present. After an increase of elongational motion, the shearing and elongational motion fall with increasing radius.

In Fig. 2.6, the normalized values of vortex criteria for the *Lamb–Oseen* vortex are shown. All vortex criteria indicate a vortex in the inner region of the *Lamb–Oseen* vortex and fall to zero at the maximum value of the tangential velocity. The Δ-criterion (dash-dotted line) drops the fastest with increasing radius. Q-criterion (dashed line) and λ_{ci}-criterion (thin solid line) are identical in the inner region of the *Lamb–Oseen* vortex. The λ_2-criterion (dotted line) is identical to the Q-criterion with inverted sign.

While the two dimensional *Lamb–Oseen* vortex is still a relatively simple example, the connection between the basic relative motions and the vortex criteria is more complex for three dimensional flows. In the case of a general three dimensional relative motion near a point, three individual shear planes are possible and the relative orientation between rigid body rotation, shear rate and rate of elongation is arbitrary. In Fig. 2.7, isosurfaces of magnitudes of the Shear Maximizing Decomposition tensors are shown. In all three visualizations, vortical structures are visible. The core regions of vortex tubes are captured mainly by the rigid body rotation $||(\nabla U)_{RR}||$ (Fig. 2.7a). The rate of elongation $||(\nabla U)_{EL}||$ (Fig. 2.7b) is dominated by the inviscid deflection of the flow around the geometry. In the shear rate $||(\nabla U)_{SH}||$ (Fig. 2.7c), large vortex tubes from the side mirrors and the A-pillars can be seen. The vortices in the flow around the DrivAer body consist to a varying degree of rigid body rotation, shearing and irrotational elongational motion.

To show how the vortex criteria depend on the basic relative motions of the Shear Maximizing Decomposition (SMD), the tensor fields of the SMD are computed and the vortex criteria are applied to these tensor fields. As a reference, isosurfaces of the vortex criteria applied to the full velocity gradient tensor are also shown. The Isovalues of the criteria

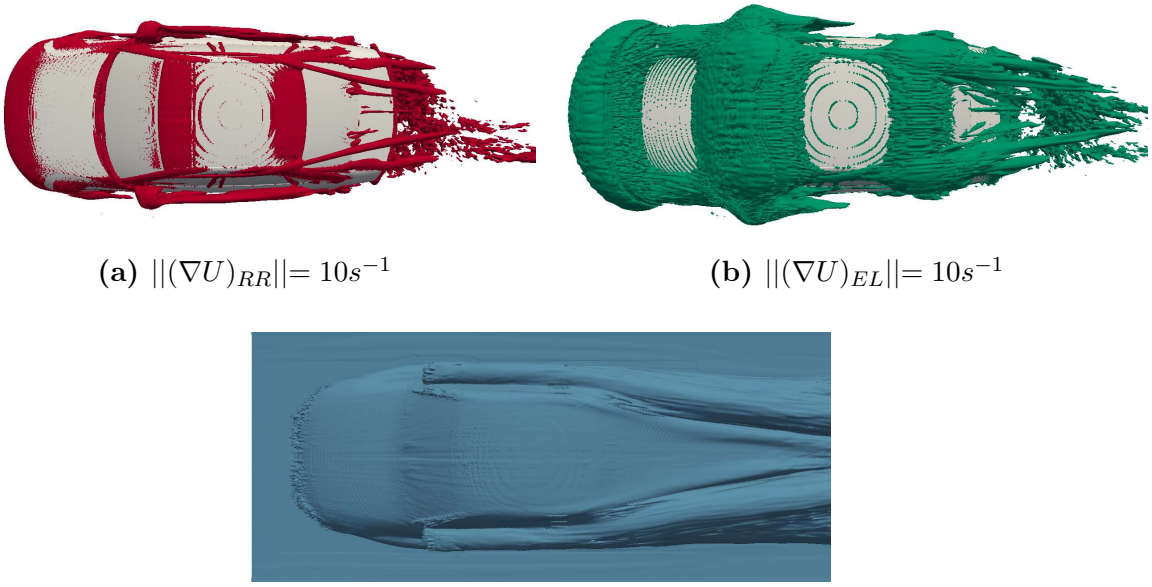

(a) $||(\nabla U)_{RR}||= 10s^{-1}$ **(b)** $||(\nabla U)_{EL}||= 10s^{-1}$

(c) $||(\nabla U)_{SH}||= 10s^{-1}$

Figure 2.7: Shear Maximizing Decomposition (SMD) of the time averaged flow around the DrivAer body.

applied to the rigid body rotation tensor $(\nabla U)_{RR}$ are chosen visually with respect to the size of the longitudinal vortices from the side mirrors.

The Q-Criterion applied to the full velocity gradient tensor and to the tensors of the SMD is shown in Fig. 2.8. As the magnitudes of the symmetric and skew-symmetric parts of the shear tensor are equal, the Q-criterion applied to a shear tensor is always zero. The vortices that are made up of shearing motion shown in Fig. 2.7c cannot be captured by the Q-criterion. The Q-criterion applied to the tensor of rigid body rotation reproduces the isosurfaces of $||(\nabla U)_{RR}||$ in Fig. 2.7a. Applied to the rate of elongation tensor, the Q-criterion is always negative. The inviscid part of the vortices cannot be detected. Nonetheless, the negative contribution of the elongational motion to the Q-criterion will influence its results.

Figure 2.9 shows the Δ-criterion applied to the tensors of the SMD. The shearing motion is found to have a strong contribution to the Δ-criterion. The structures in Fig.2.9b appear to be not only vortical structures, but also shear layers. The structures from the Δ-criterion applied to the rigid body rotation tensor are similar to the structures found in the original $||(\nabla U)_{RR}||$ isosurface of Fig. 2.7a. The Δ-criterion applied to the elongation tensor (Fig.2.9d) shows the inviscid deflection of the flow upstream the vehicle and elongational motion near the surface of the model. Although it does not show distinct coherent structures at the chosen isovalue, it also has an influence on the results of the Δ-criterion.

(a) Q-Criterion on ∇U : $Q = 200s^{-2}$
($Q_{min} = -3.4 \cdot 10^9 s^{-2}$, $Q_{max} = 5.1 \cdot 10^8 s^{-2}$)

$$Q((\nabla U)_{SH}) = 0$$

(b) Q-Criterion on $(\nabla U)_{SH}$: $Q = 0s^{-2}$
($Q_{min} = 0s^{-2}$, $Q_{max} = 0s^{-2}$)

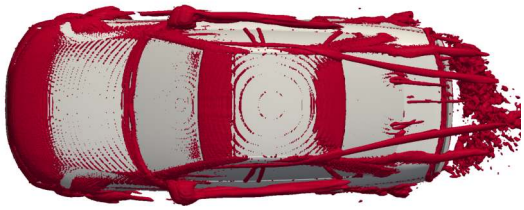

(c) Q-Criterion on $(\nabla U)_{RR}$: $Q = 50s^{-2}$
($Q_{min} = 0s^{-2}$, $Q_{max} = 3.9 \cdot 10^7 s^{-2}$)

(d) Q-Criterion on $(\nabla U)_{EL}$: $Q = -50s^{-2}$
($Q_{min} = -6.7 \cdot 10^7 s^{-2}$, $Q_{max} = 0s^{-2}$)

Figure 2.8: Q-Criterion on the tensors of the Shear Maximizing Decomposition

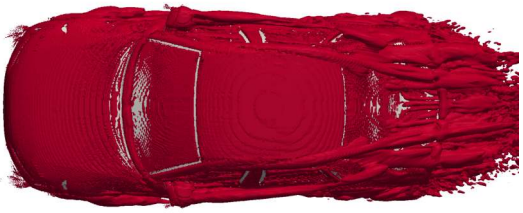

(a) Δ-Criterion on ∇U: $\Delta = 7 \cdot 10^5 s^{-6}$
($\Delta_{min} = -1.5 \cdot 10^{27} s^{-6}$, $\Delta_{max} = 1.7 \cdot 10^{26} s^{-6}$)

(b) Δ-Criterion on $(\nabla U)_{SH}$: $\Delta = 7 \cdot 10^3 s^{-6}$
($\Delta_{min} = 0s^{-6}$, $\Delta_{max} = 1.4 \cdot 10^{25} s^{-6}$)

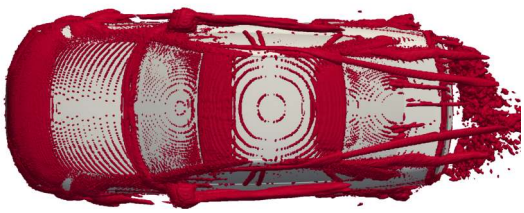

(c) Δ-Criterion on $(\nabla U)_{RR}$: $\Delta = 7 \cdot 10^3 s^{-6}$
($\Delta_{min} = 0s^{-6}$, $\Delta_{max} = 2.0 \cdot 10^{22} s^{-6}$)

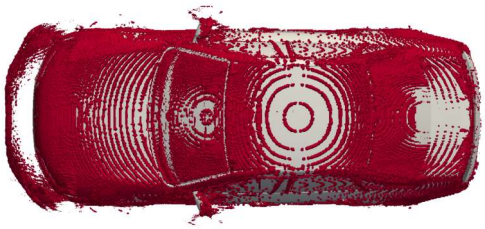

(d) Δ-Criterion on $(\nabla U)_{EL}$: $\Delta = 7 \cdot 10^3 s^{-6}$
($\Delta_{min} = -2.8 \cdot 10^{23} s^{-6}$, $\Delta_{max} = 6.2 \cdot 10^{23} s^{-6}$)

Figure 2.9: Δ-Criterion on the tensors of the Shear Maximizing Decomposition

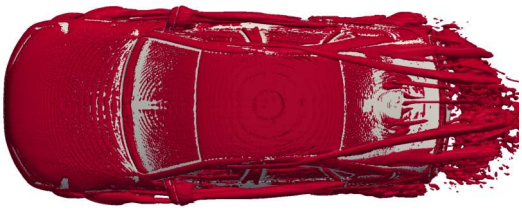

(a) λ_2-Criterion on ∇U: $\lambda_2 = -200s^{-2}$ ($\lambda_{2,min} = -9.0 \cdot 10^8 s^{-2}$, $\lambda_{2,max} = 1.0 \cdot 10^9 s^{-2}$)

(b) λ_2-Criterion on $(\nabla U)_{SH}$: $\lambda_2 = -10s^{-2}$ ($\lambda_{2,min} = -1.7 \cdot 10^7 s^{-2}$, $\lambda_{2,max} = 0s^{-2}$)

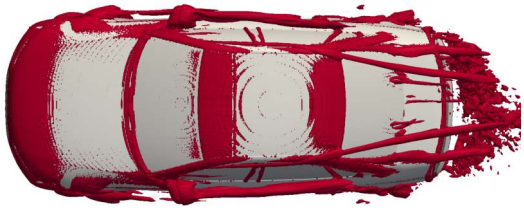

(c) λ_2-Criterion on $(\nabla U)_{RR}$: $\lambda_2 = -10s^{-2}$ ($\lambda_{2,min} = -7.6 \cdot 10^3 s^{-2}$, $\lambda_{2,max} = 0s^{-2}$)

(d) λ_2-Criterion on $(\nabla U)_{EL}$: $\lambda_2 = 10s^{-2}$ ($\lambda_{2,min} = 0s^{-2}$, $\lambda_{2,max} = 6.0 \cdot 10^7 s^{-2}$)

Figure 2.10: λ_2-Criterion on the tensors of the Shear Maximizing Decomposition

The contribution of shearing motion to the λ_2-criterion in Fig. 2.10b is not as strong as the contribution of shear to the Δ-criterion. Nonetheless, the structures at the C-pillars of the model also appear to be shear layers rather than vortical structures. The structures of the λ_2-criterion applied to $(\nabla U)_{RR}$ are again very similar to structures of $||(\nabla U)_{RR}||$ in Fig. 2.7a. When applied to the elongation tensor, the λ_2-criterion is always positive and therefore not able to detect inviscid vortices. The isosurface of a positive threshold, shown in Fig. 2.10d, shows a relatively strong influence of the elongational motion to the λ_2-criterion.

The isosurfaces of the λ_{ci}-criterion applied to the tensors of the SMD are shown in Fig. 2.11. The isosurface of the λ_{ci}-criterion applied to the shear rate tensor (Fig. 2.11b) is similar to the isosurface of the λ_2-criterion (Fig. 2.10b). The isosurface of the λ_{ci}-criterion applied to the rigid body rotation tensor resembles the original $||(\nabla U)_{RR}||$ isosurface in Fig. 2.7a. The λ_{ci}-criterion is not able to detect elongational motions. It can therefore not be biased by elongations but will also fail to detect the inviscid part of vortices.

Conclusion

All investigated vortex criteria have been found to be biased to some extend and are not applicable outside the vortex core region. The Q-criterion fails to detect vortical shearing motions but will not be influenced by shear layers. It is also not able to detect

(a) λ_{ci}-Criterion on ∇U: $\lambda_{ci} = 14s^{-1}$
($\lambda_{ci,min} = 0s^{-1}$, $\lambda_{ci,max} = 1.3 \cdot 10^4 s^{-1}$)

(b) λ_{ci}-Criterion on $(\nabla U)_{SH}$: $\lambda_{ci} = 7s^{-1}$
($\lambda_{ci,min} = 0s^{-1}$, $\lambda_{ci,max} = 5.3 \cdot 10^3 s^{-1}$)

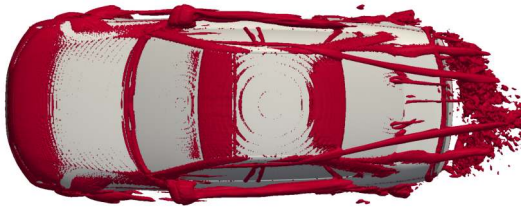

(c) λ_{ci}-Criterion on $(\nabla U)_{RR}$: $\lambda_{ci} = 7s^{-1}$
($\lambda_{ci,min} = 0s^{-1}$, $\lambda_{ci,max} = 5.4 \cdot 10^3 s^{-1}$)

$\lambda_{ci}((\nabla U)_{EL}) = 0$

(d) λ_{ci}-Criterion on $(\nabla U)_{EL}$: $\lambda_{ci} = 0s^{-1}$
($\lambda_{ci,min} = 0s^{-1}$, $\lambda_{ci,max} = 0s^{-1}$)

Figure 2.11: λ_{ci}-Criterion on the tensors of the Shear Maximizing Decomposition

inviscid vortices. Judging from Fig. 2.8d it is moderately influenced by elongational motions. The Δ-criterion appears to be considerably influenced by shearing motions as most of the structures found in Fig. 2.9d appear to be shear layers. The Δ-criterion is non-zero, when applied to the rate of elongation tensor in the three dimensional case. This means it could detect three dimensional inviscid vortices. As the Δ-criterion was not able to detect the outer region of the *Lamb–Oseen* vortex, elongational motions in car aerodynamics flow fields will probably have a predominantly biasing effect on the results of the Δ-criterion. The λ_2-criterion detects three dimensional shearing motions and is therefore able to identify shear vortices. As the structures in Fig. 2.10b appear to be at least partly shear layers, the λ_2-criterion is also biased by shearing motions. The λ_2-criterion is not able to detect inviscid vortices, but is influenced by elongational motions. The λ_{ci}-criterion shows a similar behavior as the λ_2-criterion when applied to the shear rate tensor but it is not affected by elongational motions. The $||(\nabla U)_{RR}||$-criterion, by design, fails to detect vortical shearing motions or inviscid vortices but its results are not affected by shearing or elongational motions. It relies on the presence of rigid body rotation and is therefore also only applicable in the core region of vortices. For car aerodynamics flow fields, the $||(\nabla U)_{RR}||$-criterion emphasizes the rigid body rotation in the vortex tubes over the curved redirection of the flow at curved surfaces (see Fig. 2.4) and therefore produces a clear picture of the vortices.

It has to be concluded that none of the investigated vortex criteria can be used for quantitative investigations of vortices. It has been shown that all criteria can even fail completely in some special cases. As relative motions near a point cannot be unambiguously linked to vortical or non-vortical motions it is questionable if an unambiguous vortex criterion based on the velocity gradient tensor is even possible. Nonetheless, it has to be noted that vortex criteria are widely used in the fluid mechanics literature and are used with success in the car aerodynamics development process. By reviewing the use of vortex criteria in the recent literature, it becomes evident that in most cases the use of vortex criteria is motivated by the goal to unveil the topological structure of the flow rather than by extracting and quantifying individual vortices (see e.g. Gnanaskandan and Mahesh [34], Jiang et al. [48] and [49] or Barnes et al. [5] as an exemplary selection). From this point of view, the Shear Maximizing Decomposition appears to be the most useful tool as it retains the complete information of the velocity gradient tensor and allows analyzing the coherent structures formed by shearing motions, elongational motions and rigid body rotations individually without being limited to the core region of vortices.

2.5 Modal Decompositions

One of the challenges in the investigation of coherent structures in turbulent bluff body flows is the presence of a large number of structures. Structures of different length and time scale interpenetrate and form the complex unsteady flow field. To investigate the causes and effects of individual flow processes, it is necessary to isolate the unsteady coherent structures connected with the process. Modal decompositions are pattern or structure recognition algorithms that decompose the flow into individual modes. The modes contain a subset of the dynamics of the flow and can be used to reconstruct a reduced order representation of the original flow field. In this thesis, the Proper Orthogonal Decomposition (POD) and the Dynamic Mode Decomposition (DMD) are used. The decomposition process of the POD is based on the total variance in the flow thus separating the modes of a velocity field by the hierarchy of the kinetic energy of its structures. The DMD is based on the frequency of the fluctuations in the flow. DMD modes therefore contain structures of common frequency.

The modal decompositions are implemented for fully distributed memory parallel processing. The flow fields of a parallel CFD run are loaded in parallel. The linear algebra computations are executed by the ScaLAPACK library for distributed memory parallel linear algebra computation [8]. The result files are again written in parallel.

2.5.1 Proper Orthogonal Decomposition

The idea of the Proper Orthogonal Decomposition (POD) was published by Pearson [82] at the beginning of the 20th century. The method has been independently reinvented and used in different contexts of data analysis. Depending on the field of application, it is described, amongst others, as Principal Component Analysis, Hotelling transform, Karhunen–Loève decomposition or Singular Value Decomposition. The method was introduced to fluid mechanics by Lumley [66] and Sirovich [96] and is a well established tool for the investigation of coherent structures in turbulent flow fields.

For the investigation according to the *method of snapshots* by Sirovich [96], the flow fields $\mathbf{v}_i$ of the time steps $\{t_1, t_2, ..., t_N\}$ are arranged as the column vectors of the snapshot matrix $\mathbf{V}_1^N$

$$\mathbf{V}_1^N = \{\mathbf{v}_1, \mathbf{v}_2, \mathbf{v}_3, ..., \mathbf{v}_N\}. \tag{2.71}$$

In this thesis, the POD is computed using a Singular Value Decomposition (SVD) of the snapshot matrix.

$$\mathbf{V}_1^N = \mathbf{U}\mathbf{\Sigma}\mathbf{W}^H. \tag{2.72}$$

The columns of $\mathbf{U}$ are the left singular vectors, the columns of $\mathbf{W}$ are the right singular vectors, $\mathbf{\Sigma}$ is a diagonal matrix with the singular values as the diagonal elements. To compute the POD modes, the left singular vectors $\mathbf{u}_i$ are weighted by their corresponding singular value σ_i.

$$\hat{\boldsymbol{\phi}}_{pod,i} = \mathbf{u}_i \sigma_i \tag{2.73}$$

The flow can be reconstructed by a multiplication of the matrix of POD modes $\mathbf{\Phi}_{pod}$ and the matrix of right singular vectors. A reduced order representation of the original flow can be computed by using a subset of the POD modes and their corresponding right singular vectors

$$\tilde{\mathbf{V}} = \mathbf{\Phi}_{\mathbf{pod}}\mathbf{W}. \tag{2.74}$$

Sign Indeterminacy

A frequently overlooked property of the Proper Orthogonal Decomposition is the sign indeterminacy of the POD modes. The scaling of the singular vectors of a singular value decomposition, just as the scaling of eigen vectors of a spectral decomposition, is arbitrary. Depending on the implementation of the SVD, the singular vectors are usually scaled to a norm of one. By weighting the left singular vectors with their corresponding singular value, a meaningful relative scaling of POD modes is established. Nonetheless, the sign of the POD modes will still be arbitrary. It is not possible, in general, to compute a sign of the singular vectors, as the SVD is only unique up to a reflection of the corresponding left and right singular vectors. Based on the intuitive assumption that the singular vectors should point into the direction of the majority of the vectors it represents, Bro et al. [11] proposed an algorithm for the reconstruction of a meaningful sign of singular vectors:

Step 1: The inner product of the left singular vector $\mathbf{u}_i$ and the data vectors $\mathbf{v}_1$ to $\mathbf{v}_N$ is computed and the signed square sum is taken.

for all $\mathbf{u}_i$ do

$\mathbf{s}_i^{left} \leftarrow \sum_{j=1}^{N} sign(\mathbf{u}_i^T\mathbf{v}_j)(\mathbf{u}_i^T\mathbf{v}_j)^2$

end for

Step 2: The inner product of the right singular vector $\mathbf{w}_i$ and the data vectors $\mathbf{v}_1$ to $\mathbf{v}_N$ is computed and the signed square sum is taken.

for all $\mathbf{u}_i$ **do**

$\mathbf{s}_i^{right} \leftarrow \sum_{j=1}^{N} sign(\mathbf{w}_i^T \mathbf{v}_j)(\mathbf{w}_i^T \mathbf{v}_j)^2$

end for

Step 3: If the singular vector and the data vectors point into the same direction ($(\mathbf{s}_i^{left}\mathbf{s}_i^{right}) \geq 0$) the sign is already correct. Else, the magnitudes of the previously computed square sums are compared and the sign of the larger value is used to correct the signs of the singular vectors.

for all $\mathbf{s}_i^{left}$ **do**

if $(\mathbf{s}_i^{left}\mathbf{s}_i^{right}) < 0$ **then**

if $|\mathbf{s}_i^{left}| < |\mathbf{s}_i^{right}|$ **then**

$\mathbf{s}_i^{left} \leftarrow -\mathbf{s}_i^{left}$

else

$\mathbf{s}_i^{right} \leftarrow -\mathbf{s}_i^{right}$

end if

end if

$\mathbf{u}_i^* \leftarrow sign(\mathbf{s}_i^{left})\mathbf{u}_i$

$\mathbf{w}_i^* \leftarrow sign(\mathbf{s}_i^{right})\mathbf{w}_i$

end for

The sign corrected POD modes are computed from the sign corrected left singular vectors

$$\boldsymbol{\phi}_{pod,i} = \mathbf{u}_i^* \sigma_i. \tag{2.75}$$

For a reconstruction of the flow with the sign corrected POD modes, the matrix of sign corrected right sigular vectors $\mathbf{W}^*$ is employed

$$\tilde{\mathbf{V}} = \boldsymbol{\Phi}_{\mathbf{pod}} \mathbf{W}^*. \tag{2.76}$$

The algorithm has been used in Peichl and Indinger [83] for the sign correction of POD modes of car aerodynamics flow fields. It has been found that the algorithm is computationally expensive when compared to the computation of the singular value decomposition as the algorithm includes a large number of dot products. Considering the computational resources needed for the unsteady CFD simulations, the POD with sign correction is still relatively cheap.

2.5.2 Dynamic Mode Decomposition

The Dynamic Mode Decomposition (DMD) has been originally proposed by Schmid in [92]. It has rapidly established itself as a method for the investigation of coherent structures in the fundamental research of fluid flows. The method has been used for a modal analysis of a car aerodynamics flow field by Peichl et al. in [84]. The description of the decomposition and reconstruction process of the DMD is based on the descriptions in [84] with minor corrections in Eq. 2.90.

The description of the decomposition process of the Dynamic Mode Decomposition follows the derivation of Schmid [92]. The description of the reconstruction follows Rowley et al. [89].

Decomposition

The flow field sequence is represented as a matrix $\mathbf{V}_1^N$ with the flow fields $\mathbf{v}_i$ as the column vectors (Eq. 2.77). The sequence has to be ordered and the separation time between the time steps Δt_{DMD} has to be constant.

$$\mathbf{V}_1^N = \{\mathbf{v}_1, \mathbf{v}_2, \mathbf{v}_3, ..., \mathbf{v}_N\} \tag{2.77}$$

With the assumption of a linear mapping $\mathbf{A}$ from one flow field to the next flow field $\mathbf{v}_{i+1} = A\mathbf{v}_i$, the matrix $\mathbf{V}_1^N$ can be constructed as a Krylov sequence,

$$\mathbf{V}_1^N = \{\mathbf{v}_1, \mathbf{A}\mathbf{v}_1, \mathbf{A}^2\mathbf{v}_1, ..., \mathbf{A}^{N-1}\mathbf{v}_1\}. \tag{2.78}$$

For a quasi-steady flow with small perturbations, the dynamic characteristic described by the Krylov sequence is equivalent to the dynamics described by the Matrix of flow fields. For a nonlinear process, the Krylov sequence is a linear tangent approximation. The Matrix $\mathbf{A}$ is the system matrix of the dynamic process. The aim of the DMD is to extract the dynamics described by the matrix $\mathbf{A}$.

With a sufficient number of linear independent flow fields, the snapshot matrix $\mathbf{V}_1^N$ describes the dominant features of the flow. Additional flow fields can then be described by a linear combination of the previous flow fields.

$$\begin{aligned}\mathbf{v}_N &= a_1\mathbf{v}_1 + a_2\mathbf{v}_2 + ... + a_{N-1}\mathbf{v}_{N-1} + \mathbf{r} \\ &= \mathbf{V}_1^{N-1}\mathbf{a} + \mathbf{r}\end{aligned} \tag{2.79}$$

with $\mathbf{r}$ as the residual vector. The matrix $\mathbf{V}_2^N$ with flow fields $\{\mathbf{v}_2, \mathbf{v}_3, ..., \mathbf{v}_N\}$ can be described as

$$\mathbf{V}_2^N = \mathbf{A}\mathbf{V}_1^{N-1} = \mathbf{V}_1^{N-1}\mathbf{S} + \mathbf{r}\mathbf{e}^T. \tag{2.80}$$

The matrix $\mathbf{S}$ is a companion matrix

$$\mathbf{S} = \begin{bmatrix} 0 & & & & a_1 \\ 1 & 0 & & & a_2 \\ & \ddots & \ddots & & \vdots \\ & & 1 & 0 & a_{N-2} \\ & & & 1 & a_{N-1} \end{bmatrix}, \tag{2.81}$$

it shifts the first $N-2$ columns of $\mathbf{V}_1^{N-1}$, $\{\mathbf{v}_1, \mathbf{v}_2, ..., \mathbf{v}_{N-2}\}$ forward in time to $\{\mathbf{v}_2, \mathbf{v}_3, ..., \mathbf{v}_{N-1}\}$. The last column vector of $\mathbf{V}_2^N$, $\mathbf{v}_N$ stems from the linear mapping by the coefficients $a_1, a_2, ..., a_{N-1}$. These coefficients are the only unknowns in the matrix $\mathbf{S}$. As the system matrix $\mathbf{A}$, the matrix $\mathbf{S}$ describes the dynamics of the flow. In the DMD according to Schmid [92], the matrix $\mathbf{S}$ is not computed directly by a QR Decomposition of the snapshot matrix $\mathbf{V}_1^{N-1} = \mathbf{Q}\mathbf{R}$ and $\mathbf{a} = \mathbf{R}^{-1}\mathbf{Q}^H\mathbf{v}_N$. Instead, the snapshot matrix is pre-processed by a singular value decomposition to avoid an ill-conditioned Algorithm,

$$\mathbf{V}_1^{N-1} = \mathbf{U}\mathbf{\Sigma}\mathbf{W}^H. \tag{2.82}$$

Substitution of the singular value decomposition in Eq. 2.80 and rearranging leads to

$$\mathbf{U}^H\mathbf{A}\mathbf{U} = \mathbf{U}^H\mathbf{V}_2^N\mathbf{W}\mathbf{\Sigma}^{-1} \equiv \tilde{\mathbf{S}}. \tag{2.83}$$

The singular value decomposition can also be used as a filter by restricting the projection basis to singular values above a prescribed fraction of the total variance in the dataset. The dynamic modes are computed by

$$\hat{\boldsymbol{\phi}}_i = \mathbf{U}\mathbf{y}_i \tag{2.84}$$

where $\mathbf{y}_i$ are the eigenvectors of $\tilde{\mathbf{S}}$ given by $\tilde{\mathbf{S}}\mathbf{y}_i = \lambda_i \mathbf{y}_i$.

Reconstruction

The dynamic modes according to Schmid [92] are not scaled and have arbitrary sign. Following Rowley et al. [89] the dynamic modes can be scaled such that

$$\mathbf{v}_i = \sum_{k=1}^{N} \lambda_k^{i-1} \boldsymbol{\phi}_k, \quad i = 1, ..., N \tag{2.85}$$

with the scaled modes $\boldsymbol{\phi}_k$. The first snapshot of the sequence is the sum of the modes

$$\mathbf{v}_1 = \sum_{k=1}^{N} \boldsymbol{\phi}_k. \tag{2.86}$$

This leads to a system of linear equations with the matrix of unscaled modes $\hat{\boldsymbol{\Phi}}$ and the scaling vector $\mathbf{d}$,

$$\hat{\boldsymbol{\Phi}}\mathbf{d} = \mathbf{v}_1. \tag{2.87}$$

The scaled dynamic modes $\boldsymbol{\phi}_i$ are then computed by

$$\boldsymbol{\phi}_i = \hat{\boldsymbol{\phi}}_i d_i. \tag{2.88}$$

The snapshot sequence can be reconstructed according to Eq. 2.85 as

$$\tilde{\mathbf{V}} = \boldsymbol{\Phi}\mathbf{T} \tag{2.89}$$

with the Vandermonde matrix $\mathbf{T}$,

$$\mathbf{T} = \begin{bmatrix} 1 & \lambda_1 & \lambda_1^2 & \dots & \lambda_1^{N-2} \\ 1 & \lambda_2 & \lambda_2^2 & \dots & \lambda_2^{N-2} \\ \vdots & \vdots & \vdots & \ddots & \vdots \\ 1 & \lambda_{N-1} & \lambda_{N-1}^2 & \dots & \lambda_{N-1}^{N-2} \end{bmatrix}. \tag{2.90}$$

Data Pre-Processing

It was found that the pre-processing of data has an important influence on the accuracy of the Dynamic Mode Decomposition. Most important is a low pass filtering of the data. While low frequency oscillations have no negative influence on the accuracy of the DMD and fall into a non-oscillating mode if their frequency is too low to be resolved, high frequency content that cannot be processed accurately by the method will contaminate the analysis and lead to wrong results. The cut-off frequency of the filter $f_{cut-off}$ has to be chosen such that only resolvable frequencies remain in the DMD analysis. The cut-off frequency is chosen relative to the sampling frequency of the data. This approach guaranties the resolvability of all fluctuations in the data after the filtering without additional user input.

For the DMD to produce satisfactory results, Schmid [92] found a sampling frequency of six times the inherent frequency of the dynamic process to be sufficient in some cases. An extensive study of Duke et al. [26] on synthetic waveforms recommends a sampling frequency of ≥ 20 times the inherent frequency of the process for modes with zero growth rate and ≥ 40 times the inherent frequency for modes with moderate growth rate. In this study, it has been found that filtering the data with a cut-off frequency of 20 times the sampling frequency of the data is sufficient for the predominantly undamped fluctuations in the flow around a car.

The low pass filtering approach used to pre-process the data in this thesis is a forward-backward filtering with a second order Butterworth low-pass filter which results in a zero-phase filter of 4th order (Oppenheim et al. [80]). In addition to the low pass filtering prior to the DMD analysis, the projection basis of the Singular Value Decomposition in the DMD algorithm (Eq. 2.83) is restricted to modes with a relative contribution of more than 1×10^{-4} % to the total variance of the flow. This is necessary to account for a rank deficient snapshot matrix. The chosen threshold of 1×10^{-4} % of the total variance in the flow is relatively low, as the low pass filtering step prior to the DMD analysis already removes most of the noise in the data.

Most DMD analyses found in the literature rely only on the filtering by a restriction of the POD basis after the SVD step in the DMD algorithm without explicitly pre-processing the data with a low pass filter. This approach is problematic, as it assumes that high frequency fluctuations in the flow have low total variance (or energy content). By removing singular vectors of low total variance it is assumed that no high frequency fluctuations are retained in the flow. In addition, the threshold for the SVD filtering has to be found iteratively as it depends on the physical phenomenon under investigation. In this thesis, a combination of a low pass filter and a very moderate restriction of the POD basis after the SVD step in the DMD algorithm was found to be the best procedure. The cut-off frequency of the low pass filter can be directly determined by the sampling frequency of the data and due to the low threshold of the SVD filtering the risk of biasing the data is

reduced. No user-supplied parameter is necessary for the pre-processing and SVD filtering in the DMD with this procedure. In the case of more than one field in one DMD analysis, it can be necessary to scale the individual fields to unit variance prior to the analysis, as the SVD filtering is based on the variance of the data. Especially in the case of fields of different dimensions, scaling the fields to unit variance is recommended to ensure a predictable behavior of the SVD filtering step.

Filtering the data in a forward-backward filtering approach with an IIR filter requires the full time step sequence to be stored. By filtering the data prior to writing it onto a storage medium, aliasing effects can be safely avoided. It should be possible to design a zero-phase forward FIR filter that can be used to filter the data during the CFD run. As an alternative, the phase response of an online IIR filter can be corrected after the DMD computation on the eigenvalues of the matrix $\tilde{\mathbf{S}}$ [1].

In the case of a spatially non-uniform data distribution (non-uniform grids), the data points in the snapshot matrix have to be weighted spatially. In the case of volume fields, the cell value is divided by the volume of the cell. In the case of surface fields, the value is divided by the area of the surface cell. The DMD is executed with the weighted data. The result fields of the DMD, the DMD modes or the reconstructed flow fields, then have to be multiplied by the cell value or the surface cell area.

Post-Processing

The result of the DMD is a set of complex dynamic modes $\boldsymbol{\phi}_i$ (Eq. 2.88) and a set of corresponding complex eigenvalues of the matrix $\tilde{\mathbf{S}}$, the so called Ritz values λ_i (Eq. 2.83). A reconstruction of the flow with a subset of the modes is possible using Eq. 2.85 to 2.89. The frequency of a mode can be computed from its complex eigenvalue λ_i

$$f_i = Im\left[\frac{\log \lambda_i}{\Delta t_{DMD}}\right]\frac{1}{2\pi}. \tag{2.91}$$

An oscillating process with non-zero frequency is represented by the DMD with a complex conjugate pair of modes. As the modes of a complex conjugate pair are identical except for the sign of the imaginary part, one mode of the pair is sufficient to describe the process and only modes with positive frequencies are considered in this thesis. By transforming the complex eigenvalues into the complex stability plane, additional information about the growth rate of the mode becomes available

$$\omega_i = \frac{\log \lambda_i}{\Delta t_{DMD}}. \tag{2.92}$$

[1] Correcting the shortcomings of an online filter after the execution of the DMD was proposed by A. Endres during his Master's thesis at the Chair of Aerodynamics and Fluid Mechanics at TU Munich.

The real part of ω_i is the growth rate of the mode. The fluctuations of modes with positive $Re\{\omega_i\}$ intensify over time, while modes with negative real part describe a decaying process. The imaginary part of ω_i is the angular frequency of the mode with $Im\{\omega_i\} = 0$ for a non-oscillating process. Unphysically high damping rates (negative growth rates) can be an indication for a low signal to noise ratio resulting in an inaccurate computation of the DMD. In the case of car aerodynamics with largely undamped vortex shedding, the growth rates should be close to zero. As the computation of the DMD is not totally accurate it can be practical to artificially correct growth rates smaller than the error of the analysis to zero prior to the reconstruction of the flow. The advantage of the correction is that only one period of the fluctuation needs to be reconstructed for modes of zero growth rate as the fluctuation is repeated unchanged every period.

An important characteristic of the modes are the modes amplitudes. Usually, the scaling vector $\mathbf{d}$ computed in Eq 2.87 is used directly as amplitudes of modes. The scaling vector $\mathbf{d}$ can also be computed as a post-processing step with the elements d_i in the vector being the norm of the corresponding dynamic mode $\boldsymbol{\phi}_i$.

$$d_i = \sqrt{\sum_{k=1}^{M} \phi_{k,i}^2}. \tag{2.93}$$

In the case of non spatially weighted DMD modes, the weighting has to be considered in computing the norm.

The amplitudes of the modes are the most important criterion for judging the importance of a mode for the flow process under investigation. The usefulness of the DMD as a data mining method is highly dependent on the criterion under which the modes are rated as important for the investigated flow process. The current selection criterion is the (spatially weighted) norm of the modes. Replacing this criterion with a more sophisticated heuristic is a promising improvement to the data mining capability of the DMD.

3 Applications

The chapter on applications shows how the methods, introduced in chapter 2, are to be applied in car aerodynamics. The applications are test cases with different degree of complexity and realism. The first case, the surface mounted cube, is used to show how the methods are applied to a well known bluff body flow around a simple geometry. It establishes a connection to investigations already present in the literature. The second test case, the case of the SAE car bodies, is an application of the methods to a highly simplified generic car model. This case shows an application of the methods to different variants of one geometry. In the third case, the DrivAer test case, the methods are applied to a realistic generic vehicle. This test case shows how the methods can be used to investigate the unsteady details of the flow around a car geometry similar to the geometry of a production car. The fourth case, a convertible car model, is an application of the methods to a geometry based on a real production car. This test case investigates a fluctuation, observed in preceding wind tunnel tests.

3.1 Surface Mounted Cube

The presented test case, a cube mounted on the surface of a channel, is used as a simple example of a bluff body flow. This test case was extensively studied during the last decades. Early experimental investigations are presented by Castro and Robins [12] with a cube in different atmospheric boundary layers to investigate the effect of turbulence in the oncoming flow or by Hunt et al. [41] who studied the flow topology using critical point theory. Martinuzzi and Tropea [70] used a cube in a fully developed channel flow and published detailed results for time averaged quantities. Other experimental contributions are from Larousse et al. [63] or Hussein and Martinuzzi [43]. LES results of a cube in fully developed channel flow are from Kishan and Ferziger [94], Rodi et al. [87] or Krajnović and Davidson [60].

Modal investigations in subdomains around a surface mounted cube are published by Manhart and Wengle [69] who executed a POD analysis in a subvolume on top of the cube, Alfonsi et al. [2] published a POD analysis in two subvolumes in front and at one side of the cube or by Muld et al. [74] who published POD and DMD analyses in a subvolume containing the cube.

3.1.1 Setup

The computational domain is sketched in Fig: 3.1. A cubic, sharp edged, bluff body is mounted on the wall of a channel. With the height of the cube H, the height of the channel $h = 2H$ the streamwise extend of the domain is $15H$ with $x_1 = 4.5$ and $x_2 = 10.5$, the spanwise extend is $10H$.

While most of the unsteady simulations of this test case found in literature use instantaneous results from channel simulations as incoming flow, the incoming flow here is the time averaged velocity profile of the experiments, similar to the boundary conditions used by Krajnović and Davidson [60].

The Reynolds number is $Re = 1 \cdot 10^5$ based on the channel height.

Numerical Setup

A block structured grid with approx. 3.4 million cells is used in the presented test case. The cell size in the vicinity of the cube is $\frac{\Delta x}{H} < 4.4 \cdot 10^{-2}$. Outside the prism layer, a cube edge is resolved with 29 cell nodes. Prism layers are present at the cube, at the bottom and at the top of the domain. The dimensionless wall distance y^+ of the wall nearest cells are below one in the whole domain. The wall normal size of the cells increase in the prism layers with a factor of < 1.25 until a cubic cell shape is reached.

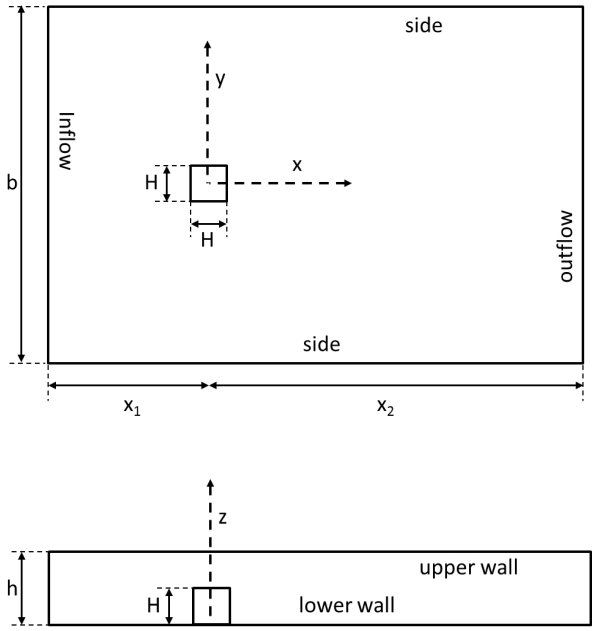

Figure 3.1: Geometry of the surface mounted cube: $\frac{h}{H} = 2$, $\frac{x_1}{H} = 4.5$, $\frac{x_2}{H} = 10.5$, $\frac{b}{H} = 10$.

The discretization scheme for convective terms is a second order central differencing scheme with a small amount of upwind to reduce oscillations on coarser grids. The gradients are computed using the Gauss theorem were the surface values are interpolated with a second order linear interpolation. The diffusive terms are approximated using a stabilized over relaxed approach to account for the non-orthogonality of the mesh in regions where the mesh changes to an O-type grid. The scheme to discretize the time derivatives is second order implicit. The time step is adjusted to result in a CFL number smaller than 1.

The turbulence model used is the Spalart-Allmaras DDES model as described in section 2.2.2. The wall normal eddy viscosity profiles have been checked against the velocity profile of the boundary layers to ensure the proper functioning of the shielding function of the turbulence model.

Boundary Conditions At the inlet boundary condition, the time averaged velocity profile of an independent channel flow simulation is imposed. The velocity profile matches the velocity profile of the experiments and provides the velocity data without the need for interpolation. As inlet values of the modified eddy viscosity $\tilde{\nu}$, the time averaged profile of $\tilde{\nu}$ of the channel simulation is used. It is known that a channel simulation with the DDES turbulence model can produce artificially low turbulent viscosity as the instability in the flow can be too low to maintain the fluctuations. Rumsey and Spalart [90] recommend a free stream eddy viscosity ratio of $\frac{\tilde{\nu}_\infty}{\nu_\infty} = 3$ as inlet boundary value for aerodynamics simulations. The lowest eddy viscosity ratio of the inlet profile is 3 and falls to 2.5 directly

in front of the cube. This is considered acceptable. The boundary condition of pressure at the inlet is a zero gradient Neumann condition.

At the outlet of the computational domain, the velocity boundary condition is a zero gradient Neumann boundary condition that is modified such that it avoids backflow into the domain. In case of backflow, the velocity vector is set to zero. The boundary condition of the modified eddy viscosity $\tilde{\nu}$ is also a zero gradient Neumann boundary condition. The pressure at the outlet is set to zero.

At the top wall, the bottom wall and the cube the boundary condition of velocity and modified eddy viscosity is of Dirichlet type set to a value of zero. The boundary condition of pressure is a zero gradient Neumann boundary condition.

The side walls are treated as slip walls. Here, the velocity components tangential to the wall are handled with a zero gradient Neumann condition, while the normal velocity components are set to zero. The modified eddy viscosity and pressure are handled with zero gradient Neumann boundary conditions.

3.1.2 Results

Time averaged flow

Statistical quantities of the mean flow are computed to be compared to experimental results published by Martinuzzi and Tropea [70] and numerical results by Krajnović and Davidson [60]. Krajnović and Davidson executed LES simulations with similar boundary conditions as in the present study with two different one-equation subgrid models on three different grids. The results presented here are compared to the results of Krajnović and Davidson with the *Dynamic One Equation Model (OEM)* [23] and the *Localized Dynamic k_{sgs}-Equation Model (LDKM)* [71] on the finest grid. The Fig. 3.2 shows the streamwise velocity component $\frac{<u>}{U_\infty}$, the upward velocity component $\frac{<w>}{U_\infty}$ and the turbulent stresses $\frac{<u'u'>}{U_\infty^2}$, $\frac{<w'w'>}{U_\infty^2}$, $\frac{<u'w'>}{U_\infty^2}$ along the vertical axis z at four streamwise positions. With the origin of the coordinate system in the middle of the cube on the ground, at $\frac{x}{H} = 0$ in center of the cube, $\frac{x}{H} = 0.5$ at the trailing edge and at two positions behind the cube: $\frac{x}{H} = 1.5$ and $\frac{x}{H} = 3.5$. The averaging time for the simulation results is $450\frac{H}{U_\infty}$ which corresponds to 90 shedding cycles for a Strouhal number of 0.2.

The first row of Fig. 3.2 shows the streamwise velocity component $\frac{<w>}{U_\infty}$. For the first three positions, results of two different measurements of Martinuzzi and Tropea are available. In the first picture ($\frac{x}{H} = 0$) the measurements differ close to the cube. The results of Krajnović and Davidson follow the measurement indicated by crosses while the simulation results of the presented investigation follow the measurement indicated by circles. This is due to two vortices found in the present study that are not reported by Krajnović

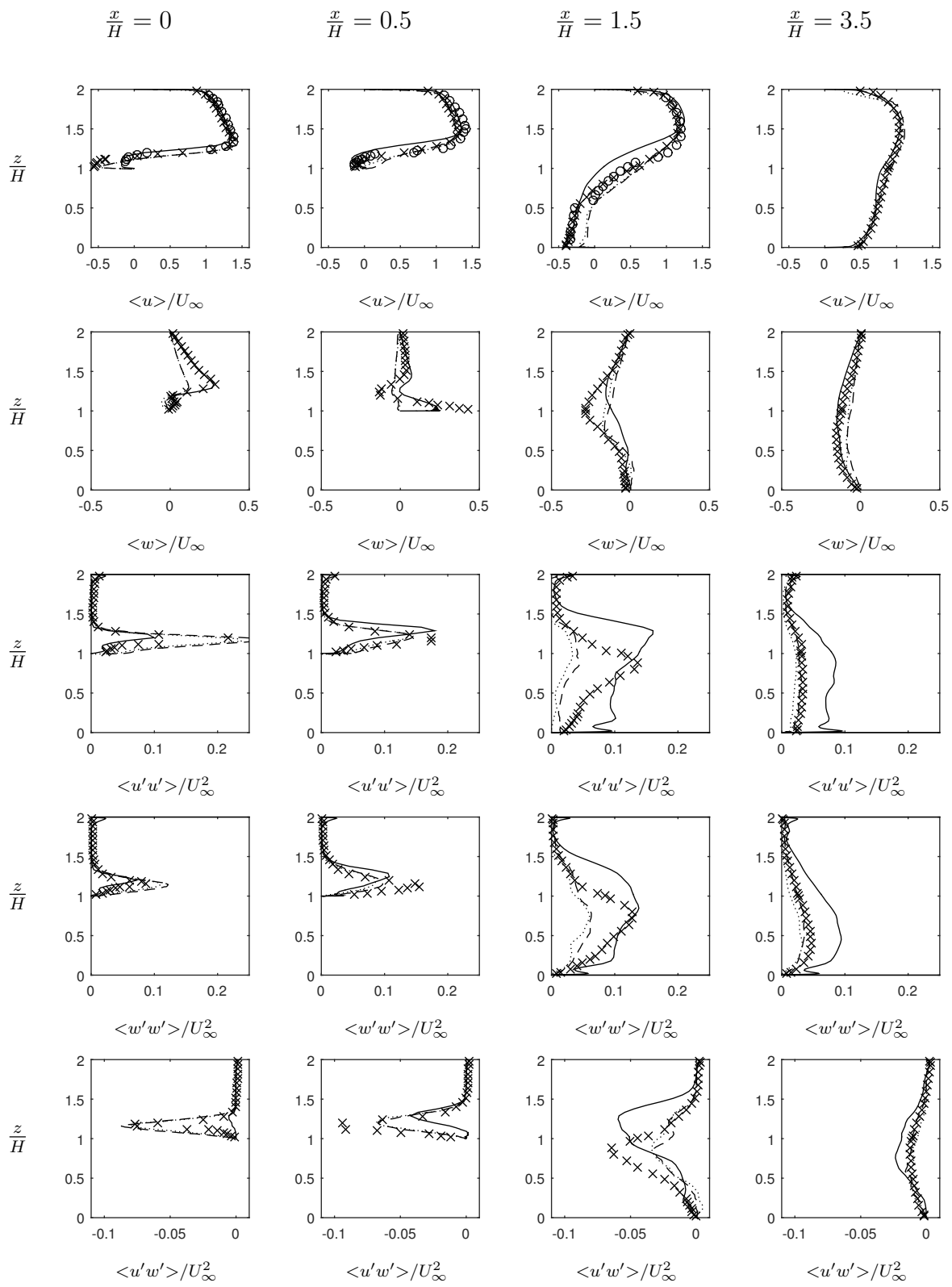

Figure 3.2: Comparison against experimental results (Martinuzzi and Tropea [70]) and results from LES simulations with comparable boundary conditions (Krajnović and Davidson [60]). Solid lines: DDES simulation, symbols: Experimental results [70], dashed lines: LDKM simulation [60], dotted lines: OEM simulation [60].

and Davidson. The fact that two independent measurements with the same measurement equipment and setup indicate different flow structures, show a strong dependency of the test case on initial and boundary conditions. The streamwise velocity component is in good agreement with the experimental results for the positions $\frac{x}{H} = 0$, $\frac{x}{H} = 0.5$ and $\frac{x}{H} = 3.5$. At position $\frac{x}{H} = 1.5$ deviations can be seen between $\frac{z}{H} = 0.5$ and $\frac{z}{H} = 1.5$ while the results of Krajnović and Davidson differ below $\frac{z}{H} = 0.5$ from the experimental results.

The upward velocity component $\frac{<w>}{U_\infty}$ shown in the second row of Fig. 3.2 is in good agreement at position $\frac{x}{H} = 0$ and $\frac{x}{H} = 3.5$ and shows deviations at positions $\frac{x}{H} = 0.5$ and $\frac{x}{H} = 1.5$. The LES results show a larger deviation to the experiments at the first two positions.

The turbulent stresses generally match the experimental results not as good as the velocities. A general observation is that the stresses are underpredicted at the first position, reach a realistic magnitude directly behind the cube and are overpredicted downstream the cube. The underestimation of turbulent stresses at the first position is caused by the stationary inlet conditions without resolved fluctuations. The overestimation of the stresses at the last down stream position can be caused by a low turbulent viscosity at the inlet boundary condition and, subsequently, a too low damping of the resolved fluctuations.

Comparing the statistical quantities of the DDES simulation presented here and especially the velocity components with the results of the LES simulations, the DDES can be said to produce competitive results for the presented test case.

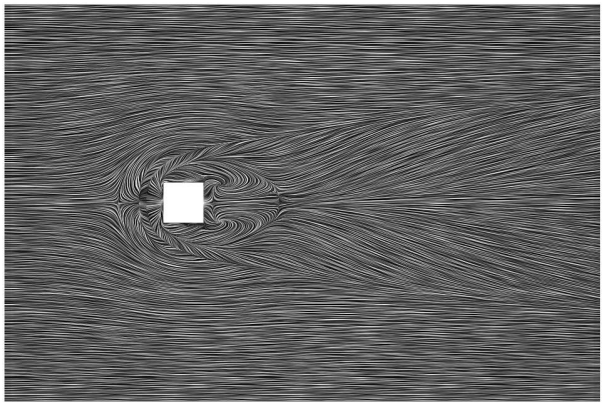

Figure 3.3: Line Integral Convolution (LIC) of the wall shear stress on the bottom of the computational domain

Line Integral Convolution (LIC) pictures on the wall shear stress vector field are shown for the bottom of the domain in Fig. 3.3 and for the surface of the cube in Fig 3.4. Important flow features in the flow are the horseshoe vortices. On the bottom of the domain, four lines are visible in front of the cube. The first line upstream is the primary detachment line of the flow in front of the first horseshoe vortex. The second line, a reattachment line, separates the first from the counter rotating second horseshoe vortex. The third line is again a separation line, indicating the next vortex. The fourth line, directly in front of

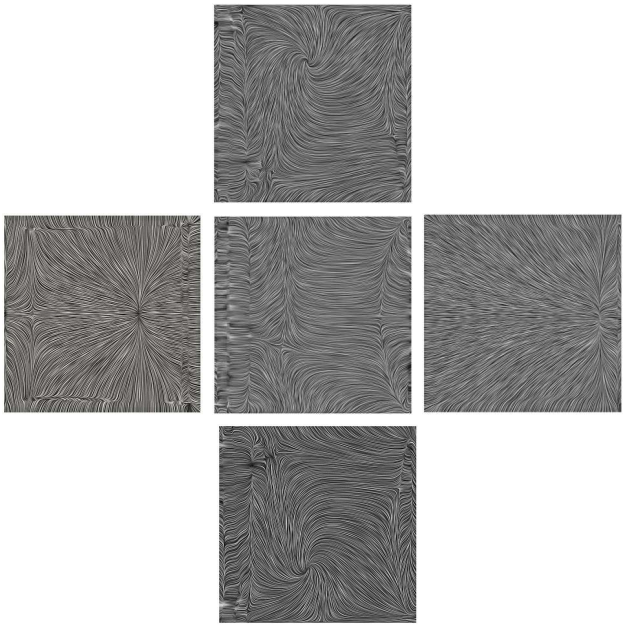

Figure 3.4: Line Integral Convolution (LIC) of the wall shear stress on the cube surface. Left: leading side, right: trailing side, top: left side in the direction of flow, bottom: right side in the direction of flow, center: top of the cube.

the cube is blurred and not clearly visible. Considering the LIC pattern on the leading face of the cube in Fig 3.4, this reattachment line has to be present in front of the cube.

In the wake of the cube, two lines are visible. The first line directly downstream is a detachment line that separates the first vortex behind the cube from an arch shaped recirculation vortex. The second line is the primary reattachment line of the main flow behind the cube. Spiraling pattern on both sides of the near wake show the mark of the "legs" of the arch shaped recirculation vortex on the wall shear stress on the ground. A similar spiraling pattern is visible on the sides of the cube (top and bottom picture in Fig. 3.4) here, recirculation vortices reach from the sides of the cube to the ground. The correspondent spiraling pattern on the ground is not clearly visible but is assumed to exist in the blurred regions directly beside the cube on the ground. Other features found in the LIC pictures of Fig. 3.4 are the stagnation point in the upper middle and separation lines at the edges of the leading face of the cube. The detachment and reattachment lines of the vortices at the edges of the side faces and the top face. And the vertical lines, leading to the recirculation zone at the bottom of the trailing face, indicating the downwash in the near wake of the cube. The LIC pattern in the center of the top face does not correspond to dominant structures of the flow. Here the time averaged wall shear stress is near zero.

The pictures of Fig 3.5 are Line Integral Convolutions on slices of the time averaged velocity field. The upper picture shows the $\frac{y}{H} = 0$ plane in the center of the cube. The lower picture shows the $\frac{z}{H} = 0.5$ plane, half the cube height above the ground. The pictures are colored by the normal component of rigid body rotation computed with the Shear Maximizing Decomposition. The upper picture shows the four horseshoe vortices in front of the cube. Here, the third vortex in the direction of the flow is clearly the

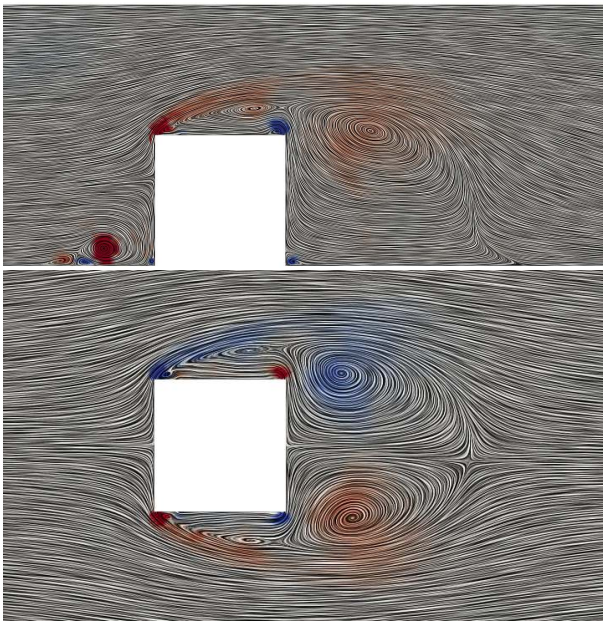

Figure 3.5: Line Integral Convolution (LIC) of the time averaged velocity colored by normal component of rigid body rotation from the Shear Maximizing Decomposition. Blue: negative rotation, red: positive rotation. Color range from blue $-2s^{-1}$ to red $2s^{-1}$.

strongest vortex. The vortices at the edges of the cube are also found to be strong, while the recirculation vortices are relatively weak. The rigid body rotation in the bended flow above the edge vortices and recirculation vortices is found to be as strong as the vortices itself. This is also true for the vortices shown in the lower picture.

(a) $||(\nabla U)_{RR}|| \frac{H}{U_\infty} = 0.6$

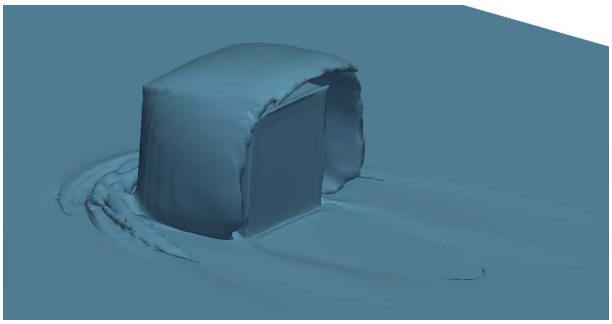

(b) $||(\nabla U)_{SH}|| \frac{H}{U_\infty} = 5$

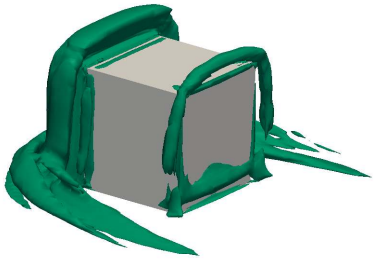

(c) $||(\nabla U)_{EL}|| \frac{H}{U_\infty} = 1.5$

Figure 3.6: Isosurfaces of $||(\nabla U)_{RR}||$, $||(\nabla U)_{SH}||$ and $||(\nabla U)_{EL}||$ of the time averaged velocity field around the cube.

To summarize the flow topology of the time averaged flow, isosurfaces of the magnitudes of the SMD tensors are shown in Fig. 3.6. In Fig. 3.6a, the isosurface of the magnitude of the tensor of rigid body rotation is shown. Clearly visible is the main horseshoe vortex and the secondary horseshoe vortices in front of the cube. The cube itself is covered by the isosurface of $||(\nabla U)_{RR}||$ in the bended flow around the cube. At the edges, the edge vortices are noticeable. On top of the cube and the sides, recirculation vortices are present as well as the arch shaped vortex in the wake of the cube.

The dominant structure in the visualization of the shear magnitude $||(\nabla U)_{SH}||$ in Fig. 3.6b is the main shear layer starting from the leading edges of the cube and following the flow into the wake. The shearing motion in the horseshoe vortices as well as the shear between the rotational motion of the horseshoe vortices and the surrounding flow are visible in front of the cube. Also visible is the shear at the bottom of the domain, the shear at the top wall has been clipped for better visibility.

The magnitude of elongation $||(\nabla U)_{EL}||$ is shown in Fig. 3.6c. The flow decelerates to the stagnation point and is redirected over the leading edges and over the trailing edges of the cube. The magnitude of elongation consists mainly of the inviscid part of the redirection of flow. Due to the elongation around and in the vortices, the horseshoe vortices are also visible in this picture.

All vortices described by Martinuzzi and Tropea [70] are present in the flow. While Krajnović and Davidson [60] report only two vortices in front of the cube, four vortices are found here. This difference is already explained by Martinuzzi and Tropea who found that the flow alternates between two different states, one state with two horseshoe vortices and one state with four horseshoe vortices in front of the cube.

Unsteady Flow

The structures in the unsteady flow around the cube are investigated with the Proper Orthogonal Decomposition (POD) and the Dynamic Mode Decomposition (DMD). The POD has been used by Manhart and Wengle [69], Alfonsi et al. [2] and Muld et al. [74] for investigations of subvolumes around the cube. The DMD has been used in the analysis of Muld et al. [74].

Proper Orthogonal Decomposition on the Velocity Vector Field The POD is applied on the velocity vector field in the whole domain with $N_{POD} = 800$ time steps, a time step length of $\Delta t_{POD}\frac{U_\infty}{H} = 0.1$ and a total time span of $T_{POD}\frac{U_\infty}{H} = 80$. As the grid used in the analysis has varying density, the velocity data has to be weighted spatially. To allow for a comparison of the POD results with the results of the DMD, the time step data is filtered with a 4th order low-pass filter with a ratio of cut-off frequency to Nyquist

frequency of 0.1. A POD analysis without pre-filtering the data produced very similar results for the first 10 Modes.

The relative distribution of total variance over the proper orthogonal modes is shown in Fig. 3.7. The first mode of the decomposition, the mean flow, contains 99.6% of the total variance in the dataset. The second mode contains 0.04%. It is a common observation for POD that one flow phenomenon is represented by two or more modes. The fact that the second and third mode have similar total variance, is an indication that they represent a common flow phenomenon. Similar content of total variance can also be observed for higher modes e.g. for modes 5 and 6 or modes 8 and 9.

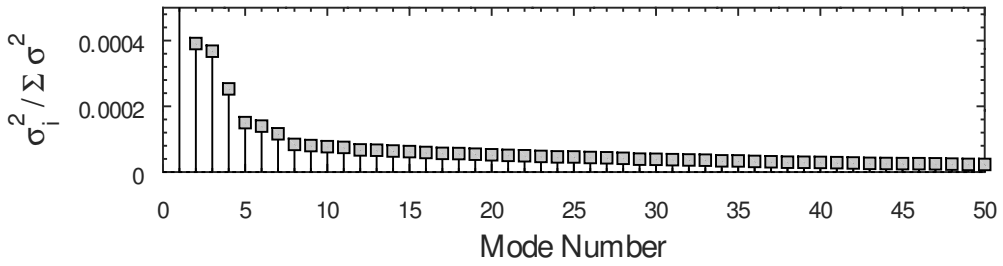

Figure 3.7: Relative variance of the Proper Orthogonal Modes. Variance of the modes normalized by sum of variance over all modes.

An overview over the proper orthogonal modes 2 to 8 is given in Fig 3.8. The pictures show isosurfaces of the velocity components u (streamwise), v (spanwise) and w (upward direction). The modes are scaled such that the first mode matches the time averaged flow. The signs of the modes are reconstructed according to the description in section 2.5.1, sign correction is indicated in the left column of Fig. 3.8.

The modes 2 and 3 in Fig. 3.8 show a streamwise pattern of positive and negative isosurfaces. The modes are similar; isosurfaces of mode 3 are shifted in the streamwise direction when compared to mode 2. The flow phenomenon described by these modes is the dominant vortex shedding in the flow. The flow pattern found in modes 2 and 3 were also found by Manhart and Wengle in [69]. The isosurfaces of Mode 4 are connected, streamwise elongated regions indicating an oscillating process in the whole wake of the cube. Modes 5 and 6, again, show a streamwise pattern of positive and negative isosurfaces. Here, the vortex shedding process has a smaller length scale then found in modes 2 and 3. Mode 7 has similarities to mode 4 with longitudinally oriented, connected regions. Mode 8 appears to be a vortex shedding process with even smaller length scale then found in mode 5 and 6.

From Fig. 3.7 it can be seen that the total variance of the modes falls with increasing mode number rapidly for the first 7 modes. While the first modes are directly induced by the shape and length scale of the geometry, the higher modes appear to evolve from

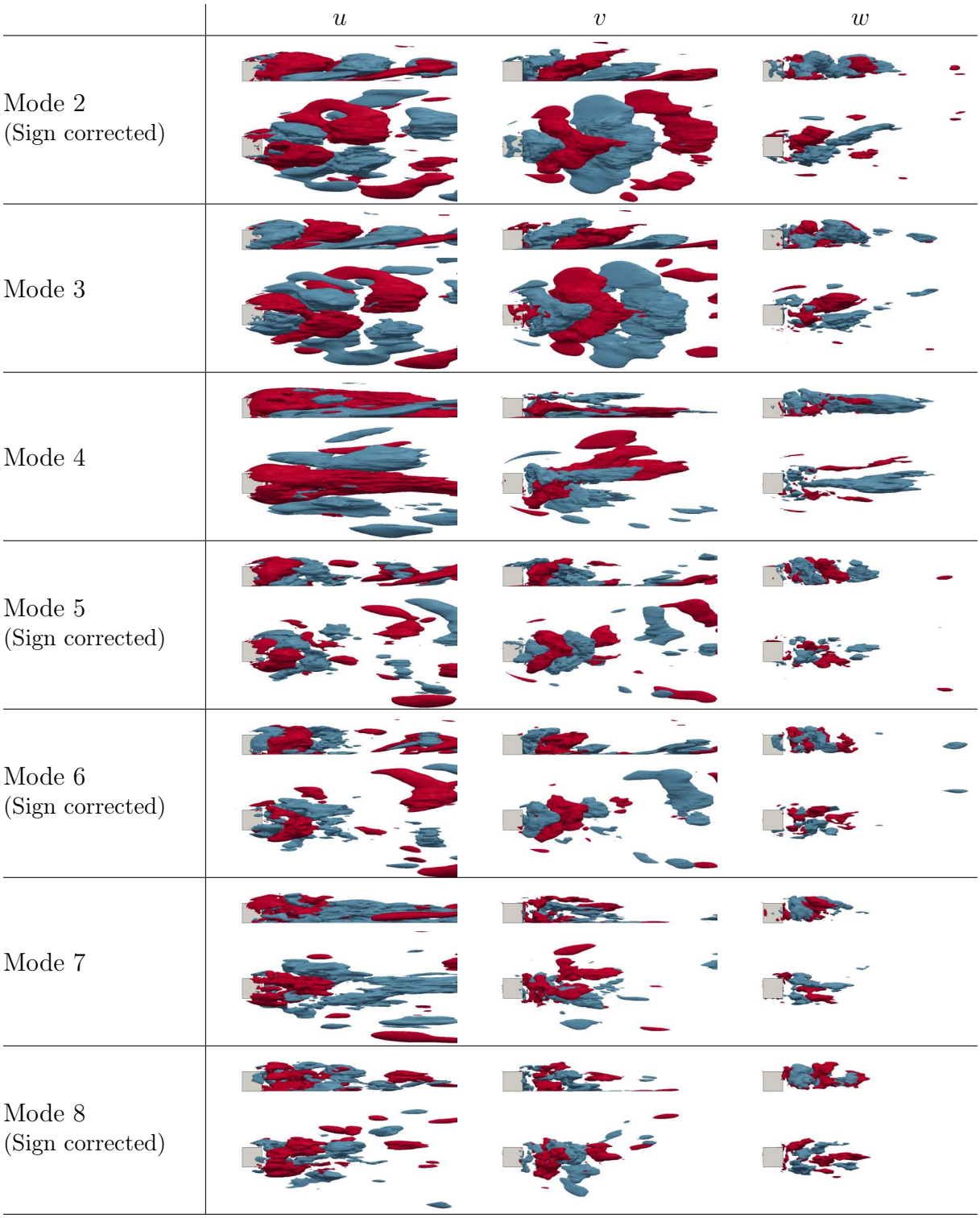

Figure 3.8: Isosurfaces of velocity components u, v and w of POD modes $2-8$. Isovalues normalized by bulk velocity U_∞. Red: $+0.04$, blue: -0.04. Upper pictures in row: side view, lower pictures in row: top view.

the shear layers around the body. With increasing mode number, the length scale of the structures decreases.

Applied to the flow around the surface mounted cube, the POD is able to extract the most dominant flow structures and reproduces the unsteady "skeleton" of flow. The algorithm of the POD based on the singular value decomposition is numerically stable and relatively easy to apply. The POD decomposes the flow based on the orthogonality condition and the hierarchy of total variance in the modes. For modes with a high contribution to the total variance, this is sufficient to reveal their contribution to the dynamics of the flow and allow connecting the mode to a distinct flow phenomenon like a vortex shedding process. For modes with lower contribution to the total variance, the dynamic evolution and contribution to the flow is usually not as clear. The modes have similar visual appearance and similar total variance. For these modes, the POD lacks a criterion to connect them to distinct flow phenomena and allow for a reconstruction of a selected part of the dynamics of the flow.

Dynamic Mode Decomposition on the Velocity Vector Field For a direct comparison with the results of the POD, the DMD has been applied on the same set of time steps of the velocity vector field in the whole domain with $N_{DMD} = 800$ time steps, a time step length of $\Delta t_{DMD} \frac{U_\infty}{H} = 0.1$ and a total time span of $T_{DMD} \frac{U_\infty}{H} = 80$. As in the POD analysis, the time step data is filtered with a 4th order low-pass filter with a ratio of cut-off frequency to Nyquist frequency of 0.1. After the singular value decomposition in the DMD algorithm, the projection basis is restricted to modes with a relative contribution of more than $1 \times 10^{-4}\,\%$ to the total variance of the flow. This threshold is high enough to safely account for a rank deficiency in the matrices but small enough to not discard physically meaningful information.

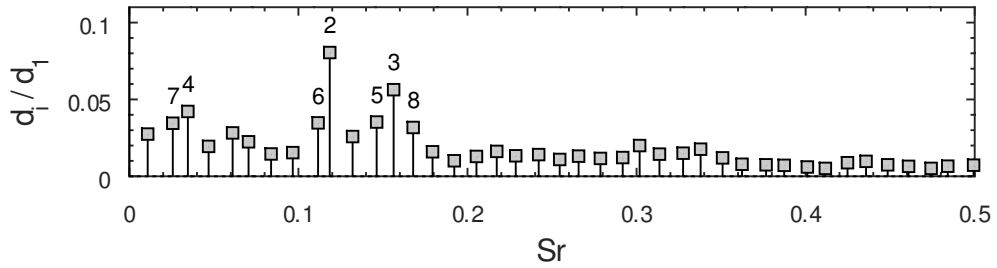

Figure 3.9: Relative amplitude over Strouhal number. Spatially weighted amplitudes of the dynamic modes normalized by amplitude of the first mode. Mode numbers by decreasing amplitude.

The relative amplitude of the dynamic modes and their corresponding Strouhal number is shown in Fig. 3.9. The amplitudes are computed as the spatially weighted norm of the mode. The modes are numbered by decreasing amplitude. Mode 1 is, again, the mean flow

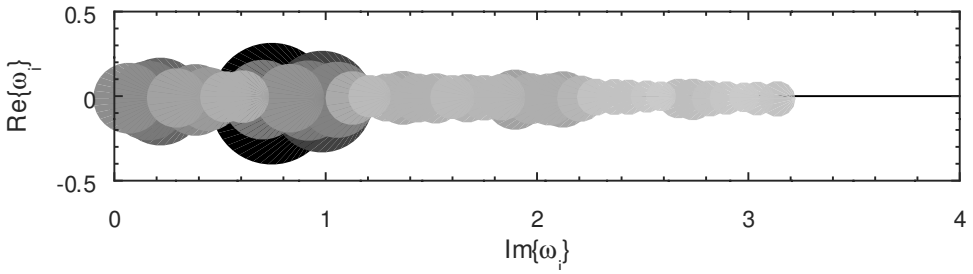

Figure 3.10: Eigenvalues of the Dynamic Modes transformed into the complex stability plane. Size and darkness of the symbols indicate the amplitude of the mode.

with a Strouhal number of $Sr = 0$. The first oscillating mode is mode 2 with Strouhal number of $Sr = 0.119$. Hussein and Martinuzzi [43] identified in their experiments a dominant vortex shedding from the lateral walls of the cube with a Strouhal number of $Sr = 0.145$. Krajnović and Davidson [60] report Strouhal numbers for the side force on the cube for the aforementioned OEM and LDKM turbulence models on different grids between $Sr = 0.092$ and $Sr = 0.146$. With $Sr = 0.115$ for the LDK model and $Sr = 0.146$ for the OE model on the finest grid.

The spectrum of eigenvalues transformed into the complex stability plane is shown in Fig. 3.10. The imaginary part of ω is the angular frequency of the mode. The real part of ω is the exponential growth rate. Positive values indicate growth, negative values indicate decay of the structures found in the mode. The structures of aerodynamics flows around bluff bodies are usually decaying or show growth rates near zero. Most relevant in car aerodynamics are usually modes with near zero growth rate. These modes describe the persistent fluctuating processes in the flow. Here, the growth rates of all modes in the time window of the analysis are zero or near zero. The DMD is sensitive to signal to noise ratio. A highly dampened spectrum can be an indication for a high noise level in the data caused for example by a high noise level in the input data, rank deficient matrices or too low a sampling rate for the highest fluctuations in the flow field sequence.

Isosurfaces of the velocity components u (streamwise), v (spanwise) and w (upward direction) of the dynamic modes 2 to 8 are shown in Fig 3.11. Mode 2 is the dominant fluctuation in the flow with a Strouhal number of $Sr = 0.119$. It describes a vortex shedding process from the side walls of the cube and is similar in structure and length scale to POD modes 2 and 3 in Fig. 3.8. Mode 3 is also a vortex shedding process from the sidewalls but with higher Strouhal number and smaller length scale then mode 2. It is similar to POD mode 5 and 6. Mode 4 is, with a Strouhal number of $Sr = 0.035$, a low frequency oscillation. Its structures have similarities to POD mode 4 and POD mode 7. The flow phenomenon of Mode 5 cannot be clearly identified. The Strouhal number and length scale of the structures point to a vortex shedding process while the lack of symmetries and no clear positive-negative pattern could be explained by two interpene-

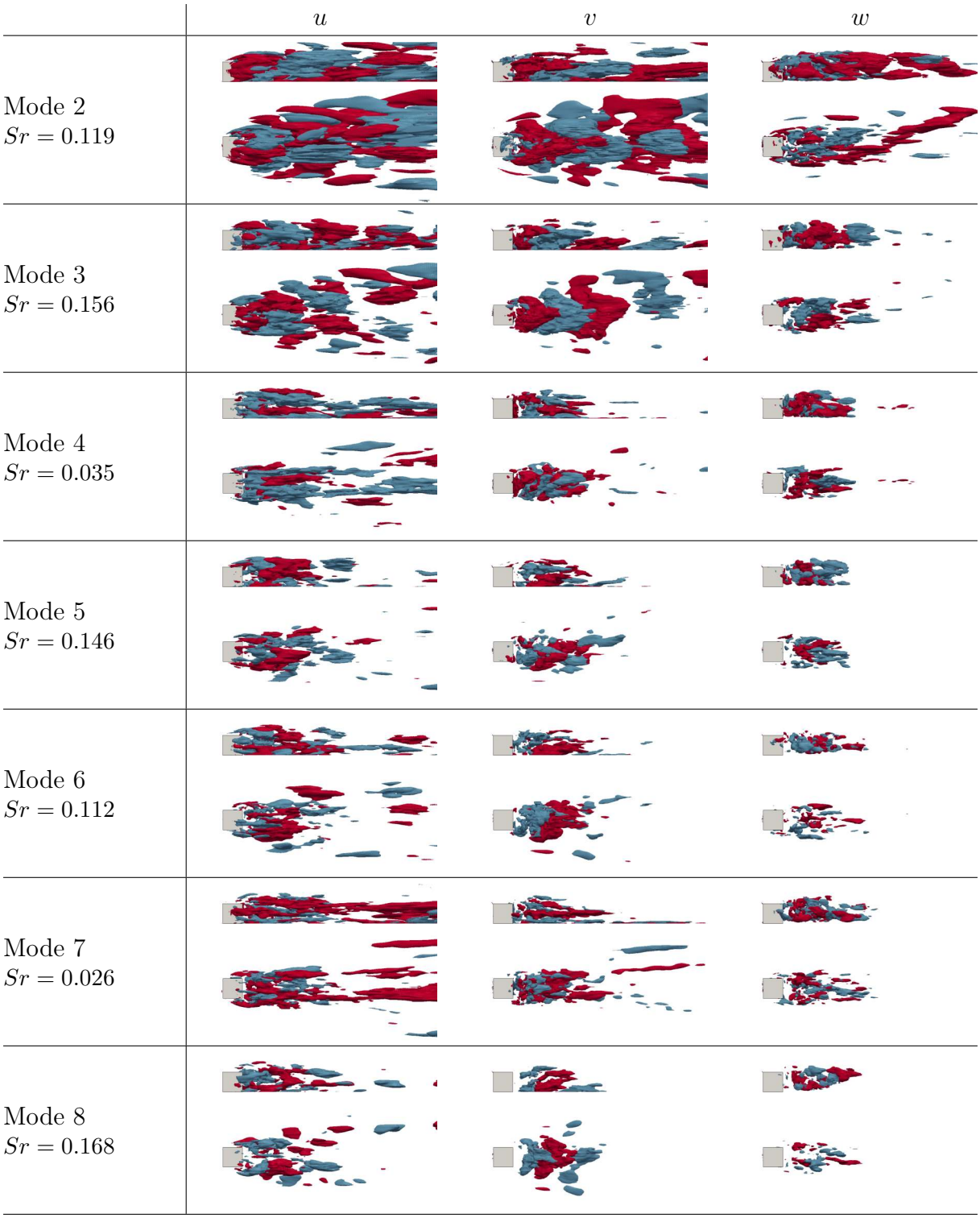

Figure 3.11: Isosurfaces of velocity components u, v and w of DMD modes 2−8. Isovalues normalized by bulk velocity U_∞. Red: +0.08, blue: −0.08. Upper pictures in row: side view, lower pictures in row: top view.

trating vortex shedding processes with the same frequency. Mode 6 can be interpreted as a vortex shedding process mainly from the side walls. The Strouhal number of $Sr = 0.112$ is nearly the same as the Strouhal number of mode 2 with $Sr = 0.119$. Mode 7 is, as mode 4, a low frequency oscillation. It is similar to mode 4 and has similarities to POD mode 4 and POD mode 7. Mode 8 is a shedding process. The typical positive-negative pattern is clearly visible in the v velocity component but not as pronounced in the other velocity components. The shedding process appears to induce a spanwise oscillating behavior of the wake.

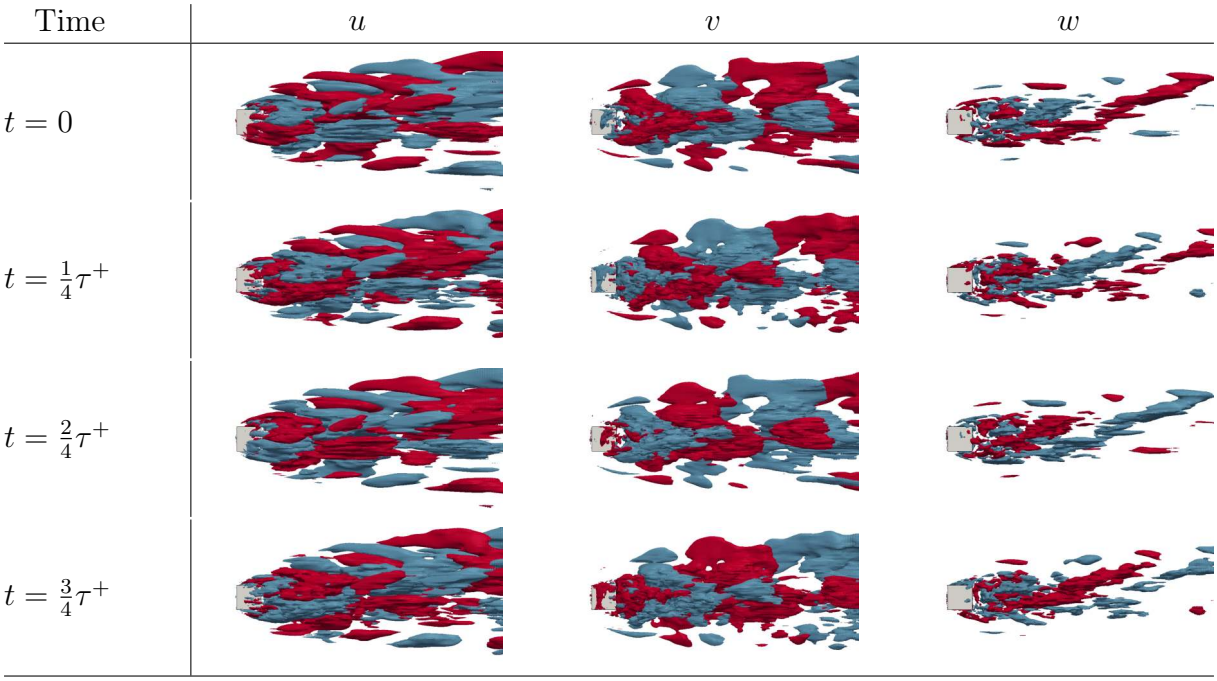

Figure 3.12: Reconstruction of one period $\tau^+ = Sr^{-1} = 8.40$ of DMD mode 2. Isosurfaces of velocity components u, v and w. Isovalues normalized by bulk velocity U_∞. Red: $+0.08$, blue: -0.08.

A lower dimensional representation of the flow has been reconstructed with one mode for the first three oscillating modes 2 to 4. The reconstruction of mode 2 is shown in Fig. 3.12 for one period of the oscillation. In the reconstruction, it can be seen, how the fluctuations deform and how they are convected with the main flow. Concentrating on the u velocity component, at $t = 0$ a positive (red) structure forms at one side of the cube and is convected down stream at $t = \frac{1}{4}\tau^+$. After half a period at $t = \frac{1}{2}\tau^+$, a negative structure (blue) forms at the same place. At the same time at $t = 0$, the positive structure in the v component shows how the flow is deflected in the spanwise direction by the detaching vortex. An interesting fact of this reconstruction is that the w velocity component is negative for the shedding of one side of the cube and positive for the shedding from the other side. This means that the axis of the vortices detaching from one side tilts inwards, while the axis of the vortices from the other side tilts outwards while they are convected down stream.

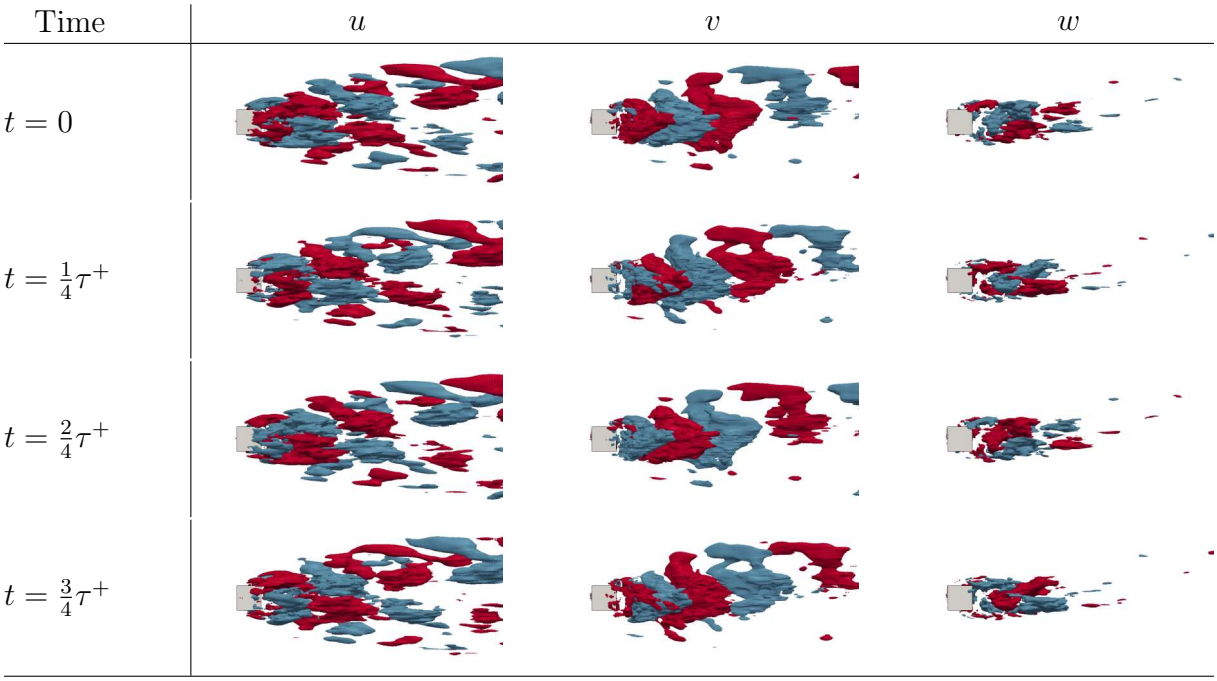

Figure 3.13: Reconstruction of one period $\tau^+ = Sr^{-1} = 6.41$ of DMD mode 3. Isosurfaces of velocity components u, v and w. Isovalues normalized by bulk velocity U_∞. Red: $+0.08$, blue: -0.08.

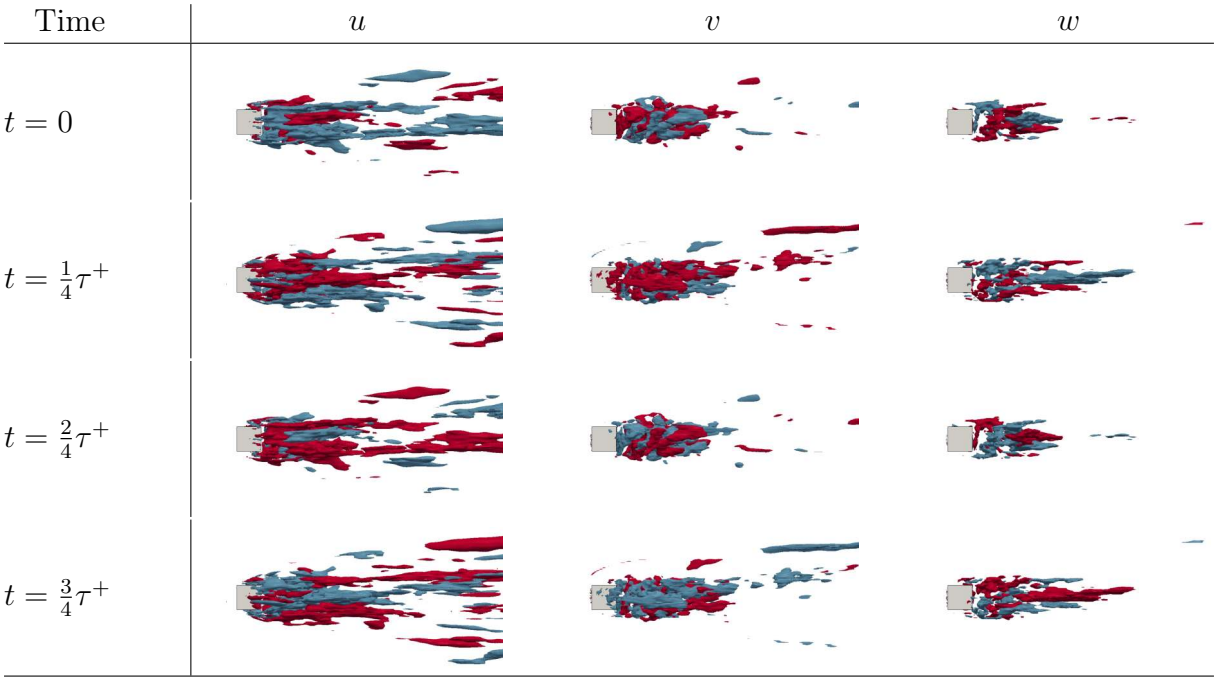

Figure 3.14: Reconstruction of one period $\tau^+ = Sr^{-1} = 28.57$ of DMD mode 4. Isosurfaces of velocity components u, v and w. Isovalues normalized by bulk velocity U_∞. Red: $+0.08$, blue: -0.08.

The reconstruction of mode 3 shows that mode 2 and 3 are, except for the Strouhal number and length scales, very similar. The upward and downward motion of mode 3 is the same as of mode 2. With upward motion for vortices detaching from the y-positive side and downward motion for vortices from the y-negative side of the cube.

In the reconstruction of mode 4, the oscillating motion of the longitudinal structures directly behind the cube is quasi stationary. The structures change from positive to negative motion without being convected with the main flow. The flow structures towards the sides of the domain move with the main flow. These tube like structures describe the motion of the unsteady vortices that form the "legs" of the horse shoe vortices of the time averaged flow.

The Dynamic Mode Decomposition was able to separate the dominant dynamic processes in the flow around the surface mounted cube. The additional information of growth rate and frequency of the modes facilitate the interpretation of the underlying flow mechanism and allow to link the modes to distinct flow phenomena. For the first DMD modes, strong visual similarities to the POD modes could be identified. As the structures of one DMD mode share a common frequency and describe a part of the dynamics of the flow, each mode can be reconstructed and interpreted individually. This is an advantage over the POD, were the modes describe a part of the variance of the flow rather than a part of the dynamic behavior.

Dynamic Mode Decomposition on the Fields of the Tensor Magnitudes of the Shear Maximizing Decomposition In addition to the approach of analyzing the velocity vector field, derived quantities can also be analyzed with the DMD. While a DMD analysis of the velocity vector field isolates the dominant fluctuations in the flow, it cannot distinguish between different kinds of relative motion like rotational or shearing motions. These relative motions are Galilean invariant and are therefore better suited to the identification of coherent structures in the flow. The DMD is executed on the scalar fields of the magnitudes of the Shear Maximizing Decomposition tensors $||(\nabla U)_{SH}||$, $||(\nabla U)_{EL}||$ and $||(\nabla U)_{RR}||$ with $N_{DMD} = 800$ time steps, a time step length of $\Delta t_{DMD}\frac{U_\infty}{H} = 0.1$ and a total time span of $T_{DMD}\frac{U_\infty}{H} = 80$. The time step data is filtered with a 4th order low-pass filter with a ratio of cut-off frequency to Nyquist frequency of 0.1. After the singular value decomposition in the DMD algorithm, the projection basis is restricted to modes with a relative contribution of more than $1 \times 10^{-4}\,\%$ to the total variance of the flow.

The spatially weighted relative amplitudes of the fields are shown in Fig. 3.15 and 3.16. The amplitudes in Fig. 3.15 are normalized by the amplitude of the first mode of $||(\nabla U)_{SH}||$ while the amplitudes in Fig. 3.16 are normalized by the amplitude of the first mode of the field itself. Shear is clearly the most intense relative motion in the flow while the amplitudes of rigid body rotation and elongation have the same magnitude. The hierarchy

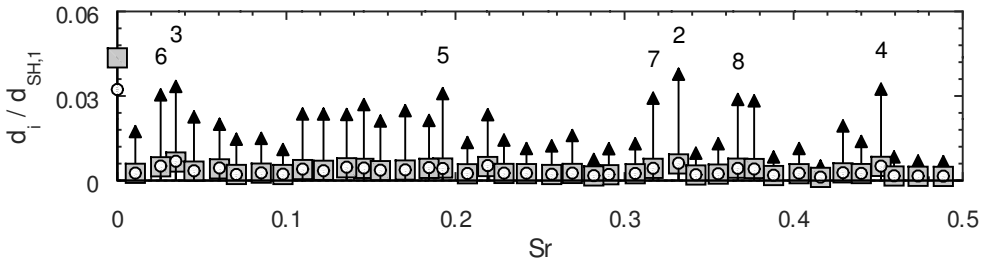

Figure 3.15: Relative amplitude over Strouhal number. Spatially weighted amplitudes of the dynamic modes normalized by amplitude of the first mode of $||(\nabla U)_{SH}||$. Triangles: $||(\nabla U)_{SH}||$, squares: $||(\nabla U)_{EL}||$, circles: $||(\nabla U)_{RR}||$.

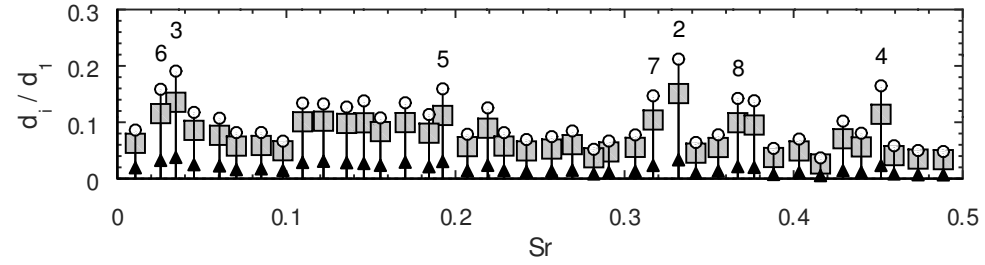

Figure 3.16: Relative amplitude over Strouhal number. Spatially weighted amplitudes of the dynamic modes normalized by amplitude of the first mode of the field. Triangles: $||(\nabla U)_{SH}||$, squares: $||(\nabla U)_{EL}||$, circles: $||(\nabla U)_{RR}||$.

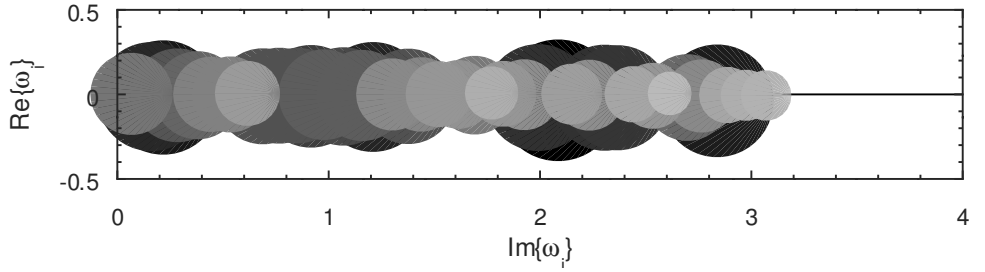

Figure 3.17: Eigenvalues of the Dynamic Modes transformed into the complex stability plane. Size and darkness of the symbols indicate the amplitude of the modes of $||(\nabla U)_{SH}||$.

of modes is independent of the field, mode 2 of $||(\nabla U)_{SH}||$ is also mode 2 of $||(\nabla U)_{EL}||$ or $||(\nabla U)_{RR}||$. While the amplitudes of the DMD modes of the velocity vector field in the previous analysis decrease for modes with higher frequency, the amplitudes of the DMD modes of the SMD tensor magnitudes are more independent of frequency and high frequency modes with high amplitudes can be found. In the singular value decomposition step of the DMD algorithm, the information of high amplitude modes is distributed over the lower POD modes of high variance. The conventional DMD algorithm, with filtering the data by restricting the projection basis in the singular value decomposition and thereby discarding fluctuations with frequencies that cannot be resolved, would not work in this case. Here, the pre-processing with a low-pass filter is inevitable. The spectrum of Eigenvalues, shown in Fig. 3.17 is nearly undampened. Without pre-filtering the data, the analysis would be contaminated by noise and the spectrum would be artificially dampened.

Isosurfaces of the dynamic modes 2 to 8 are shown in Fig 3.18, isosurfaces of the dynamic modes 9 to 15 are shown in Fig. 3.19. The positive and negative values of the isosurfaces can be interpreted here as an oscillation around a mean value. In the field of rigid body rotation of mode 2, the increasing and decreasing of the rotation in the horse shoe vortices can be seen. The "legs" of two vortices rotate around each other while they bend around the cube. The patterns in the wake flow of the cube indicate a vortex shedding. The shedding starts before the trailing edges around the cube but not at the same time on all sides. The horse shoe vortices and the shedding process can also be seen in the field of elongation of mode 2. For the shear field, the values in the boundary layers at the bottom and top wall of the domain have been clipped for better visibility. The vortex shedding is also visible in the shear field of mode 2. Mode 3 shows the same low frequency oscillation, previously found in mode 4 of the DMD analysis of the velocity field. The frequencies are the same and the structures have the same longitudinal shape as the structures found in mode 4 of the DMD analysis of the velocity field. Here, it can be seen that the low frequency oscillation also affects the horse shoe vortices in front of the cube. Mode 4 has relatively high Strouhal number and low length scale. The fluctuations start relatively regular at the leading edge and are convected with the main flow. The same is true for Mode 5 but with lower Strouhal number and larger length scales. Mode 6 is a low frequency oscillation similar to mode 3 but with even lower Strouhal number. The modes 7 and 8 are, again, vortex shedding processes similar to the modes 4 and 5.

The dominant vortex shedding processes, found in the DMD on the velocity field, with alternating shedding from the side walls of the cube and a Strouhal number of around $Sr = 0.12$ could not be found in the first 8 modes of this analysis. This is due to different meaning of the amplitude of the modes of a velocity field and the modes of a field of relative velocity. In the DMD analysis of the magnitudes of the SMD tensors, the first modes with alternating shedding from the side walls of the cube are mode 12 ($Sr = 0.110$) and 13 ($Sr = 0.122$) (Fig. 3.19). For all modes investigated, the field of rigid body rotation

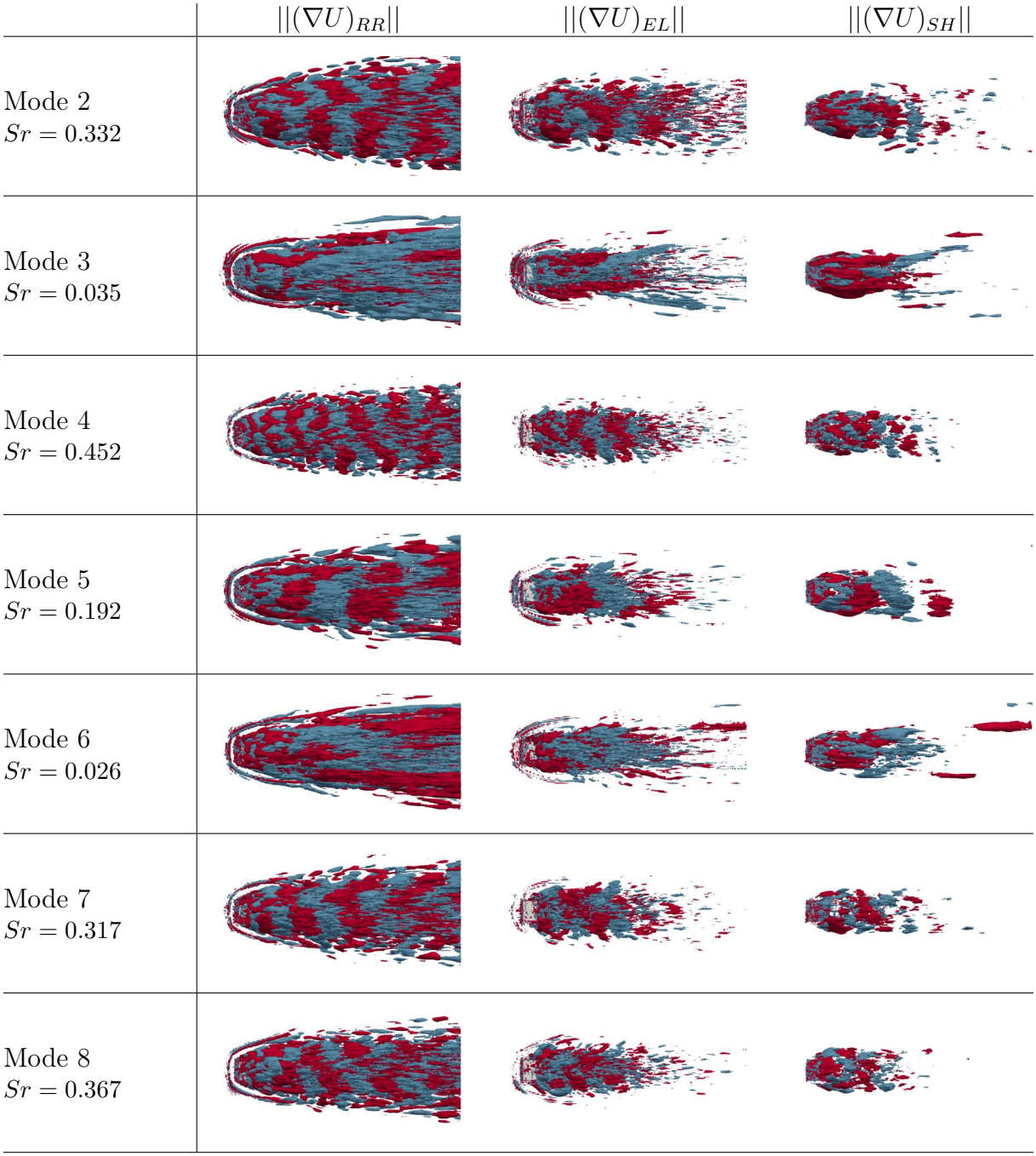

Figure 3.18: Isosurfaces of magnitudes of the Shear Maximizing Decomposition tensor. DMD modes $2-8$. Isovalues $||(\nabla U)_{RR}|| \frac{H}{U_\infty}$ red: $+0.03$, blue: -0.03. $||(\nabla U)_{EL}|| \frac{H}{U_\infty}$ red: $+0.075$, blue: -0.075. $||(\nabla U)_{SH}|| \frac{H}{U_\infty}$ red: $+0.25$, blue: -0.25.

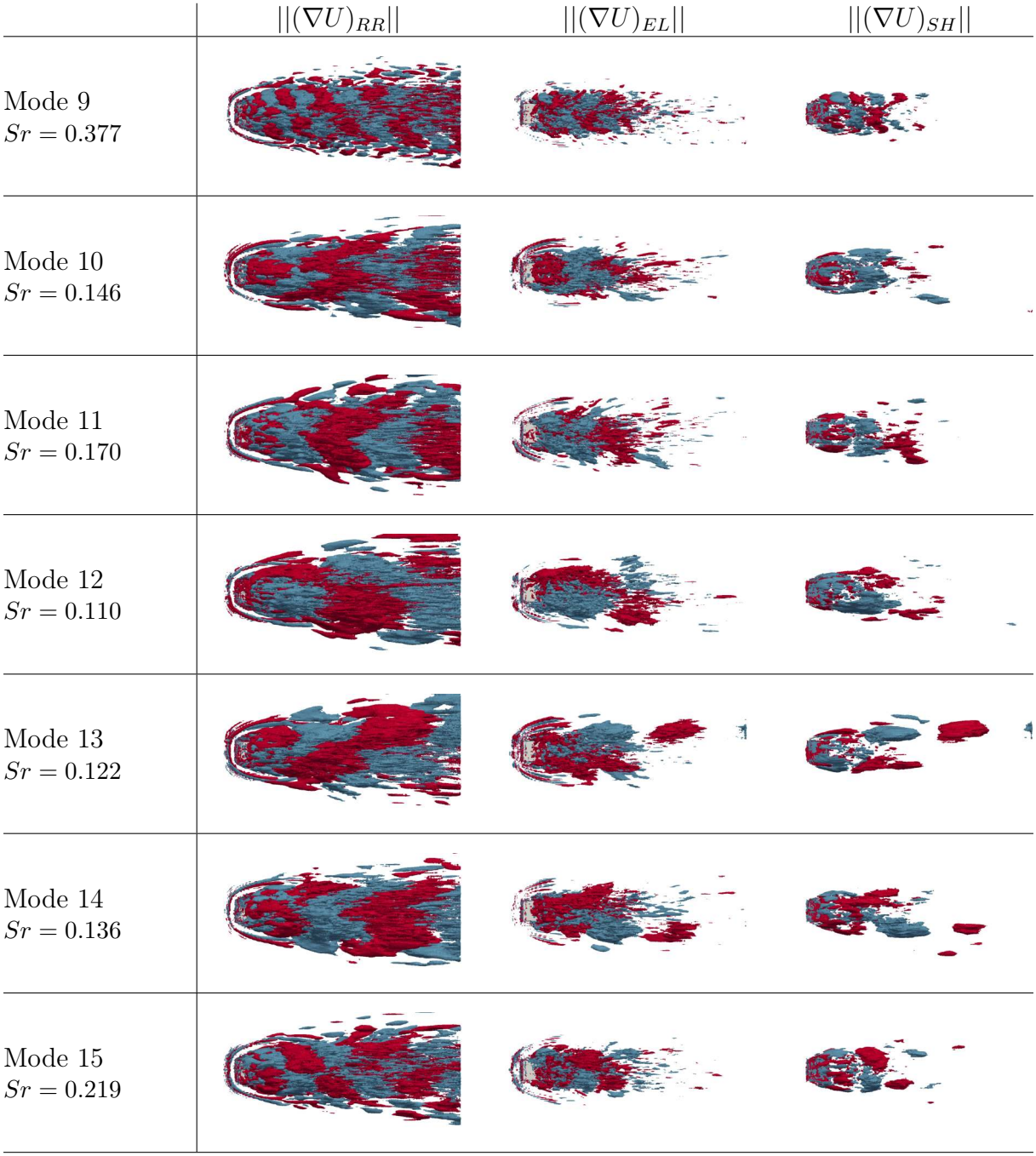

Figure 3.19: Isosurfaces of magnitudes of the Shear Maximizing Decomposition tensors. DMD modes $9 - 16$. Isovalues $||(\nabla U)_{RR}|| \frac{H}{U_\infty}$ red: $+0.03$, blue: -0.03. $||(\nabla U)_{EL}|| \frac{H}{U_\infty}$ red: $+0.075$, blue: -0.075. $||(\nabla U)_{SH}|| \frac{H}{U_\infty}$ red: $+0.25$, blue: -0.25.

shows a contribution of the horse shoe vortices to the oscillation in the mode. This is an indication that there exists an upstream influence of the wake flow on the oscillation of the horse shoe vortices.

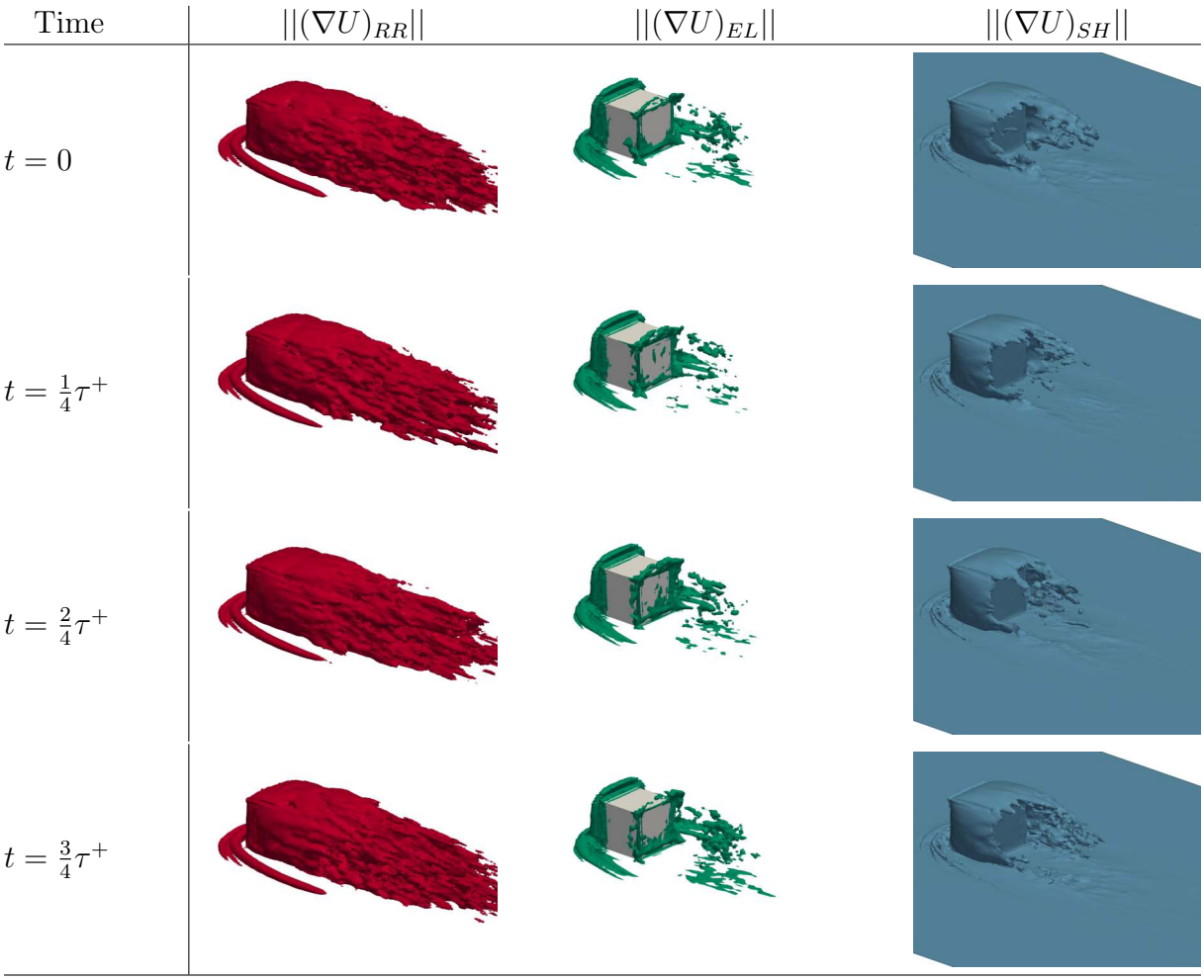

Figure 3.20: Reconstruction of one period $\tau^+ = Sr^{-1} = 28.57$ of DMD modes 1 and 3. Isosurfaces of the magnitudes of $||(\nabla U)_{RR}|| \frac{H}{U_\infty} = 0.6$, $||(\nabla U)_{EL}|| \frac{H}{U_\infty} = 1.5$ and $||(\nabla U)_{SH}|| \frac{H}{U_\infty} = 5.0$.

A reconstruction of the mean flow and one period of mode 3 is shown in Fig. 3.20. The isovalues are the same as in Fig. 3.6. The shear field of the reconstruction shows a streamwise oscillation of the main shear layer. The oscillation is present in the whole shear layer but most pronounced at the y-positive side of the cube. The oscillation in the field of elongation is restricted to the elongation at the trailing edges of the cube and to the wake. The elongation at the leading edges does not oscillate. Fluctuations can be found in most parts of the field of rigid body rotation but no clear motion of vortices can be seen except for a slight change in the length of the horse shoe vortices. The lack of a clear motion in the field of rigid body rotation is another indication that mode 3 is not

connected to the motion of vortices but is a low frequency oscillation of the whole wake of the flow.

3.1.3 Conclusion

The flow around a cube mounted in a channel was investigated in this test case. Statistical quantities of the mean flow, as well as steady and unsteady flow structures were compared to numerical and experimental investigations found in the literature. The DDES simulation is in good agreement with published experimental data and is found to produce competitive results when compared to published LES simulations. The time averaged flow was studied by Line Integral Convolution (LIC) pictures of the wall shear stress and the velocity vector field. The LIC pictures were found to be well suited to investigate the flow structures relative to one reference frame. A Shear Maximizing Decomposition was employed as a Galilean invariant method to investigate the flow structures and was found to describe the dominant flow structures also described in the literature.

The unsteady flow around the cube was studied using a sign corrected Proper Orthogonal Decomposition (POD) of the velocity vector field, a Dynamic Mode Decomposition (DMD) of the velocity vector field and a Dynamic Mode Decomposition of the fields of the tensor magnitudes of the Shear Maximizing Decomposition (SMD). The POD analysis of the velocity field was found to be able to extract the most dominant flow structures in the flow. The dominant structures were found to be in good agreement with published POD investigations with the same geometry. For higher order modes, the relation of the POD modes to distinct flow phenomena like vortex shedding processes could not be established. As the POD typically reproduces one flow phenomena with more than one mode, a reconstruction of distinct phenomena is usually not possible. The DMD of the velocity field was able to extract the dominant flow processes. The most dominant dynamic modes were found to show strong visual similarities to the most dominant proper orthogonal modes. Individual dynamic modes were reconstructed and were found to contain distinct flow phenomena like the dominant vortex shedding from the cube or an oscillation of the horse shoe vortices. The amplitude spectra of the Dynamic Mode Decomposition of the SMD tensor magnitudes are considerably different from the DMD of the velocity field. This is explained by the fact that fluctuations of high kinetic energy, the dominant modes of the DMD of the velocity field, do not necessarily imply strong relative motions. While the high frequency modes of the velocity field have low energy content, this is not the case for the relative motions. This is an important finding for the application of the method as the singular value filter of the DMD assumes low total variance in high frequency modes. The application of the DMD to the SMD tensor data wound not have been possible without low-pass filtering the data prior to the DMD analysis.

3.2 SAE Car Model

The SAE Car Model is a highly simplified, generic car model. It was used in the past to investigate fundamental flow phenomena around car-like shaped bluff bodies. The car body was proposed by Cogotti in [19] with different rear end shapes and was modified by other authors for specific investigations. The model is used here to investigate the effect of a change in geometry on the results of the Dynamic Mode Decomposition. The DMD is applied to velocity vector fields and the scalar field of pressure in one analysis. This approach allows for the investigation of the unsteady interdependencies of flow variables.

3.2.1 Setup

The SAE car model is investigated in four different configurations. Two closed configurations as proposed by Cogotti in [19] and two configurations with a generic engine compartment as proposed by Bäder in [7].

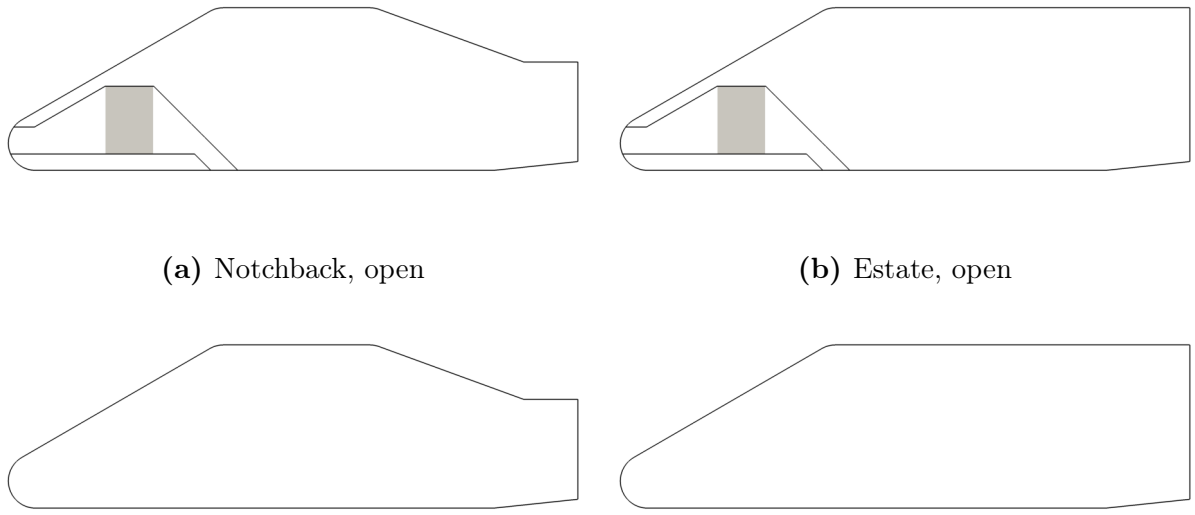

(a) Notchback, open

(b) Estate, open

(c) Notchback, closed

(d) Estate, closed

Figure 3.21: Cross sections of the SAE-Body configurations

Cross sections of the configurations are shown in Fig. 3.21. The generic engine compartment contains a model radiator (gray box in the pictures) which was modeled with flow straightener and screens in the experiments of Bäder and which is modeled with a porosity region in the simulations. The dimensions of the model radiator for a full-scale (1:1) model are $\Delta x = 360\,mm$, $\Delta y = 800\,mm$ and $\Delta z = 500\,mm$. The distance from the foremost point of the model to the radiator is $\Delta x = 716\,mm$, the distance from the

under body to the radiator is $\Delta z = 120\,mm$. The dimensions of the inlet openings are $\Delta y = 800\,mm$ and $\Delta z = 200\,mm$, the dimensions of the outlet openings are $\Delta x = 200\,mm$ and $\Delta y = 800\,mm$. The slant angle between channel and radiator, upstream the radiator, is 60°. The slant angle between channel and radiator, downstream the radiator, is 45°.

The positions of the legs are changed in the experiments of Bäder compared to the geometry description of Cogotti. In the simulations, the leg positions according to Bäder are used. The distance from the foremost point of the geometry to the center of the front legs is $\Delta x = 1520\,mm$. The distance between the front and rear legs, as well as between the left and right legs is $\Delta x = \Delta y = 1260\,mm$. In the experiments of Bäder, the model is mounted on a Table. For a full scale model, the dimensions of the table would be: $\Delta x = 10\,m$ and $\Delta y = 8\,m$. The distance from the leading edge of the table to the foremost point of the model would be: $\Delta x = 1.9\,m$.

The Reynolds number, based on the length of the car model, is $Re = 3.28 \cdot 10^6$.

Numerical Setup

The computational domain around the model vehicles is a rectangular box with the approximate dimensions of: $\Delta x = 18L$, $\Delta y = 15L$ and $\Delta z = 10L$. The domains consist of hex-dominant grids with approx. 60 million cells. The cell size in the vicinity of the car models and in the near wake is $\frac{\Delta x}{L} = 1.9 \cdot 10^{-3}$ ($\Delta x = 8.0\,mm$ in full scale). Prism layers are present at the model car geometries, the legs and the part of the ground that has a zero velocity boundary condition. The average dimensionless wall distance is approximately $y^+ \approx 50$, were the velocity boundary condition at the wall is zero. To account for y^+ values below the logarithmic part of the boundary layer, an adaptive wall model is used. The grids of the different configurations are nearly identical, except for the changes in the model car geometry.

For the discretization of convective terms, a blending approach between two schemes is used. The fist scheme is a second order central differencing scheme with a small amount of upwind. The second scheme is a first order upwind scheme. Depending on criteria for cell size, cell quality and the CFL number, the scheme blends from the second order central differencing scheme to the first order upwind scheme. This approach was used by Islam et al. in [44]. It allows for the use of a second order central differencing scheme in most of the computational domain, while it stabilizes the solution in a few low quality or small cells with high CFL number or in the big cells at the inlet, outlet and far field boundaries of the domain. As in the test case of the surface mounted cube (Section 3.1), the gradients are computed using the Gauss theorem were the surface values are interpolated with a second order linear interpolation. The diffusive terms are approximated using a stabilized over relaxed approach to account for the non-orthogonality of the mesh. The scheme to discretize the time derivatives is second order, implicit. The time step is adjusted to result

in a CFL number smaller than 1 around the car model and in most of the domain, while in a few cells the CFL number is allowed to reach a value not higher than 2.

The Spalart-Allmaras DDES turbulence model is used as described in section 2.2.2. To ensure that the shielding function of the turbulence model worked correctly, the wall normal eddy viscosity profiles have been checked against the velocity profile of the boundary layers.

The pressure loss of the model radiator is described by the Darcy-Forchheimer equation (Section 2.2.3, Eq. 2.38) with the Coefficients: $d = 5.0050e7\,m^{-2}$ and $f = 1.2065e2\,m^{-1}$.

The Dynamic Mode Decomposition analysis is executed in a subvolume of the computational domain shown in Fig 3.22. The size of the subvolume is $\Delta x = 1.6L$, $\Delta y = 0.55L$ and $\Delta z = 0.45L$ with the length of the car L. The distance from the foremost point of the car geometry to the foremost point of the subvolume is $\Delta x = 0.05L$.

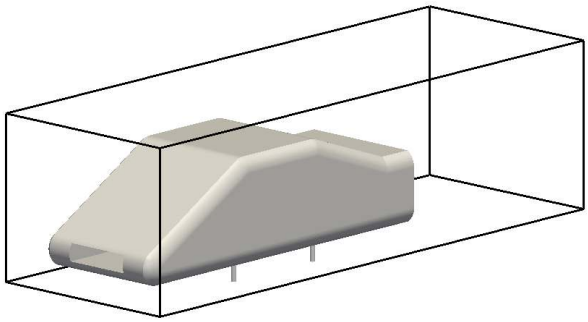

Figure 3.22: Subvolume of the DMD computation. Size of the subvolume: $\Delta x = 1.6L$, $\Delta y = 0.55L$, $\Delta z = 0.45L$.

Boundary Conditions The inlet to the domain is a stationary, Dirichlet type boundary condition for the velocity vector and a zero gradient Neumann condition for the pressure. The value for the modified eddy viscosity $\tilde{\nu}$ at the inlet is chosen such that the free stream eddy viscosity ratio $\frac{\tilde{\nu}_\infty}{\nu_\infty}$ has a value of 3 directly in front of the car model as recommended by Rumsey and Spalart in [90]. The outflow boundary condition of velocity is a modified zero gradient Neumann boundary condition that is modified to avoid backflow into the domain. The outlet boundary condition for the pressure is a Dirichlet boundary condition with a value of zero. The modified eddy viscosity $\tilde{\nu}$ at the outlet is treated with a zero gradient condition. The far field walls of the domain: the top wall, the floor – except for the table part – and the side walls are slip walls. The velocity components tangential to the walls are handled with a zero gradient Neumann condition, while the normal velocity components are set to zero. The modified eddy viscosity and pressure are handled here with zero gradient Neumann boundary conditions. The table is modeled in the simulations as a part of the floor with no-slip condition. At the surface of the car models, the legs and the table patch, the velocity vector and the modified eddy viscosity set to zero. The pressure is treated with a zero gradient boundary condition.

3.2.2 Results

Time averaged flow

The drag coefficients computed from the simulations and the drag coefficients published in Bäder [7] are shown in Tab. 3.1. The drag coefficients are given for the car models, including the legs.

Table 3.1: Drag coefficient c_D of the simulations and of experiments from Bäder [7]

	Notchback, closed	Notchback, open	Estate, closed	Estate, open
Simulations	0.205	0.228	0.269	0.295
Experiments [7]	0.196	0.240	0.256	0.285

For the closed notchback geometry, the drag coefficient of the simulation is 9 counts (thousandths) higher than the experimental value. The drag coefficient of the simulation of the open notchback is 12 counts lower. The drag coefficient of the simulation of the closed estate geometry is 13 counts higher than the experimental value and the drag coefficient of the simulation of the open estate geometry is 10 counts higher than the experimental value.

The difference between the open and closed models – the cooling drag coefficients – are in the experiments $\Delta c_{D,Notchback} = 0.044$ and $\Delta c_{D,Estate} = 0.029$. The cooling drag coefficients of the simulations are $\Delta c_{D,Notchback} = 0.023$ and $\Delta c_{D,Estate} = 0.026$. While the simulated drag coefficients of the closed notchback, as well as the open and closed estate configurations are approx. 10 counts higher in the simulations, the drag coefficient of the open notchback configuration is 12 counts lower. The cooling drag coefficient of the estate configurations is matched with a difference of 3 counts, the cooling drag coefficient of the notchback configurations differ by 21 counts.

As three of the four configurations show a nearly constant off-set to the measured values and the simulation setup has been used unchanged for the four configurations, an incorrect measurement of the drag coefficient of the open notchback configurations is assumed. This assumption is supported by the fact that an independent series of measurements of the same configurations with additional wheels, found in [7], does not show the large difference between the cooling drag coefficients of notchback and estate configurations. The nearly constant off-set of the other simulations is assumed to be due to wind tunnel effects that are not included in the simulations.

Figure 3.23 shows Line Integral Convolution (LIC) pictures of wall shear stress for the open SAE car body configurations with the notchback configuration in the left and the

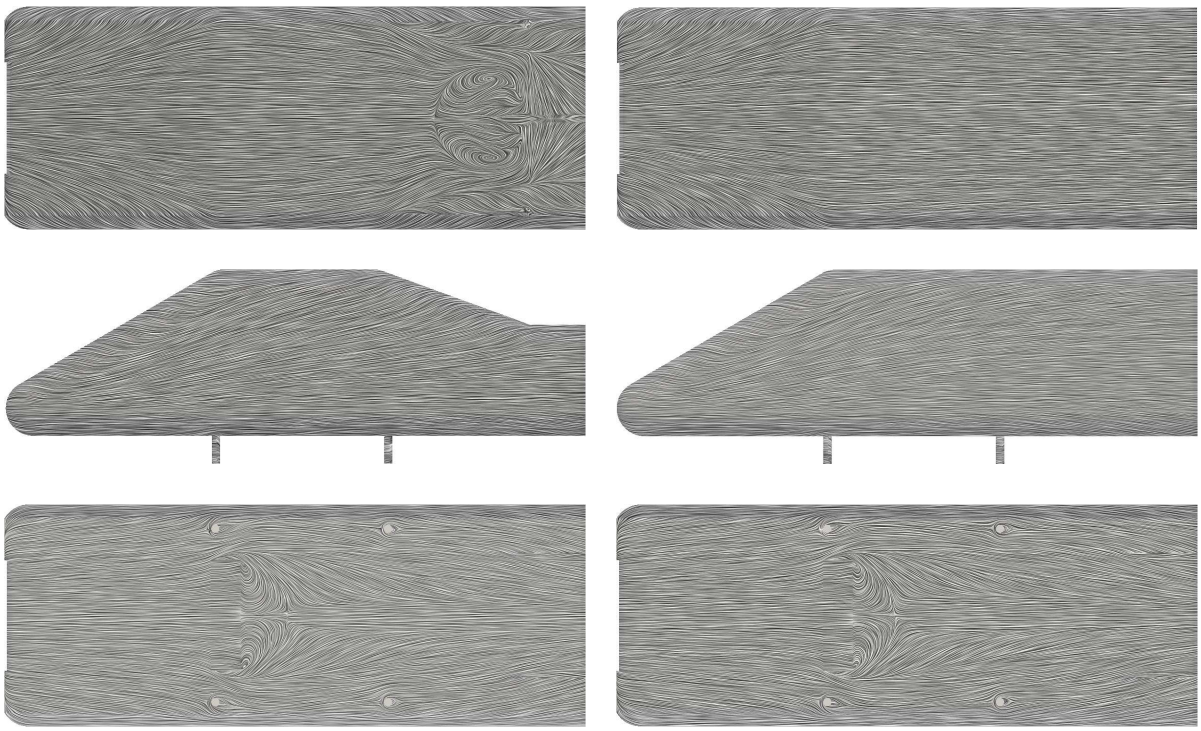

(a) Notchback, open **(b)** Estate, open

Figure 3.23: Line Integral Convolution (LIC) of the wall shear stress on the open SAE car bodies. Left column: Notchback configuration. Right column: Estate configuration.

estate configuration in the right column. All pictures show a very similar LIC pattern in the front part of the car body. In the top view of the notchback car body, the separation and reattachment lines of the longitudinal C-pillar vortices are clearly visible. On the rear slant, between the LIC pattern of the C-pillar vortices, the spiraling pattern of two detaching vortices is present. These vortices rotate against the direction of the C-pillar vortices. Between these vortices another pair of vortices is present which detaches at the end of the rear slant and rotates in the direction of the C-pillar vortices. The LIC pattern in the center line of the rear slant indicates a small recirculation zone between the vortex systems. The LIC pattern of the top view of the estate configuration does not show detachment lines. Here, the flow detaches at the sharp edge at the rear end of the geometry.

In the side views of the model geometries, no detachment lines or reattachment lines are visible as well. No distinct A-pillar vortices are induces by the SAE car body geometries at the operating conditions of the test cases.

The bottom view of the models show the LIC patterns of the flow around the legs and the detachment and reattachment of the flow leaving the generic engine compartment. Two circular LIC patterns are visible at the outlet openings of the generic engine compartments, indicating the detachment of two longitudinal vortices. The underbody flow of the two

models is very similar. It can be noticed that the detached flow from the generic engine compartment reattaches slightly earlier in the estate configuration.

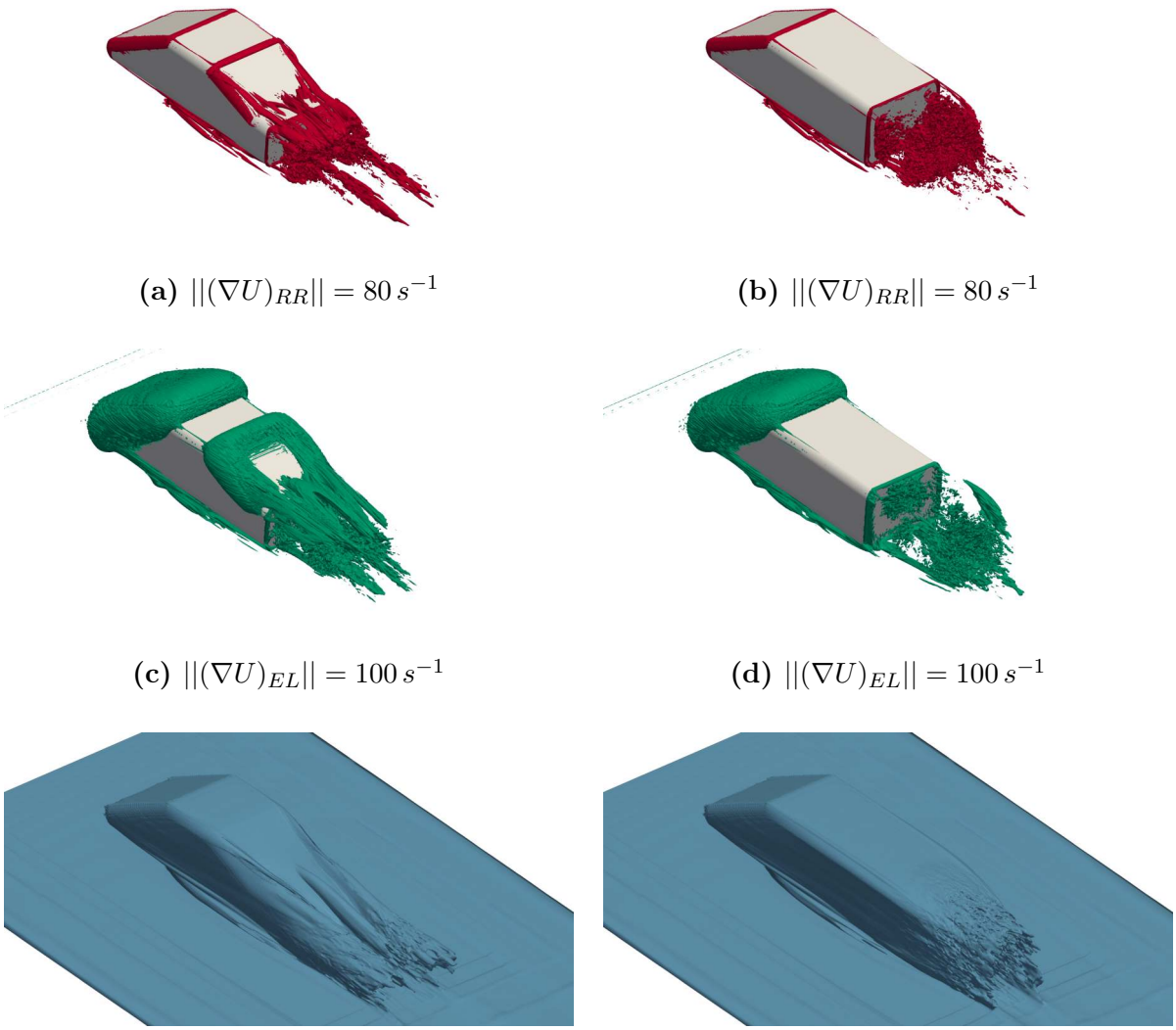

(a) $||(\nabla U)_{RR}|| = 80\,s^{-1}$ **(b)** $||(\nabla U)_{RR}|| = 80\,s^{-1}$

(c) $||(\nabla U)_{EL}|| = 100\,s^{-1}$ **(d)** $||(\nabla U)_{EL}|| = 100\,s^{-1}$

(e) $||(\nabla U)_{SH}|| = 200\,s^{-1}$ **(f)** $||(\nabla U)_{RR}|| = 200\,s^{-1}$

Figure 3.24: Isosurfaces of the magnitudes of the SMD tensors. Left column: Open Notchback configuration. Right column: Open Estate configuration.

Magnitudes of the Shear Maximizing Decomposition (SMD) tensors for the two open configurations are shown in Fig 3.24. The isosurface of rigid body rotation $||(\nabla U)_{RR}||$ of the open notchback configuration is shown in the first picture of the first column. Visible is the bended flow around the curves of the geometry, the vortices from the legs, the vortex system on the rear slant and the near wake vortices. The vortex system on the rear slant consists, as already found from the LIC pattern, of the C-pillar vortices, two counter rotating vortices, two co-rotating vortices and a recirculation zone. Here, it can be seen that the first pair of counter rotating vortices split in two vortices after detaching from the surface. Additional vortices can be found with their origin in the small

recirculation area in the center line of the rear slant. In the near wake of the car body, two recirculation zones are present. From the recirculation zones, two longitudinal vortices are formed. While the isosurfaces describing the vortices from the rear slant are distinct tubes, the isosurfaces in the wake show a large number of smaller vortices penetrating the larger vortices. The superposition of these vortices results in the irregular appearance of the isosurfaces in the wake. The isosurface of rigid body rotation $||(\nabla U)_{RR}||$ of the open estate configuration is shown in the first picture of the right column. Here, the bended flow around the curves of the geometry and the vortex systems from the legs of the model are visible, similar to the notchback configuration. In the wake of the estate model, a larger recirculation zone is present.

Isosurface of the magnitude of the elongation tensor $||(\nabla U)_{EL}||$ are shown in the second row of Fig 3.24. Again, the front parts of the geometries produce similar isosurfaces. The rear slant of the notchback geometry produces an additional contribution to the irrotational, elongational part of the relative motion in the flow.

In the shear part of the relative motion $||(\nabla U)_{SH}||$, the shear layer of the table is visible. At the notchback geometry, the shear around the C-pillar vortices, around the two large longitudinal vortices in the wake and around the small recirculation zone in the center line of the rear slant can be seen. At the estate geometry, the main shear layer separates at the rear edge and extends around the recirculation zone into the wake with only slight contraction.

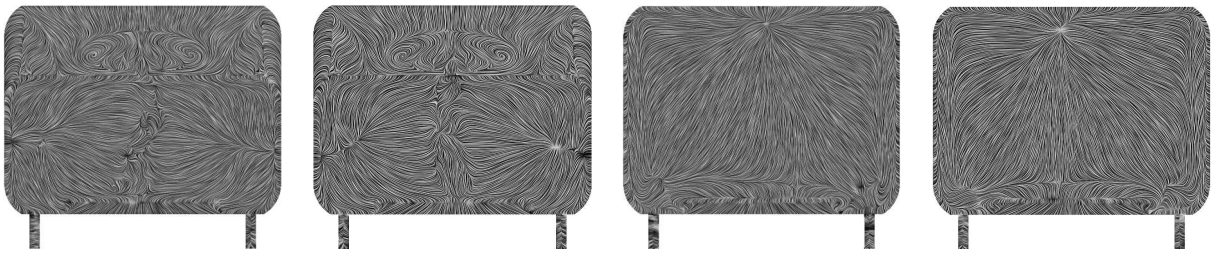

(a) Notchback, closed **(b)** Notchback, open **(c)** Estate, closed **(d)** Estate, open

Figure 3.25: Line Integral Convolution (LIC) of the wall shear stress on the open and closed SAE car bodies. Back view.

The LIC pattern of the wall shear stress on the back side of the geometries for all four configurations are shown in Fig 3.25. No big differences can be found between the open and closed geometries. At the closed notchback configuration, the centers of the detaching vortices are shifted towards the sides of the model when compared to the open configuration. The recirculation zone in the wake of the closed estate configuration is slightly smaller than the recirculation zone of the open estate configuration.

Unsteady Flow

The unsteady flow around the four configurations of the SAE car model is investigated with a Dynamic Mode Decomposition of the pressure and velocity field. A detailed examination is done for the dominant mode of the open notchback and open estate configurations.

Dynamic Mode Decomposition of Pressure and Velocity fields To find interdependencies between the flow variables, the DMD can be executed with fields of different physical quantities in one analysis. Here, the DMD is executed on the pressure scalar field and on the velocity vector field. While some quantities have a natural relative scaling, like the magnitudes of the SMD tensors in the previous test case on a surface mounted cube, pressure and velocity fields have different dimension and therefore no natural relative scaling. Here, the fields have to be scaled to unit variance prior to the analysis. Without the relative scaling, the restriction of the POD basis in the DMD algorithm would discard mainly fluctuations from the low variance field.

The DMD is executed in the same subvolume of the domain (Fig. 3.22) for all four configurations. The spectrum of amplitudes are shown in Fig. 3.26. The amplitudes are normalized by the amplitude of the mean mode. The order of the absolute values of the amplitudes of the mean modes is:

$$d_{1,Notchback,closed} < d_{1,Estate,closed} < d_{1,Notchback,open} < d_{1,Estate,open}$$

The increase of the mean mode amplitude of the open configurations over the closed configurations is explained by the increase of the total volume of the flow field in the open configurations. The increase in the mean mode of the estate configurations over the notchback configurations is due to a less uniform velocity distribution in the flow around the estate configurations. This effect is stronger than the gain in flow volume of the notchback configurations over the estate configurations. The relative amplitudes of the second modes in Fig. 3.26 are higher for the estate configuration. The fluctuations of mode 2 take a bigger volume due to the lack of downwash and the bigger size of the geometries at the rear end of the estate configurations.

Despite the fact that the amplitudes of different configurations cannot be compared directly, a dominant mode of approx. $f^* \approx 2\,Hz$ can be found for all four configurations. One period of this mode is reconstructed in Fig. 3.27, 3.28, 3.29 and 3.30 for the open notchback configuration and in Fig. 3.31, 3.32, 3.33 and 3.34 for the open estate configuration.

The reconstruction of one period of the pressure field of mode 2 of the open notchback configuration is shown in Fig. 3.27. A clear vortex shedding process can be seen. The

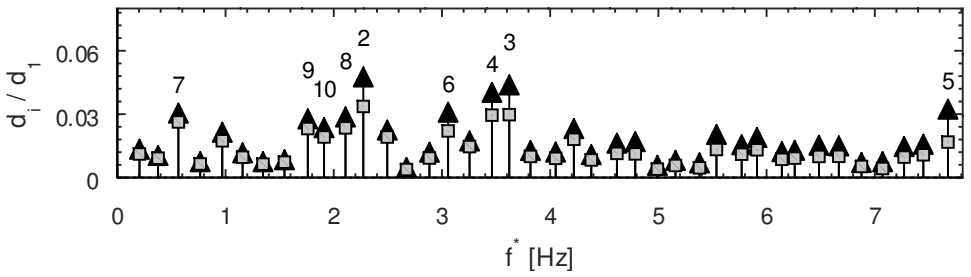

(a) Notchback, open

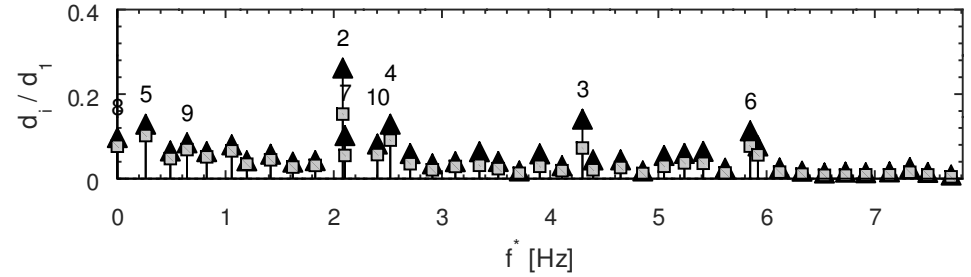

(b) Estate, open

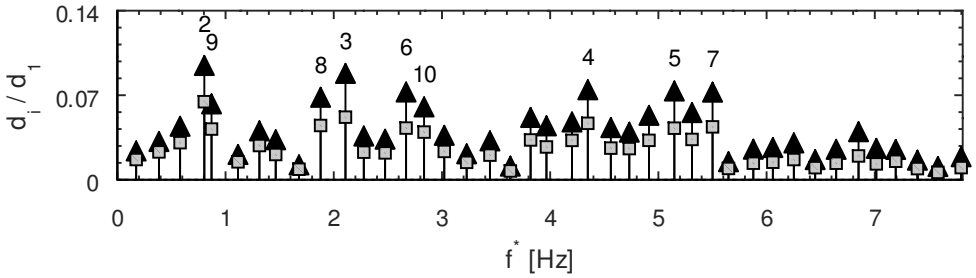

(c) Notchback, closed

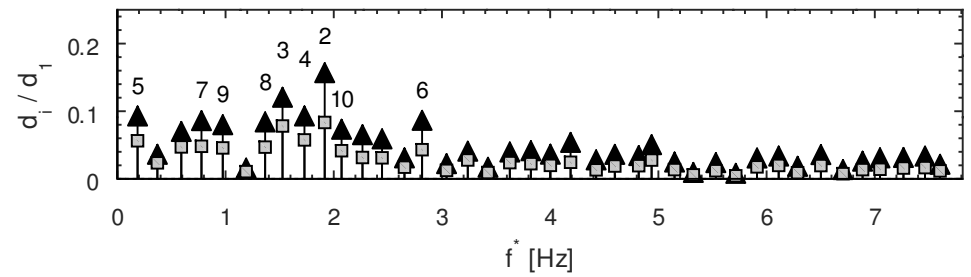

(d) Estate, closed

Figure 3.26: Relative amplitude over full scale frequency. Spatially weighted amplitudes of the dynamic modes normalized by amplitude of the first mode. Mode numbers by decreasing amplitude. Triangles: pressure, squares: velocity.

ring shape of the vortices is most clearly visible in the side view of the car geometry. The vortices form in the near wake of the car, are convected downstream and dissipate in a streamwise elongated motion. Despite the low frequency oscillation of approx. $2\,Hz$, a clear shedding process from the relatively thin legs of the model can be found. Other contributions to the oscillations in the mode are from the center of the underbody, downstream the generic engine hood opening and on the trunk deck of the model geometry.

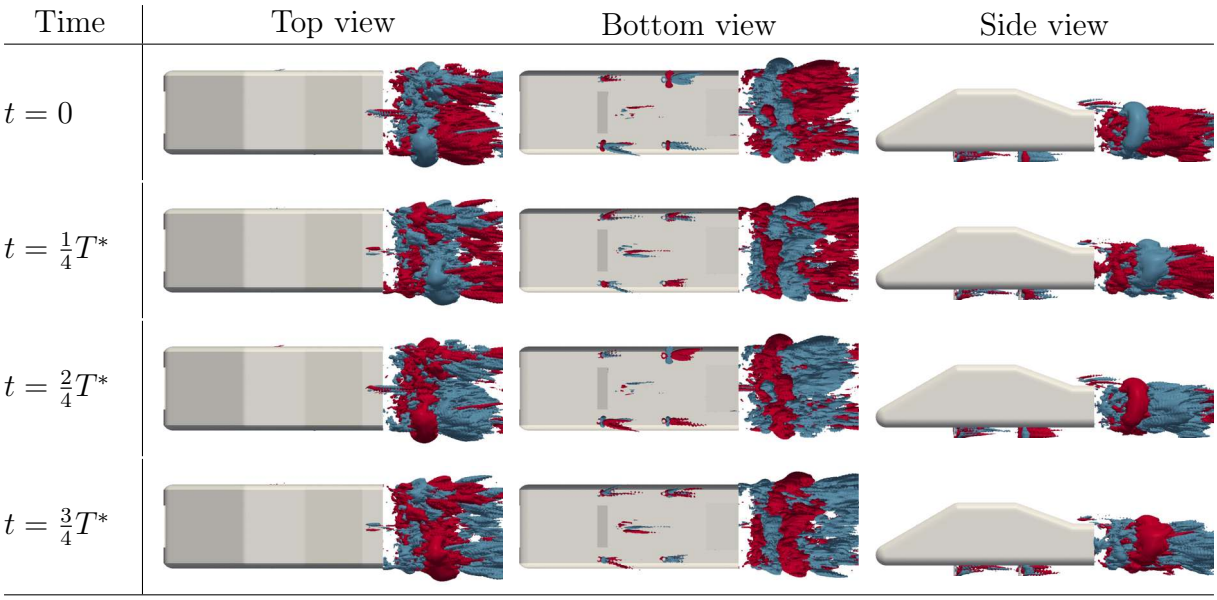

Figure 3.27: Open Notchback configuration. Reconstruction of one period $T^* = f^{*\,-1} = 0.44\,s$ of DMD mode 2. Isosurfaces of pressure. Red: $p = 5\,Pa$, blue: $w = -5\,Pa$.

The reconstruction of the u, v and w components of the velocity vector field of mode 2 are shown in Fig. 3.28, 3.29 and 3.30 respectively. The vortex shedding process, visible in the reconstruction of the pressure field in Fig. 3.27, can again be seen in the reconstruction of the velocity components. The ring shape of the vortices is most clearly visible in the streamwise velocity component. The fluctuations from the legs of the model, from the generic engine compartment opening and from the center line of the rear slant are more pronounced in the reconstructions of the velocity components. In contrast to the fluctuations found in the reconstruction of the pressure field, the fluctuations of the reconstructed velocity components are convected with the main flow into the wake of the model.

The reconstruction of one period of the pressure field of mode 2 of the open estate configuration is shown in Fig. 3.31. As in the flow around the notchback geometry, mode 2 of the estate geometry is also dominated by a large scale vortex shedding process in the wake of the model. While the vortices in the wake of the notchback geometry are convected downstream without much change in size, the vortices found in the wake of the estate geometry grow rapidly. In the top view and the bottom view of the reconstructions, the vortices are found to describe a spiraling path. This is due to a circular motion of the

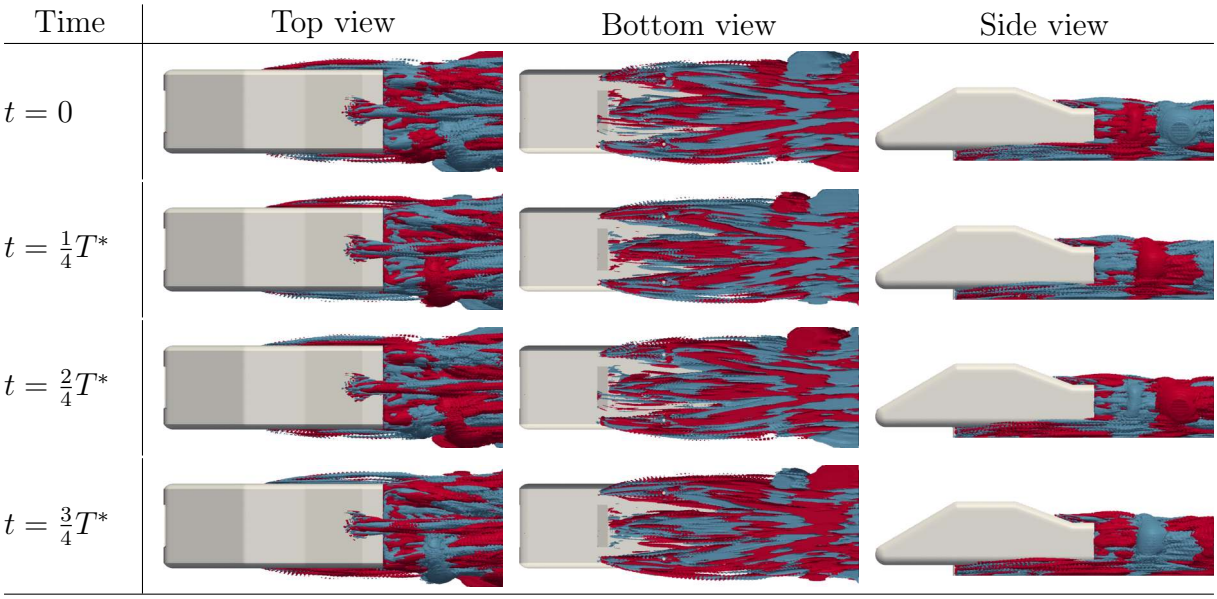

Figure 3.28: Open Notchback configuration. Reconstruction of one period $T^* = f^{*-1} = 0.44\,s$ of DMD mode 2. Isosurfaces of streamwise velocity component. Red: $u = 1.5\,m/s$, blue: $u = -1.5\,m/s$.

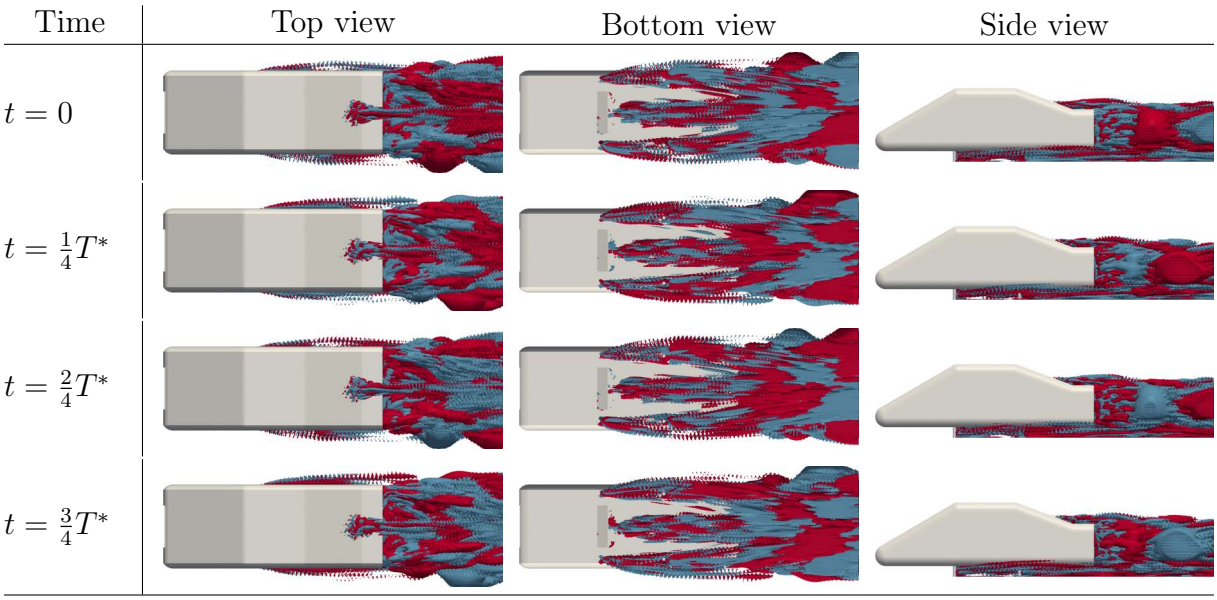

Figure 3.29: Open notchback configuration. Reconstruction of one period $T^* = f^{*-1} = 0.44\,s$ of DMD mode 2. Isosurfaces of sideward velocity component. Red: $v = 1.5\,m/s$, blue: $v = -1.5\,m/s$.

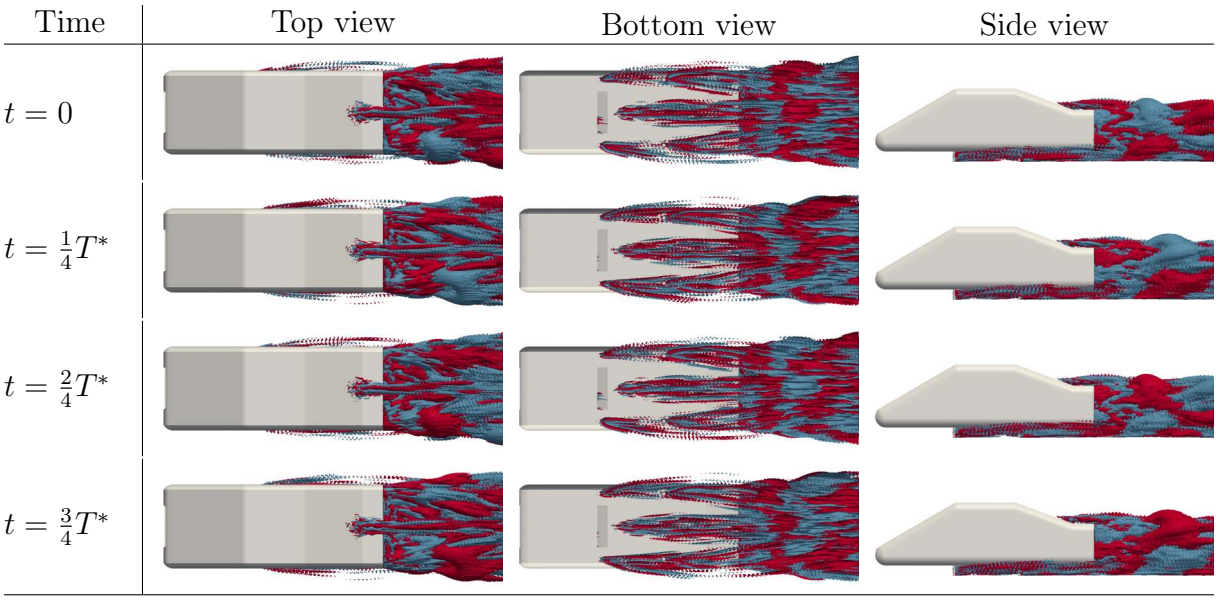

Figure 3.30: Open notchback configuration. Reconstruction of one period $T^* = f^{*-1} = 0.44\,s$ of DMD mode 2. Isosurfaces of upward velocity component. Red: $w = 1.5\,m/s$, blue: $w = -1.5\,m/s$.

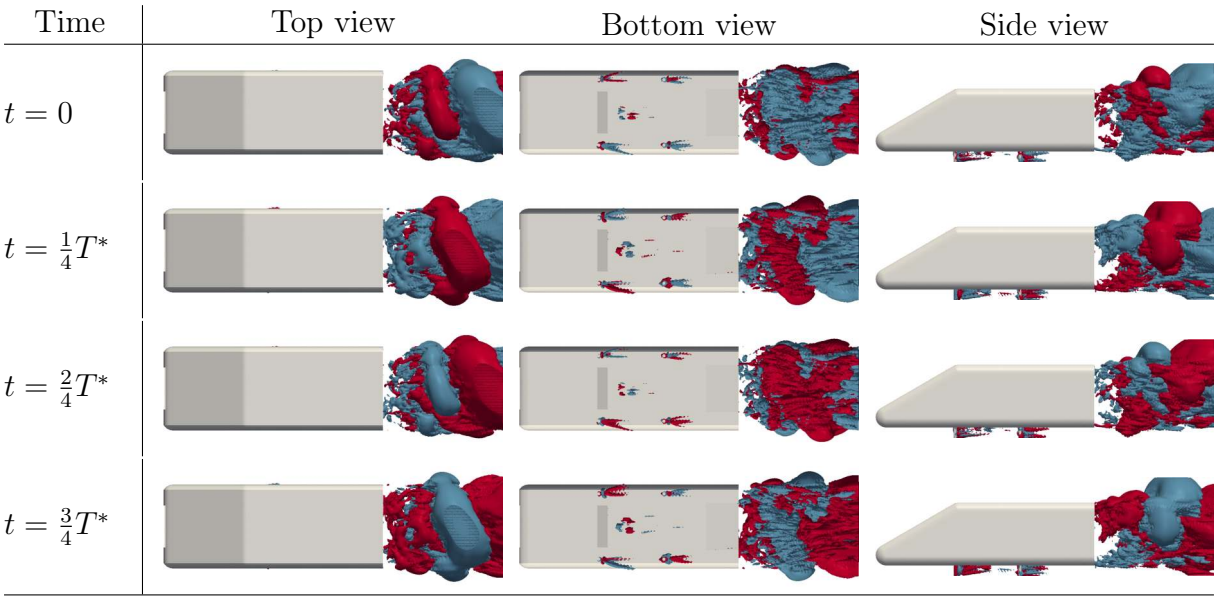

Figure 3.31: Open estate configuration. Reconstruction of one period $T^* = f^{*-1} = 0.48\,s$ of DMD mode 2. Isosurfaces of pressure. Red: $p = 20\,Pa$, blue: $p = -20\,Pa$.

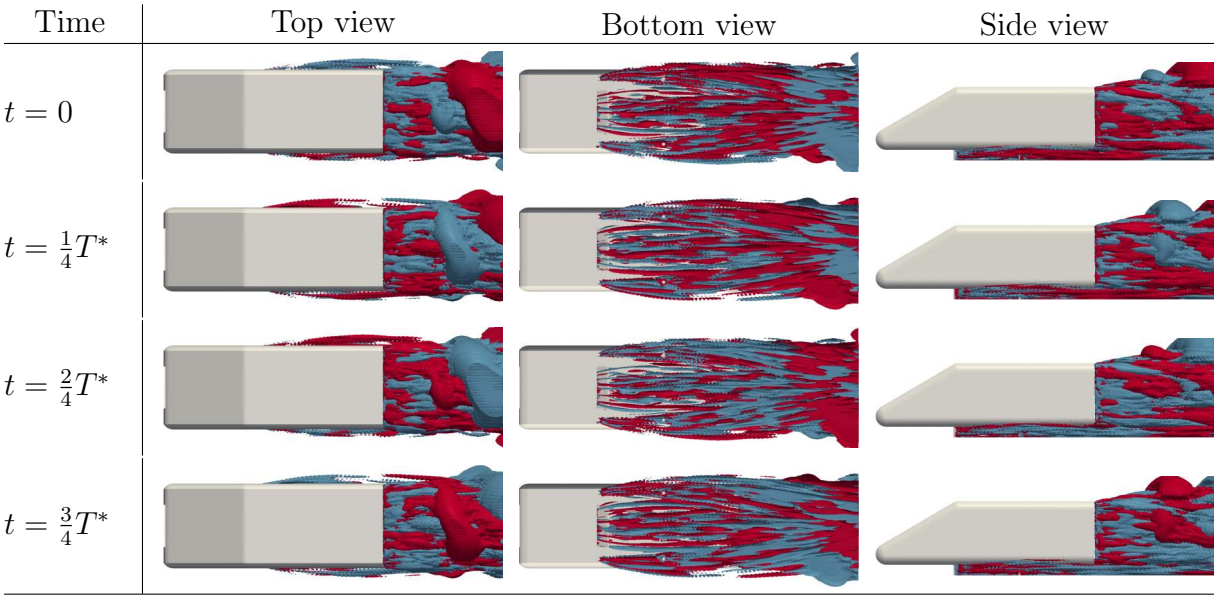

Figure 3.32: Open estate configuration. Reconstruction of one period $T^* = f^{*-1} = 0.48\,s$ of DMD mode 2. Isosurfaces of streamwise velocity component. Red: $u = 6\,m/s$, blue: $u = -6\,m/s$.

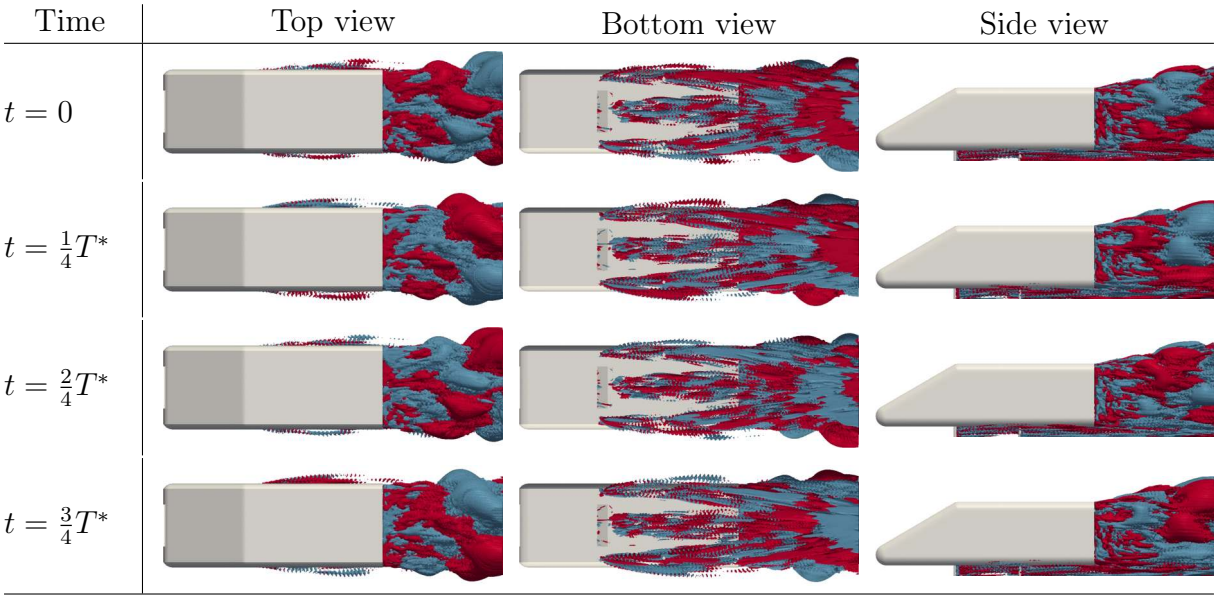

Figure 3.33: Open estate configuration. Reconstruction of one period $T^* = f^{*-1} = 0.48\,s$ of DMD mode 2. Isosurfaces of sideward velocity component. Red: $v = 6\,m/s$, blue: $v = -6\,m/s$.

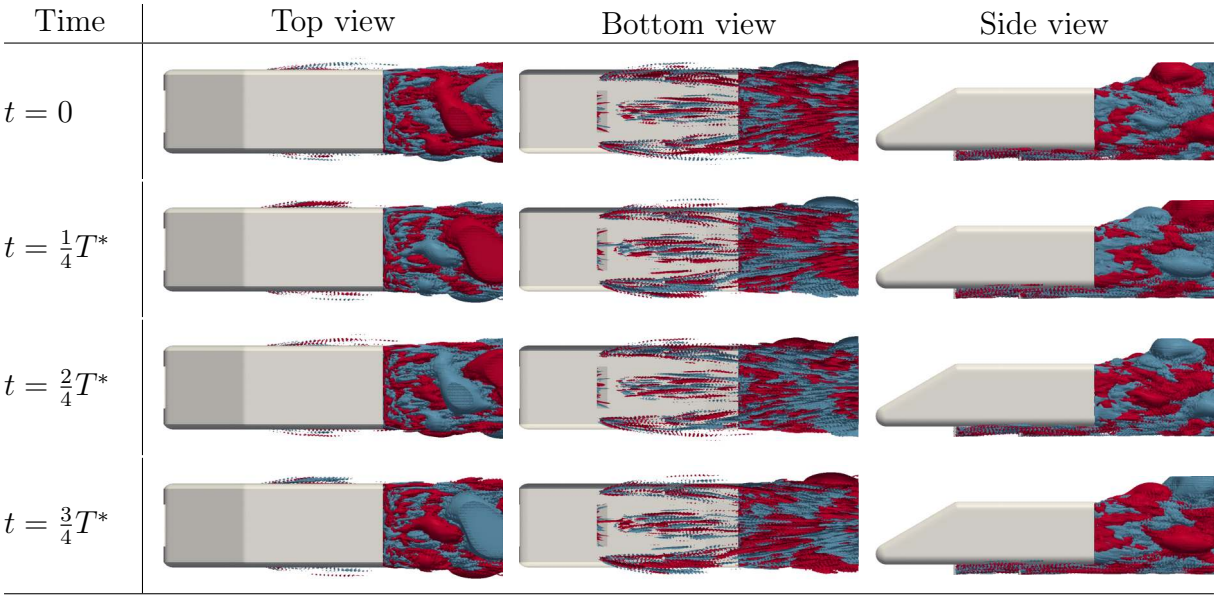

Figure 3.34: Open estate configuration. Reconstruction of one period $T^* = f^{*-1} = 0.48\,s$ of DMD mode 2. Isosurfaces of upward velocity component. Red: $w = 6\,m/s$, blue: $w = -6\,m/s$.

detachment point along the trailing edge of the geometry. As in the reconstruction of the pressure field of the notchback geometry, fluctuations from the legs of the model and from the center of the underbody downstream the opening of the engine compartment, contribute to fluctuations in the mode despite their small length scale.

The reconstruction of the u, v and w components of the velocity vector field of mode 2 are shown in Fig. 3.32, 3.33 and 3.34 respectively. The vortex shedding process, found in the pressure field of mode 2, is also visible in the reconstructions of the velocity components. The fluctuations from the legs of the model and from the opening of the engine compartment are again more dominant in the reconstructions of the velocity components than in the reconstruction of the pressure field.

3.2.3 Conclusion

The flow around four different configurations of the SAE body was investigated in this test case. The simulations were validated against published experimental data. In the published experiments, a large difference between the cooling drag coefficient $\Delta c_D = c_{D,open} - c_{D,closed}$ of the notchback and the estate configurations was found. This large difference of cooling drag coefficients could not be reproduced in the simulations. Measuring the difference between cooling drag coefficients is especially sensitive to measuring errors as four configurations have to be measured independently for a $\Delta c_{D,Notchback} - \Delta c_{D,Estate}$ value. As the measurements were not undertaken to specifically investigate the difference of cooling drag coefficients, it is assumed that the large difference between the cooling

drag coefficients in the experiments is due to a measurement error. For *difference-of-delta*-type investigations, at least one repetition and reproduction of the measurements is recommendable.

The time averaged flow of the simulations was investigated with Line Integral Convolution (LIC) pictures of the wall shear stress on the car bodies. The LIC pictures of closed and open configurations were found to be similar. The topology of the time averaged flow was investigated and documented with isosurfaces of the magnitudes of the Shear Maximizing Decomposition tensors.

The unsteady flow around the four configurations of the SAE car body was investigated with Dynamic Mode Decompositions. The DMD analyses of the four configurations were executed with the pressure and the velocity field in the DMD analyses. An important finding of this test case is the relatively strong contribution of fluctuations from the legs to the second mode. A dominant frequency of the notchback, as well as the estate configuration is of approx. $f^* \approx 2.2\,Hz$. As the configurations have considerably different rear end height but identical width, the width of the model is assumed to be the relevant length scale of this vortex shedding process. Building the Strouhal number with the width of the model results in a Strouhal number of $Sr_{Mode2} = 0.29$ for the notchback configuration and of $Sr_{Mode2} = 0.27$ for the estate configuration. Building the Strouhal number of the vortex shedding from the legs of the model with the diameter of the legs results in $Sr_{Mode2} = 0.01$. The Strouhal number of the dominant vortex shedding process of a single circular cylinder at the same Reynolds number is approx. $Sr_{Cylinder} \approx 0.2$ which is 20 times higher than the Strouhal number of the vortex shedding from the legs in mode 2. As a single, isolated circular cylinder would not produce a high amplitude vortex shedding with a Strouhal number as low as $Sr = 0.01$, the fluctuations from the legs in mode 2 must be induced by the strong vortex shedding process in the wake of the car. The fluctuations from the legs are convected into the wake flow of the car and establish a feedback loop.

A contribution to mode 2 can also be noticed from the rear slant of the notchback geometry and the generic engine compartment opening of both open configurations. Together with the wake flow, these are the unstable parts of the flow around the geometries. It appears that strong fluctuations in the subsonic flow around a bluff body induce a global oscillation in the flow and have a controlling effect on the shedding processes on other unstable parts of the flow – independent of the length scale of the controlled parts of the flow. This interaction of global modes with locally unstable parts of the flow provides an explanation for observations in wind tunnel tests, where local changes in the shape of a car upstream of the wake have different effects on notchback than on estate configurations.

3.3 DrivAer Car Model

The DrivAer model (www.drivaer.com, [38, 68]) is a realistic generic car model. It includes the main aerodynamic features of a mid-sized passenger car. The DrivAer model was developed by the Institute of Aerodynamics and Fluid Mechanics at Technical University of Munich in cooperation with AUDI AG and BMW AG. It is mainly derived from the *Audi A4* (B8, since 2007) and the *BMW 3 series* (E90/91, since 2005) [39]. The DrivAer geometry is available with different rear end shapes, different underbody geometries and different wheels. An extension with a generic engine hood is also available.

The DrivAer car model is used here to investigate the unsteady details of the flow around a realistic car geometry. The DMD is executed on the velocity vector field and on the field of force on the car body.

3.3.1 Setup

The investigated configuration of the DrivAer model is the notchback rear end with a detailed underbody. It is equipped with side mirrors; the wheels have closed rims and slick tires. No cooling airflow is considered. The Reynolds number, based on the length of the car model, is $Re = 5.2 \cdot 10^6$.

Numerical Setup

The computational domain of the simulation is a rectangular box with the approximate dimensions of: $\Delta x = 16L$, $\Delta y = 14L$ and $\Delta z = 8L$. The grid has approx. 66 million cells and is hex-dominant. The size of the cells in the vicinity of the car and in the wake is $\Delta = 8.2\,mm$ for a full scale model. Prism Layers are present at the car body and the wheels. The average dimensionless wall distance at the surface of the model is approximately $y^+ \approx 50$. To account for y^+ values below the logarithmic part of the boundary layer, an adaptive wall model is used.

The same discretization schemes, as in the test case of the SAE car bodies (Section 3.2), are used here. The convective terms are discretized by a blending between a second order central differencing scheme with a small amount of upwind and a first order upwind scheme. The gradients are computed using the Gauss theorem were the surface values are interpolated with a second order linear interpolation. The diffusive terms are approximated using a stabilized over relaxed approach to account for the non-orthogonality of the mesh. The scheme to discretize the time derivatives is second order, implicit.

The time step is adjusted to result in a CFL number smaller than 1 around the car model and in most of the domain. Unlike the setup of the SAE car body simulations, the CFL

number is allowed to reach a value up to 3 in some cells in the gap between the wheels and the ground.

As in the SAE car body simulations, the Spalart-Allmaras DDES turbulence model is used as described in section 2.2.2. To check for the correct operation of the shielding function, the wall normal eddy viscosity profiles have been compared against the velocity profile of the boundary layers.

The subvolume of the Dynamic Mode Decomposition is shown in Fig 3.35. The size of the subvolume is $\Delta x = 1.45L$, $\Delta y = 0.5L$ and $\Delta z = 0.35L$ with the length of the car L. The distance between the foremost point of the car geometry and the foremost point of the subvolume is $\Delta x = 0.05L$.

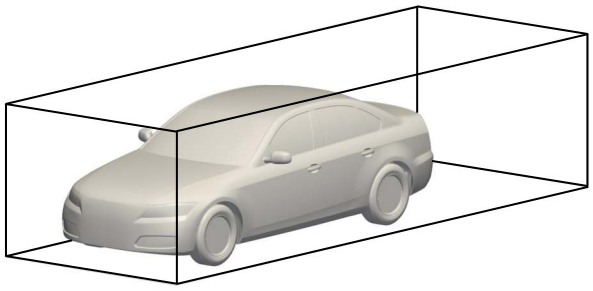

Figure 3.35: Subvolume of the Dynamic Mode Decomposition. Size of the subvolume: $\Delta x = 1.45L$, $\Delta y = 0.5L$, $\Delta z = 0.35L$.

Boundary Conditions The types of boundary conditions for the inlet and outlet of the domain are the same as for the SAE car body simulations (Section 3.2). The value for the modified eddy viscosity $\tilde{\nu}$ at the inlet is, again, chosen such that the free stream eddy viscosity ratio $\frac{\tilde{\nu}_\infty}{\nu_\infty}$ has a value of 3 directly in front of the car model as recommended by Rumsey and Spalart in [90]. The far field of the domain, the side walls and the top wall are treated as the far field walls of the SAE car body simulations. In contrast to the SAE car body simulations, the whole ground moves here with the speed of the flow velocity at the inlet and the wheels rotate accordingly. The motion of the ground and the rotation of the axially symmetric wheels are modeled with a Dirichlet boundary condition for the velocity vector. At the surface of the car model, the velocity vector and the modified eddy viscosity are set to zero. The pressure is treated with a zero gradient boundary condition.

Experimental Setup

To validate the CFD simulations, experiments were conducted in two different wind tunnels employing a 40% scaled model of the DrivAer geometry. The tests were performed in the model scale wind tunnel at Technical University of Munich (TUM) and in the full-scale wind tunnel of AUDI AG. Both wind tunnels are equipped with a rolling road system. The model is held by a Model Support System (MSS) consisting of a top-sting, a

central strut that holds the car body from above and four wheel struts to hold the wheels on the ground simulation belt. The Wheels are driven by the belt. Details of the wind tunnels were presented in chapter 2.3.1, the aerodynamic test model has been described in chapter 2.3.2. A comprehensive description of the experimental setup and a detailed description of the wind tunnel at TUM can be found in Mack et al. [67]. Details of the wind tunnel at Audi can be found in Wickern and Lindener [111].

3.3.2 Results

Time averaged flow

The pressure coefficient in the symmetry plane of the vehicle on the upper part of the vehicle's surface is shown in Fig. 3.36. Despite considerable different nozzle cross sections of the two wind tunnels, the results of the experiments (symbols) are in good agreement. The simulation data (line) matches the experimental results on the engine hood and the windshield. On the roof of the car, the pressure coefficient of the simulation is lower than in the experiments. This is explained by the top-sting (its position is indicated by the dashed lines; see [67] for details). The top-sting, as well as the wheel struts, are used in the experiments but are not present in the simulation. Towards the rear window, the simulation and experimental results again agree well.

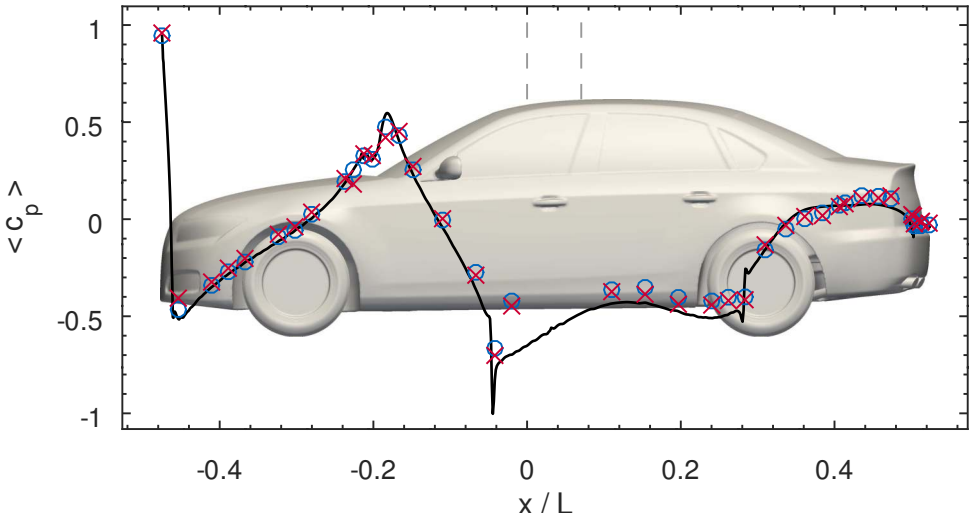

Figure 3.36: Pressure coefficient in the $y = 0$ plane of the vehicle. Upper part. (Solid line: Simulation, blue circles: TUM wind tunnel, red crosses: Audi wind tunnel)

Fig. 3.37 shows the pressure coefficient in in the symmetry plane at the underbody. Small deviations between the experimental results from the different wind tunnels can be noticed. These deviations may be related to the small momentum deficit of the ground

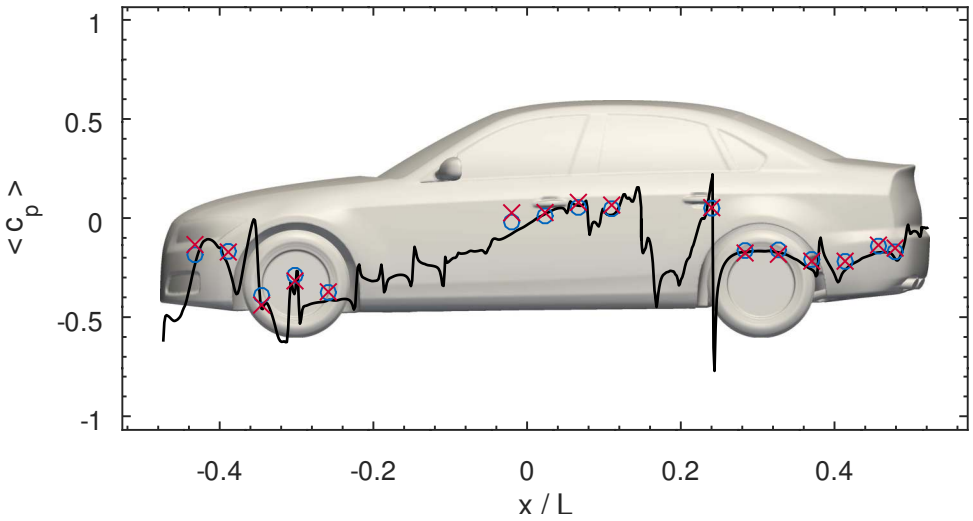

Figure 3.37: Pressure coefficient in the $y = 0$ plane of the vehicle. Lower part. (Solid line: Simulation, blue circles: TUM wind tunnel, red crosses: Audi wind tunnel)

boundary layer which is present in the TUM wind tunnel (see [67]). The agreement between simulation and experimental results is still good.

Figure 3.38 shows the pressure coefficient in a ground parallel plane on the left side of the car, indicated by the dashed line ($z = 0.102L$ above the ground, $y < 0$). The simulation results are, again, in good agreement with the experimental data.

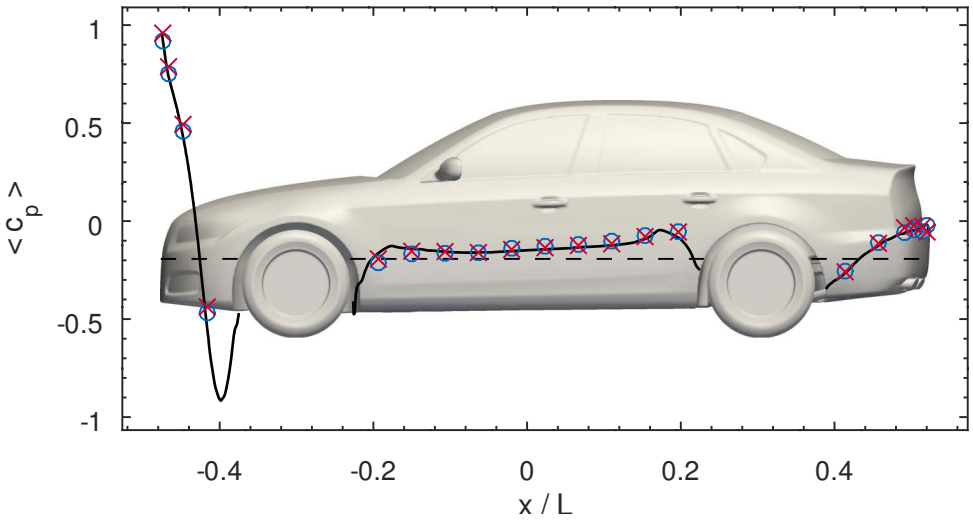

Figure 3.38: Pressure coefficient in the $z = 0.102L$ plane of the vehicle. (Solid line: Simulation, blue circles: TUM wind tunnel, red crosses: Audi wind tunnel)

The drag coefficients of the full vehicle, including wheels and lift coefficients of the vehicle body, excluding wheels, are shown in Table 3.2. The uncorrected drag coefficient of the

simulation is 15 counts (5.2 %) lower than the value measured in the Audi wind tunnel and 5 counts (1.8 %) lower than the value measured in the TUM wind tunnel. The lift coefficient of the simulation is 11 counts lower than the value measured in the Audi wind tunnel and 30 counts higher than the value measured in the TUM wind tunnel. As the simulation has been executed without the model support system (MSS) consisting of the wheel-struts to hold the wheel on the ground simulation belt and the top-sting to hold the model, the drag coefficient of the simulation is lower than the measured drag coefficients. Heft found in a previous study [39] that the MSS increases the drag coefficient for the DrivAer model in a notchback configuration by $\Delta c_D = 0.006$. Correcting the drag coefficient of the simulation by $\Delta c_D = 0.006$, the drag coefficient of the simulation is 9 counts (3.1 %) lower than the value measured in the Audi wind tunnel and 1 count (0.4 %) larger than the value measured in the TUM wind tunnel. The influence of the model support system on the measured lift values is not yet clear. The reproducibility of the experimental results in the same wind tunnel is estimated for the drag coefficient to be approximately $\Delta c_D \pm 0.0015$, for the lift coefficient to be approximately $\Delta c_L \pm 0.0045$ and for the pressure coefficient, depending on the position on the geometry, up to approximately $\Delta c_p \pm 0.01$.

Table 3.2: Drag coefficient c_D of the full vehicle including wheels and lift coefficient $c_{L,Body}$ of the vehicle body excluding wheels. The simulations are executed without model support system (MSS)

	TUM wind tunnel	Audi wind tunnel	Simulation (without MSS)
c_D	0.279	0.289	0.274
$c_{L,Body}$	0.032	0.073	0.062

A Line Integral Convolution on the time averaged wall shear stress field on the car body is shown in Fig. 3.39. The downward oriented streaks at the A-pillar show the effect of the A-pillar vortex on the wall shear stress. The A-pillar vortex follows the motion of the fluid on the roof of the car geometry. In the side view of the geometry, an upward motion of the flow is visible at the side windows. Circular pattern can be found at the front and rear wheels and downstream the rear wheels, were vortices detach from the surface. Another clear reattachment line is visible in the top view of the geometry on the windshield. Here, a vortex tube rotates in the cavity between engine hood and the windshield. The flow detaches at the trailing edge of the engine hood and reattaches on the windshield downstream the vortex tube. The effect of the C-pillar vortex on the wall shear stress is visible by the detachment lines on the C-pillars. The streamwise and outward oriented patterns on the outer parts of the trunk are due to the outward motion of fluid in the C-pillar vortices near the car surface. Between the C-pillar vortices, circular LIC pattern indicate the detachment of four vortices. The two outer vortices rotate against the C-

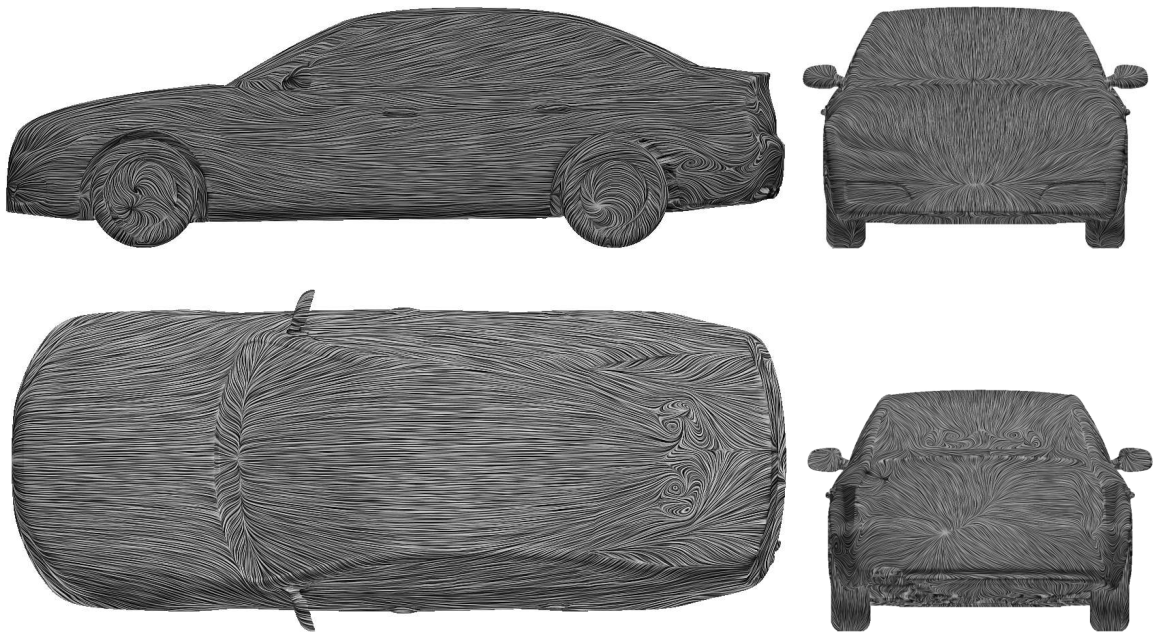

Figure 3.39: Line Integral Convolution (LIC) of the time averaged wall shear stress on the DrivAer car body.

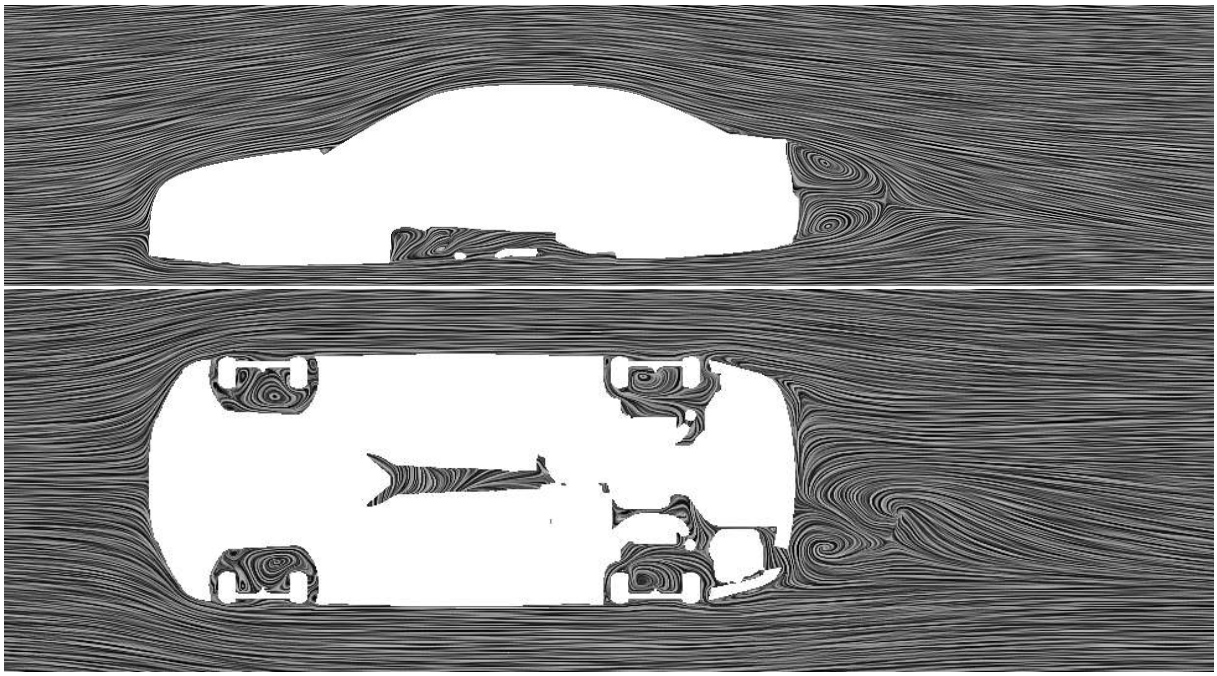

Figure 3.40: Line Integral Convolution (LIC) of the time averaged velocity in the flow around the DrivAer car body. Top: $y = 0$ plane, bottom: $z = const.$ plane at the height of the stagnation point.

pillar vortices, while the two inner vortices rotate in the same direction as the C-pillar vortices. The inner vortices are connected by another detachment line. This detachment line indicates a recirculation zone between the vortices. The LIC pattern on the rear window, the trunk and on the back of the car is not symmetric with respect to the $y = 0$ plane. This asymmetry is due to the asymmetric underbody.

The orientation of the time averaged velocity field in the coordinate system of the vehicle geometry is shown in Fig. 3.40. The upper picture shows the $y = 0$ plane of the geometry. Two distinct circulating patterns can be found in the near wake of the car body. The wake flow forms two three dimensional recirculation vortices at the rear end of the car. As the flow is asymmetric, the $y = 0$ plane cuts through one of the vortices. The lower picture shows a LIC on the $z = const.$ plane at the height of the stagnation point, below the recirculation vortices in the wake. Here, the asymmetry of the flow from the underbody is clearly visible.

Figure 3.41: Isosurface of the magnitude of the rotation rate tensor from the Shear Maximizing Decomposition, $||(\nabla U)_{RR}|| = 10\,s^{-1}$.

The vortex core regions of the most dominant Vortices in the time averaged flow around the geometry are shown by isosurfaces of the magnitude of the rate of rotation tensor $||(\nabla U)_{RR}||$ in Fig. 3.41. Vortex tubes form from the side mirrors, the A-pillars, the C-pillars, the wheels and from the rear window. Two ring shaped vortices and another streamwise oriented vortex can be seen in the near wake of the car. The isosurfaces of these vortices are rough as they are interpenetrated by smaller vortices with high rotation rate from the shear layers around the car.

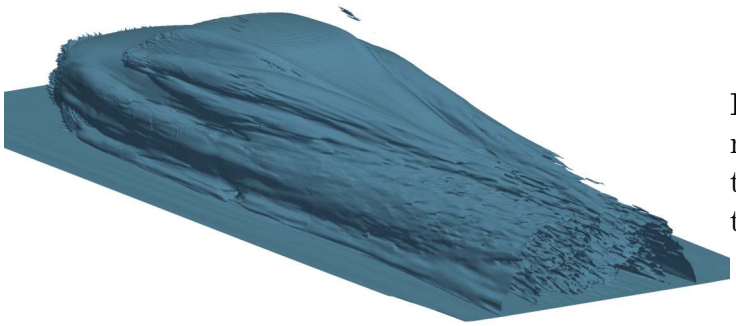

Figure 3.42: Isosurface of the magnitude of the shear rate tensor from the Shear Maximizing Decomposition, $||(\nabla U)_{SH}|| = 10\,s^{-1}$.

The shear layers around the car are shown in Fig. 3.42 by isosurfaces of the magnitude of the rate of shear tensor $||(\nabla U)_{SH}||$. Tube shaped shear layers detach from the front

wheels, the side mirrors and from the A-pillar around the A-pillar vortices. The shear layers extend into the wake of the car and combine to large tubular structures. Although the ground is modeled to move with the oncoming flow, a shear layer develops on the ground. The shear on the ground has been clipped for better visibility.

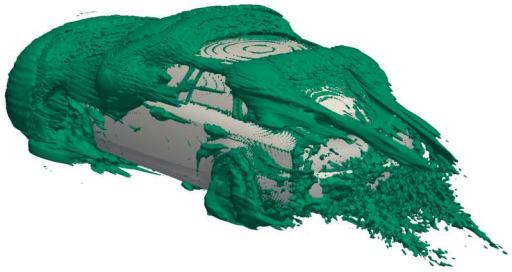

Figure 3.43: Isosurface of the magnitude of the elongation rate tensor from the Shear Maximizing Decomposition, $||(\nabla U)_{EL}|| = 10\,s^{-1}$.

The irrotational part of the relative motions in the flow are visualized with isosurfaces of the magnitude of the elongation rate tensor $||(\nabla U)_{EL}||$ in Fig. 3.43. The picture shows the stretching and the irrotational deflection of flow around the car. The main contributions to the elongation in the flow are were the oncoming flow is redirected at the front of the geometry, around the edges of the windshield and around the edges of the rear window. The elongated structures from the C-pillars are assumed to be mainly due to the inward deflection of the flow.

Unsteady Flow

The unsteady flow is investigated here with focus on the unsteady forces acting on the car body. The Dynamic Mode Decomposition is applied on the velocity field and on the field of force per unit area on the car body. The two most dominant modes of the analysis are selected for an exemplary investigation.

Dynamic Mode Decomposition The DMD is executed with $N_{DMD} = 800$ time steps, a time step length of $\Delta t_{DMD} = 0.005\,s$ and a total time span of $T_{DMD} = 4\,s$. As in the previous test cases, the time step data is filtered with a 4th order low-pass filter with a ratio of cut-off frequency to Nyquist frequency of 0.1. After the singular value decomposition in the DMD algorithm, the projection basis is restricted to modes with a relative contribution of more than $1 \times 10^{-4}\,\%$ to the total variance of the flow. Prior to the analysis, the fields of forces and velocities are scaled independently to unit variance.

The normalized amplitudes and frequencies of the modes are shown in Fig. 3.44. The amplitudes are computed separately for the velocities and for the forces. For the forces, amplitudes are computed as norm of force data in the mode. For the velocities, amplitudes are computed as the volume-weighted norm of the velocity data in the mode. Most of the

energy of the flow falls into the mode that represents the mean flow. Sorting the modes by their amplitudes, the relative force amplitude of the second mode is 23%; the relative velocity amplitude of the second mode is 17%.

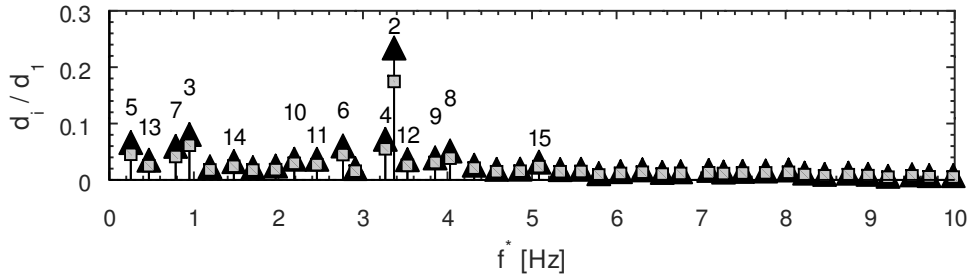

Figure 3.44: Relative amplitude over full scale frequency. Amplitudes of the dynamic modes normalized by amplitude of the first mode. Mode numbers by decreasing amplitude. Triangles: force, squares: velocity.

Isosurfaces of the velocity components of the flow are shown in Fig. 3.45 for a reconstruction of mode 2 and in Fig. 3.46 for a reconstruction of mode 3. Mode 2 with a frequency of $f = 3.4\,Hz$ contains the fluctuations of highest energy in the flow. Mode 2 is not a single oscillating process, but rather a collection of individual oscillations with common frequency falling into the same mode. The oscillations in the velocity field combine and result in the oscillations of the force on the surface of the car. The tubular structures found in the isosurface pictures of the u component of mode 2 show that the mode is mainly connected to motions of vortex tubes. The strongest contribution to this mode comes from the wake of the car and from the underbody (not shown). Other contributions originate from the wheels, the windshield apron, the side mirrors and the front apron.

The isosurface pictures of mode 3 (Fig. 3.46), with a frequency of $f = 0.9\,Hz$, show large connected regions of oscillating fluid in the wake of the car. The locally unstable flow around the side mirrors, at the bottom of the windshield or at the front apron also shows vortex shedding in the low frequency of the large oscillating areas in the wake of the car. Assuming that these local shedding processes with much smaller lengthscales than the oscillations in the wake of the car would not produce high energy fluctuations with a time scale of $T = 1.1\,s$, the local vortex shedding must be triggered by the fluctuations of the wake flow. This effect of *global modes* has also been found in the previous test case of the SAE car body configurations.

The lift force per unit area normalized by the force per area at the stagnation point $(F_Z/A)/(p_\infty + \frac{\rho}{2}U_\infty^2)$ is shown for mode 2 and 3 in figures 3.47 and 3.48 respectively. The reconstruction of mode 2 shows a strong lift force oscillation between the rear wheels and at the rear diffuser of the underbody. The same oscillation, but weaker, can be seen on the lower edge of the rear window and on the top of the trunk. The oscillation of the

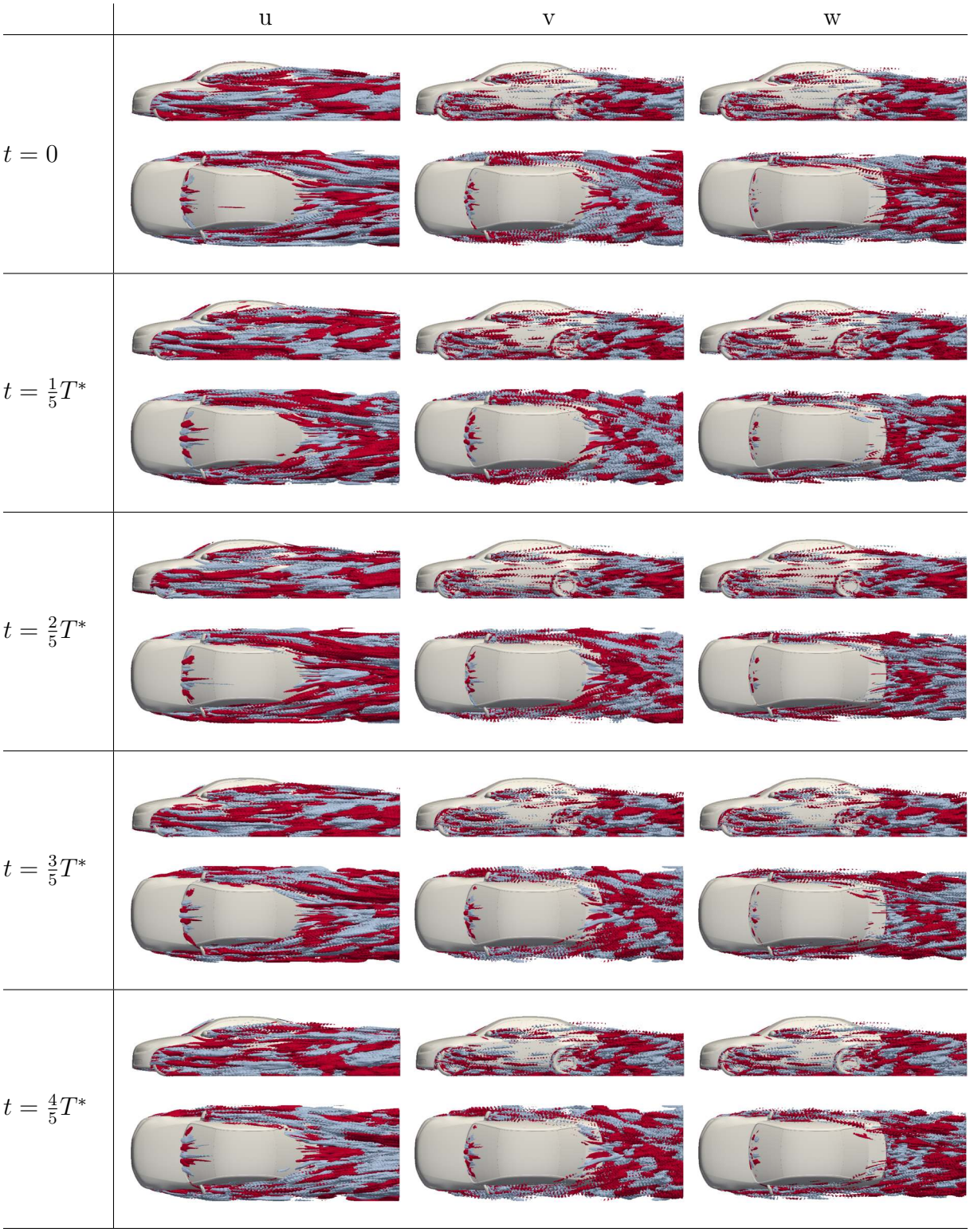

Figure 3.45: Reconstruction of one period of the mode 2 ($f = 3.4\,Hz$). Positive (red) and negative (blue) isosurfaces of the velocity components $u = v = w = \pm 1\,m/s$.

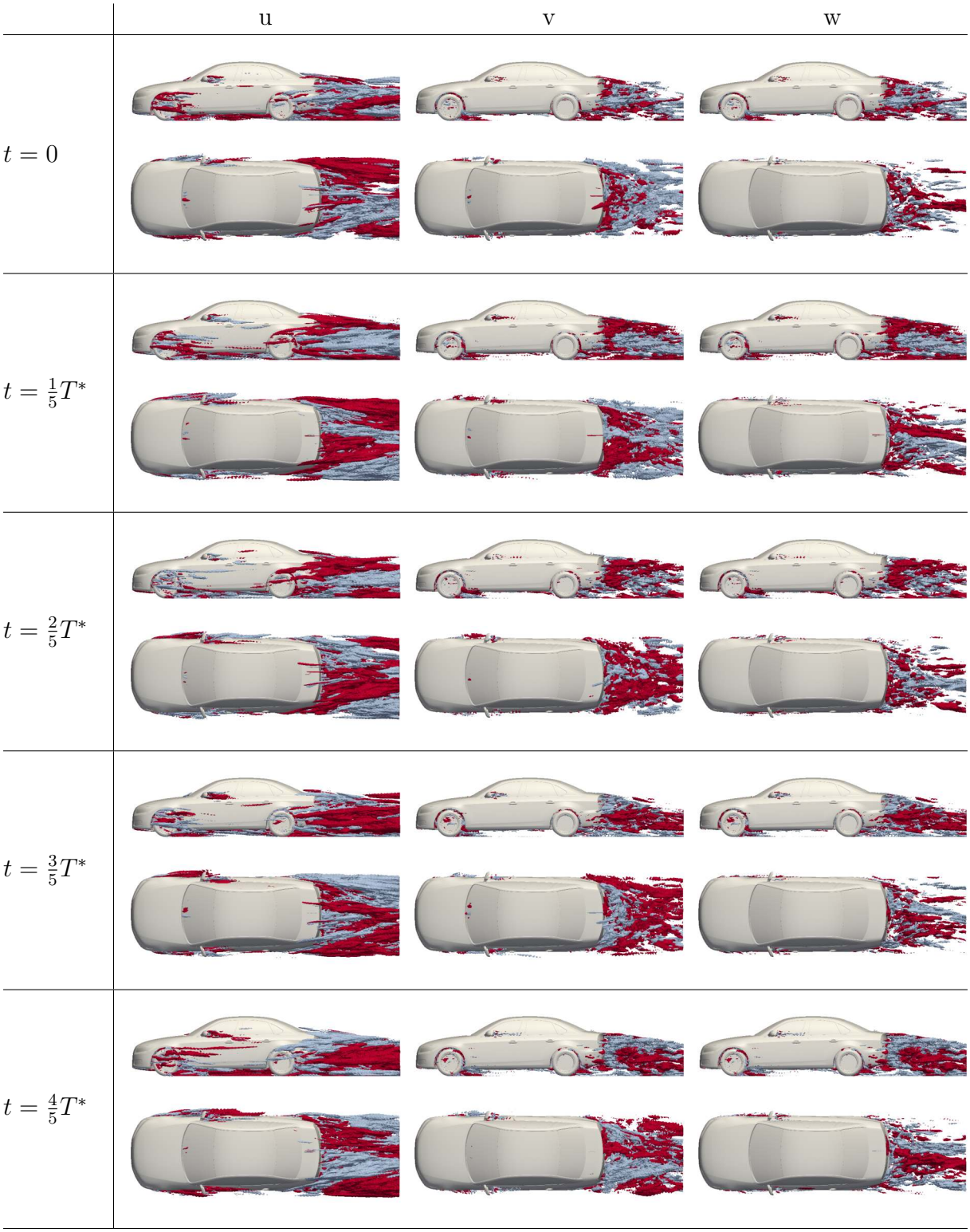

Figure 3.46: Reconstruction of one period of the mode 3 ($f = 0.9\,Hz$). Positive (red) and negative (blue) isosurfaces of the velocity components $u = v = w = \pm 1\,m/s$.

lift force between the front wheels is phase shifted to the oscillation on the back of the car. This induces an oscillating pitching moment on the car body. Other fluctuations can be found at the front apron, behind the wheels, in the middle tunnel of the underbody, behind the side mirrors and at the lower edge of the windshield. The normalized lift force of a reconstruction of mode 3 is shown in Fig. 3.48. The lift force at the rear of the car – at the underbody diffuser, between the rear wheels and on the top of the trunk – is a counter oscillation between the right and left side of the vehicle. The oscillation of the lift force between the front wheel and the middle part of the underbody is largely symmetric in y-direction, but also counter oscillating. The lift forces acting on the rear of the car induce a rolling moment, while the oscillations between the front wheels result in a pitching moment on the car body. Other oscillations can be found at the front apron, the lower part of the windshield and behind the mirrors.

The force coefficients computed from the surface integrated force components of mode 2 and 3 are shown in Fig. 3.49 for one period of the oscillation. The strongest components of the oscillating force in mode 2 are the lift and drag components as expected from the surface plots in Fig 3.47. The side force is comparatively weak. The lift and drag oscillations are phase shifted by approx. half a period. The amplitude of the oscillating force in mode 3 is lower than the amplitude of mode 2. The side and lift force components oscillate nearly in phase, while the drag force oscillation is phase shifted by approx. half a period to the other components.

The moment coefficients computed from the components of the surface integrated moments acting on the car geometry are shown in Fig. 3.50. The center of rotation is located in the $y = 0$ plane symmetrically between the wheel axes on the ground. The dominant oscillation of mode 2 is, as expected from the surface plots in Fig 3.47, the pitching moment. The yaw moment is in phase with the pitching moment, while the rolling moment is phase shifted by half a period. The pitching moment is the weakest component of the moment in mode 3. The yaw and rolling moment of mode 3 are stronger and have comparable magnitude. The moments of mode 3 do not show a clear co or counter oscillation.

The individual dynamic modes show a part of the dynamics of the flow. A reconstruction with all modes would reproduce the original flow up to the filtering with the low pass filter and the projection step onto a reduced POD basis in the DMD algorithm. A reconstruction with only a subset of modes can be seen as a superposition of individual parts of the dynamic behavior of the flow. In Fig. 3.51, the surface integrated lift force and yaw moment is shown for a reconstruction of modes 1 and 2 (dotted line), modes 1 to 3 (dash dotted line) and modes 1 to 15 (dashed line). The force and moment for the reconstruction with the mean mode and the second mode is an oscillation around the mean value. The other two reconstructions result in a more complex dynamic behavior. While the DMD analysis has been executed, for the velocity vector field in a subvolume of

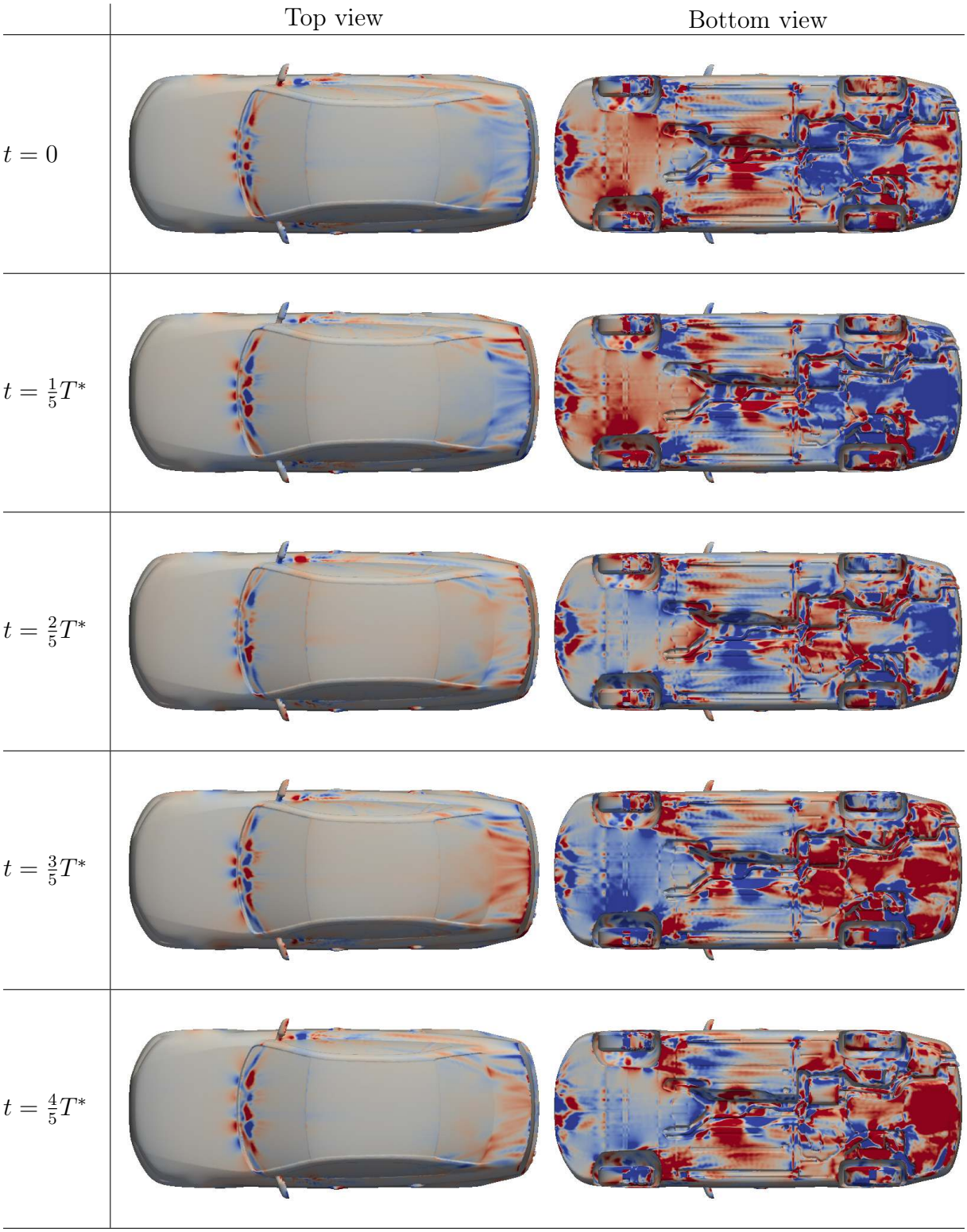

Figure 3.47: Reconstruction of one period of the mode 2 ($f = 3.4Hz$). Normalized lift force $(F_Z/A)/(p_\infty + \frac{\rho}{2}U_\infty^2)$ values ranging from -0.05 (blue) to $+0.05$ (red).

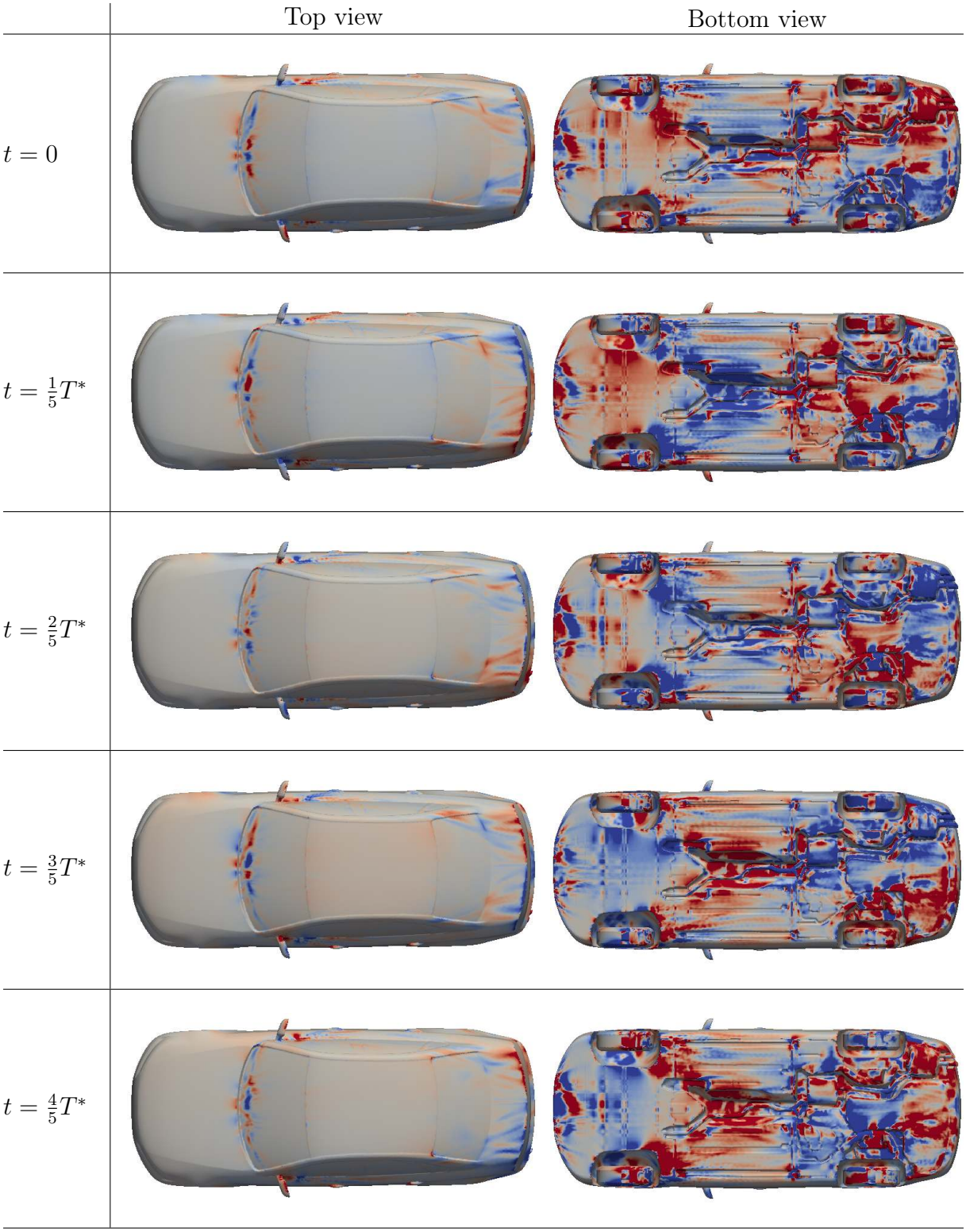

Figure 3.48: Reconstruction of one period of the mode 3 ($f = 0.9\,Hz$). Normalized lift force $(F_Z/A)/(p_\infty + \frac{\rho}{2}U_\infty^2)$ values ranging from -0.02 (blue) to $+0.02$ (red).

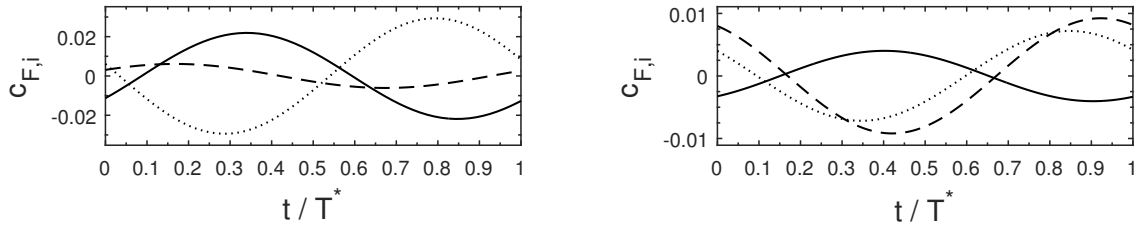

(a) Mode 2 **(b)** Mode 3

Figure 3.49: Force coefficients computed from the components of the surface integrated force of a reconstruction of mode 2 and a reconstruction of mode 3. Solid line: drag force coefficient, dashed line: side force coefficient, dotted line: lift force coefficient.

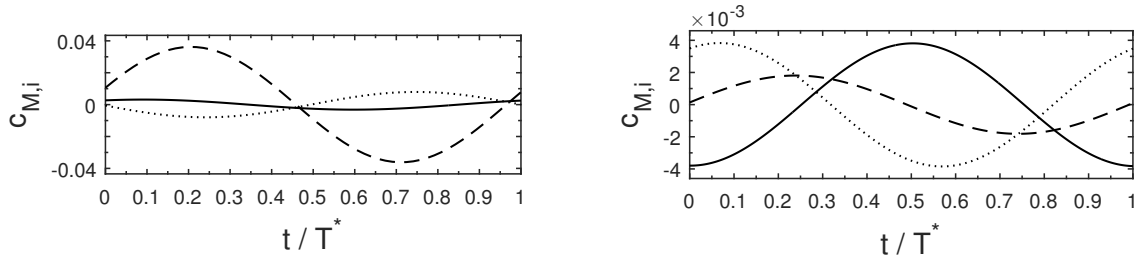

(a) Mode 2 **(b)** Mode 3

Figure 3.50: Moment coefficients computed from the components of the surface integrated moment of a reconstruction of mode 2 and a reconstruction of mode 3. Solid line: roll moment coefficient, dashed line: pitch moment coefficient, dotted line: yaw moment coefficient.

the domain and the vector field of force per area on the surface of the car, the reconstruction here shows only a small part of the information processed in the DMD. Therefore a reconstruction with an increasing number of modes will not necessarily converge monotonically to the original force signal of the CFD simulation. To show this effect, the normalized root-mean-square deviation for the deviation between the reconstruction and the original force or moment signal is shown in table 3.3. The deviations are higher for a reconstruction with the modes 1, 2 and 3 then for a reconstruction using only mode 1 and 2. For a reconstruction using the first 15 modes, the deviations are reduced. This effect can be found for the reconstruction of the lift force and its coefficient c_L as well as for the reconstruction of the yaw moment and its coefficient $c_{M,z}$.

The normalized root-mean-square deviation is computed with equation 3.1:

$$\mathrm{RMS_{N,D}} = \frac{1}{\phi_{max} - \phi_{min}} \sqrt{\frac{\sum_{t=1}^{n} (\phi_{ref,t} - \phi_{recon,t})^2}{N}} \tag{3.1}$$

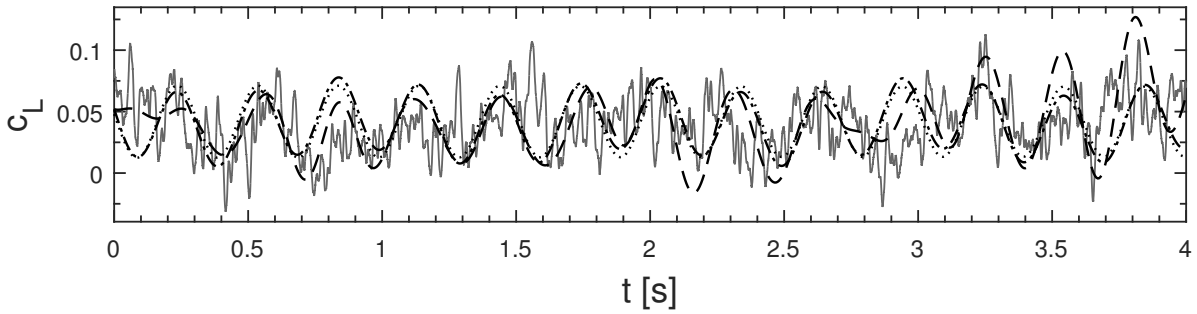

(a) Lift force coefficient

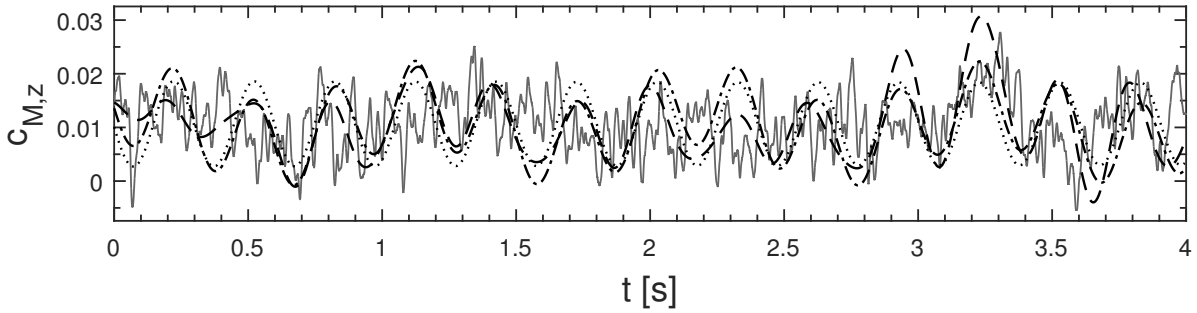

(b) Yaw moment coefficient

Figure 3.51: Lift force coefficient and yaw moment coefficient of the original cfd simulation (solid line), a reconstruction with modes $\{1, 2\}$ (dotted line), modes $\{1, 2, 3\}$ (dash dotted line) and modes $\{1, \ldots, 15\}$ (dashed line).

Table 3.3: Normalized root-mean-squares of the deviation between the result of the CFD simulation and the reconstruction with different numbers of modes

Modes	$\{1, 2\}$	$\{1-3\}$	$\{1-15\}$
$\mathrm{RMS}_{\mathrm{N,D}}$ of c_L	0.213	0.215	0.200
$\mathrm{RMS}_{\mathrm{N,D}}$ of $c_{M,z}$	0.239	0.243	0.219

were $\phi_{ref,t}$ is the force or moment coefficient of the CFD simulation at time t, $\phi_{recon,t}$ is the force or moment coefficient of the reconstruction at time t, $\phi_{max,ref}$ and $\phi_{min,ref}$ are the max and min values of the force or moment coefficients of the CFD simulation and N is the number of values.

A Line Integral Convolution (LIC) of the force vector field for a reconstruction of the mean mode 1 and the mode 2 is shown in Fig. 3.52. The image section shows the bottom of the rear window and a part of the top of the trunk. In both pictures, the C-pillar vortices are noticeable by streaks in the direction of the C-pillar and the side edges of the trunk. Vortex cores are indicated by crosses and circles. In the upper picture, $t = 0$, the crosses and the circles indicate the vortex cores of two longitudinal vortex tubes that are connected

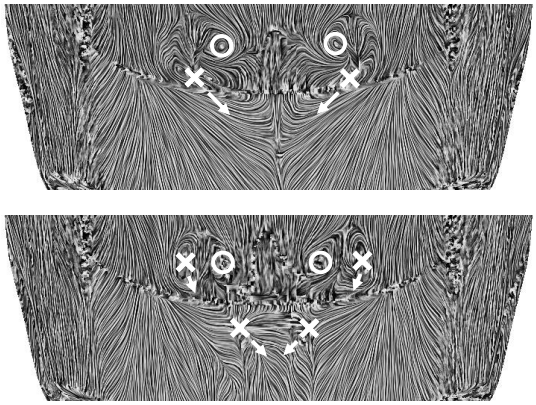

Figure 3.52: Line Integral Convolution (LIC) of the force field on the car surface. Reconstruction of mode 1 and mode 2 at $t = 0$ and after half a period $t = \frac{1}{2}T$. Image section: Bottom of the rear window and part of the top of the trunk. Flow from top to bottom.

by a recirculation vortex similar to the vortex system found by Gilhome et al. in [32] (see [32] or [93] for a qualitative sketch of the vortex topology). The recirculation vortex and the vortex tubes indicated by crosses rotate opposite to the direction of the C-pillar vortices. The vortices of the circles have the same rotation as the C-pillar vortices. In the lower picture, after half a period of the oscillation, $t = \frac{1}{2}T$, the vortex system indicated by crosses is moved down onto the trunk deck where it detaches as a hairpin vortex. The separation and reattachment lines on the trunk deck show the "legs" of the hairpin vortex. Another vortex system with recirculation and longitudinal vortices establishes immediately on the rear window. The vortex system of circles follows the motion of the detaching vortices and oscillates down and up on the rear window. The periodic shedding of hairpin vortices from a recirculation vortex in the near wake of a notchback vehicle was also described by Guilhome et al. in [32]. While Guilhome et al. are describing a vortex system with a stable recirculation vortex and a periodic shedding of hairpin vortices from this recirculation zone, the reconstruction of mode 1 and 2, shown here, identifies an oscillating vortex system on the rear window and a second vortex system that detaches periodically from the trunk deck.

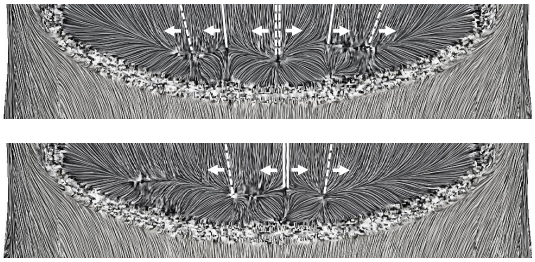

Figure 3.53: Line Integral Convolution (LIC) of the force field on the car surface. Reconstruction of mode 1 and mode 2 at $t = \frac{1}{4}T$ and after half a period $t = \frac{3}{4}T$. Image section: Lower part of the windshield. Flow from bottom to top.

Another vortex shedding process can be found at the lower part of the windshield, shown in Fig. 3.53. The pictures, again, show a Line Integral Convolution (LIC) of the force field on the surface of the car for a reconstruction of mode 1 and 2. In both pictures, a stationary recirculation zone at the bottom of the windshield can be identified by the streaks in the direction of the engine hood. From this recirculation, longitudinal vortices form on the windshield (solid lines indicate separation lines, dashed lines indicate reattachment lines).

The longitudinal vortices form in the middle of the windshield move outward and are convected over the A-pillar and the roof of the car.

3.3.3 Conclusion

In this test case, the CFD simulation was validated by experimental results measured in two different wind tunnels. The pressure and force coefficients of the experiments were found to be in good agreement with results from the Detached Eddy simulation. The time averaged flow around the DrivAer car body was documented by Line Integral Convolution pictures of the wall shear stress and the velocity vector field. A Shear Maximizing Decomposition of the time averaged flow field was used to give an overview of the topology of the flow.

The Dynamic Mode Decomposition was applied to force and velocity vector fields. With isosurface plots of reconstructed velocity components and surface plots of the reconstructed lift force, a clear connection could be shown between flow structures and force oscillations for mode 3. As mode 2 consists of a collection of shedding processes, the force oscillation of mode 2 was found to be the result of many different processes that fall into the same mode. With Line Integral Convolutions of the reconstructed force field, the DMD was shown to be able to isolate individual dynamic processes like the shedding of hairpin vortices from the near wake of the notchback geometry or the formation of longitudinal vortices on the windshield. With evaluations of the force and moment coefficients of modes 2 and 3, the main sources of flow induced car body oscillations could be shown. The flow fields of the modes together with the force plots and the force and moment coefficients allow connecting the resulting motion of a real car body to the topology of the dominant oscillations in the flow field.

Again, like in the previous test case of the SAE car body, it was found that flow structures with a relatively small length scale contribute to modes with relatively long time scales. This supports the assumption in the previous test case that strong fluctuations control other unstable parts of the flow.

3.4 Convertible Car Model

The car model used in this test case is an aerodynamic test model of convertible type based on the *Audi A5 Cabriolet* (since 2009). The model has an open roof and closed side windows. Two anthropomorphic dummies are included to resemble the driver and co-driver.

In this test case, the low energy flow fluctuations in the passenger compartment of the convertible are described and linked to the fluctuations of flow induced forces on the anthropomorphic dummies. A low frequency fluctuation of aprrox. $1\,Hz$ has been observed in preceding wind tunnel tests and is explained here.

3.4.1 Setup

The convertible car model is a left-hand drive vehicle. It is modeled without ground motion and non-rotating wheels. No additional rear wind screen is considered. The free stream velocity in the full scale is $140\,km/h$ ($87\,mph$). The Reynolds number, based on the length of the car model, is $Re = 1.15 \cdot 10^7$.

Figure 3.54: Geometry of the convertible car model. Side windows are included in the simulations but not shown here.

Numerical Setup

The grid of the numerical model has approx. 94 million cells and is hex-dominant. Prism Layers are present at the car body, the wheels and the ground. The average dimensionless wall distance at the surface of the model is approximately $y^+ \approx 50$. An adaptive wall model is used. The computational domain of the simulation is a rectangular box with the approximate dimensions of: $\Delta x = 16L$, $\Delta y = 13L$ and $\Delta z = 8L$. The numerical methods are based on the simulation setup described in Islam et al. [44].

The subvolume of the Dynamic Mode Decomposition is shown in Fig 3.55. The size of the subvolume is $\Delta x = 1.3\,L$, $\Delta y = 0.5\,L$ and $\Delta z = 0.23\,L$ with the length of the car L. The distance between the foremost point of the car geometry and the foremost point of the subvolume is $\Delta x = 0.05\,L$. The distance between the ground and the lowest point of the subvolume is $\Delta z = 0.11\,L$

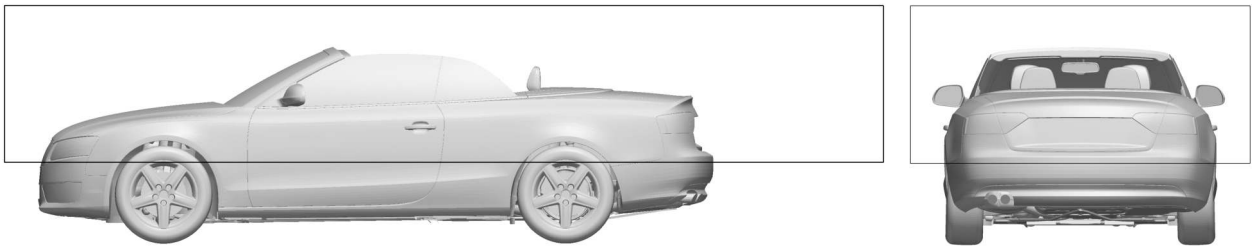

Figure 3.55: Subvolume of the Dynamic Mode Decomposition. Size of the subvolume: $\Delta x = 1.3\,L$, $\Delta y = 0.5\,L$, $\Delta z = 0.23\,L$.

Boundary Conditions The inflow to the domain is a constant, uniform velocity distribution. The velocities at the ground and at the car model are set to zero. Pressure is treated with a zero gradient Neumann condition at the inlet, the car model and the ground and with a constant value Dirichlet boundary condition at the outlet of the domain.

3.4.2 Results

Time averaged flow

The orientation of wall shear stress on the convertible car model is shown by a Line Integral Convolution of the time averaged wall shear stress in Fig. 3.56. On the upper picture, the detachment and reattachment line of the A-pillar vortex is visible. Upward oriented lines on the side windows indicate that the A-pillar vortex extends over the upper edges of the side windows.

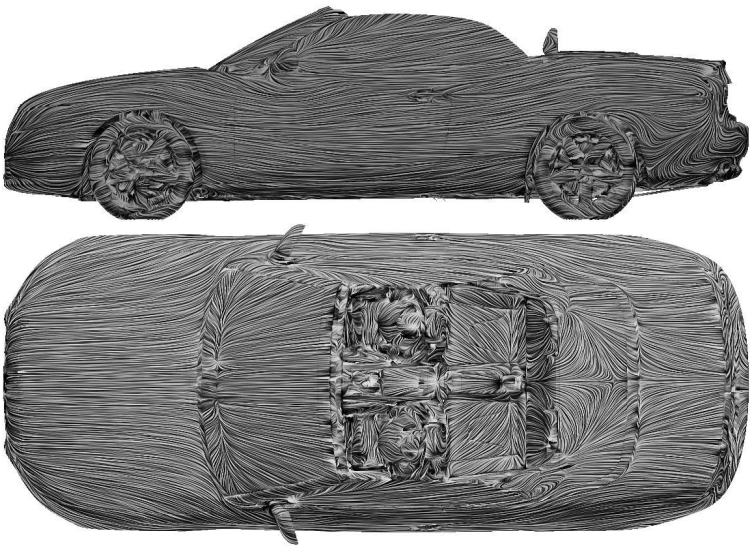

Figure 3.56: Line Integral Convolution (LIC) of the time averaged wall shear stress on the convertible car model.

In the lower picture in Fig. 3.56, the typical LIC pattern on the windshield, already described in the DrivAer car body test case, can be found. The flow forms a recirculation zone on the lower part of the windshield with a clear reattachment line. At the end of the

side windows, small circulating pattern can be found, indicating the presence of inward rotating vortices at the rear edges of the side windows. Directly behind the rear passenger compartment, the reattachment line of the main flow is visible.

Figure 3.57: Line Integral Convolution (LIC) of the time averaged wall shear stress on the anthropomorphic dummy of the driver side. Left picture: inner side view, middle picture: front view, right picture: view from side window.

The wall shear stress on the anthropomorphic dummies is low. The Line Integral Convolution pattern on both dummies show a stagnation point on the lower chest with upward oriented lines. Attachment and separation lines on the arms and shoulders indicate the presence of vertically oriented vortex tubes. The irregular LIC pattern on the inner sides of the heads of the dummies is due to a wall shear stress near zero. On the outer sides of the heads, another stagnation point can be seen. The LIC pattern on the two dummies is very similar with a symmetry in the symmetry plane of the vehicle.

Figure 3.58: Line Integral Convolution (LIC) of the time averaged wall shear stress on the anthropomorphic dummy of the co-driver side. Left picture: view from side window, middle picture: front view, right picture: inner side view.

A Line Integral Convolution of the time averaged velocity is shown in Fig. 3.59. The upper picture shows a large clockwise rotating vortex in the passenger compartment. The vortex is driven by the main shear layer starting from the windshield. Other vortices can be found in the near wake of the car and at the underbody. A free stagnation point is visible above the rear part of the vehicle geometry.

In the lower picture, two vortices can be found in front of the anthropomorphic dummies. The vortex on the driver side rotates clockwise; the vortex on the passenger side rotates counter clockwise. Another pair of vortices is present in the rear passenger compartment. Here, the driver side vortex rotates counter clockwise while the passenger side vortex rotates clockwise. Other vortices in the passenger compartment form along the side windows and at the dashboard. Vortices in the flow around the vehicle body form at the side mirrors and the rear of the side windows.

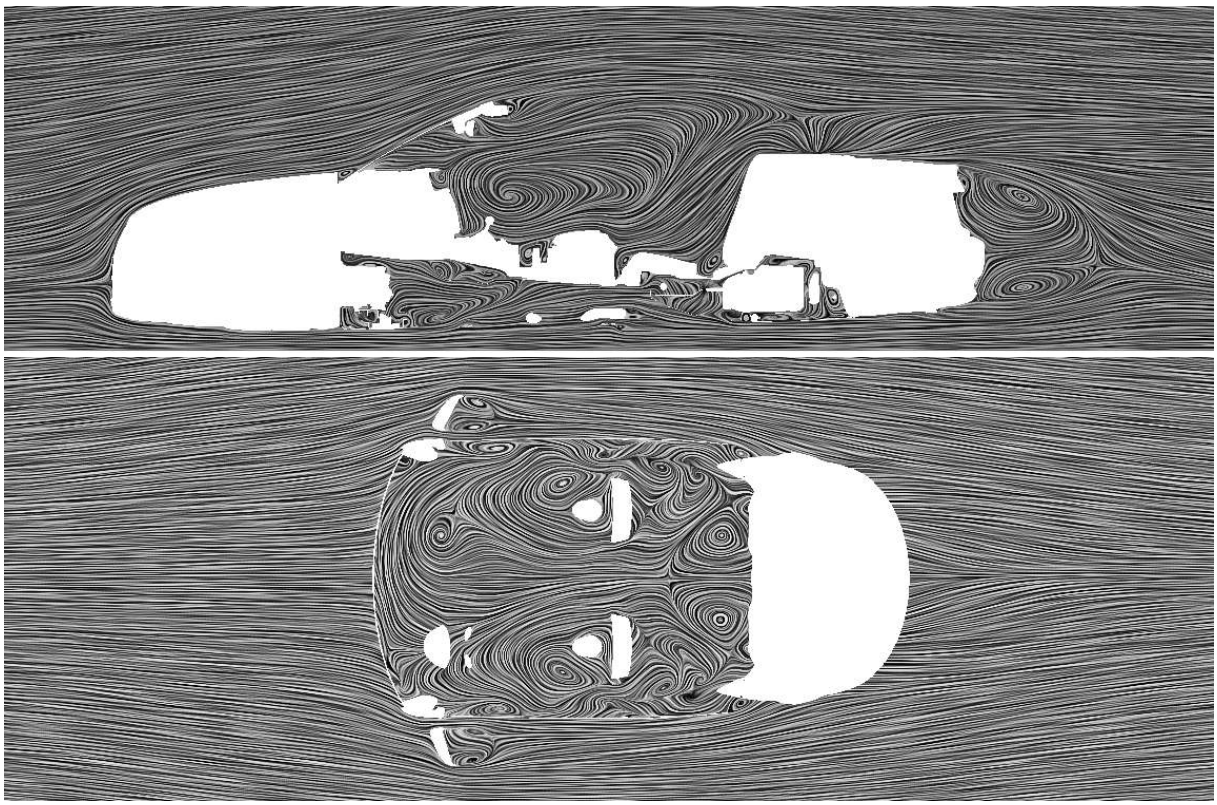

Figure 3.59: Line Integral Convolution (LIC) of the time averaged velocity in the flow around the convertible car model. Top: $y = 0$ plane, bottom: $z = const.$ plane at the height of the faces of the anthropomorphic dummies.

Isosurfaces of the magnitudes of the Shear Maximizing Decomposition tensors are shown in Fig. 3.60, 3.61 and 3.62. The isosurface of $||(\nabla U)_{RR}||$ in Fig. 3.60 shows that the A-pillar vortices split in two branches. One branch follows the top edge of the side windows while the second branch is convected inwards. A pair of inward rotating vortices can be found at the rear edges of the side windows. The pair of recirculation vortices in the rear passenger compartment, already identified in the LIC pictures of the time averaged velocity, are also clearly visible. From the rear of the passenger compartment, two longitudinal vortices extend into the wake of the car model. No strong C-pillar vortices are present in the flow.

In Fig. 3.61 the irrotational deflection of the flow is shown. A strong irrotational deflection of the main flow around the geometry is shown at the front of the car, on the whole windshield and the beginning of the main shear layer at the top edge of the windshield. The two branches of the A-pillar vortices also show an irrotational vortical motion. A contribution to the elongation is also found at the rear edges of the side windows. The two longitudinal vortices, starting at the rear of the passenger compartment, contribute in the vicinity of the geometry and in the space between the vortices only.

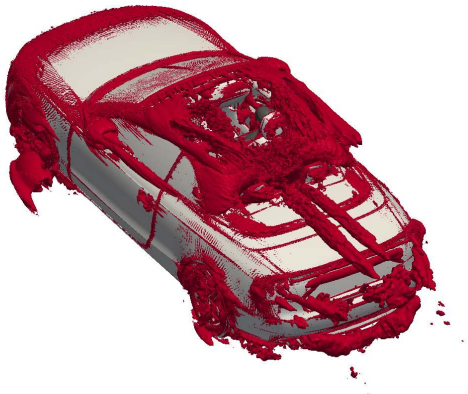

Figure 3.60: Isosurface of the magnitude of the rotation rate tensor from the Shear Maximizing Decomposition, $||(\nabla U)_{RR}|| = 20\,s^{-1}$.

Figure 3.61: Isosurface of the magnitude of the elongation rate tensor from the Shear Maximizing Decomposition, $||(\nabla U)_{EL}|| = 30\,s^{-1}$.

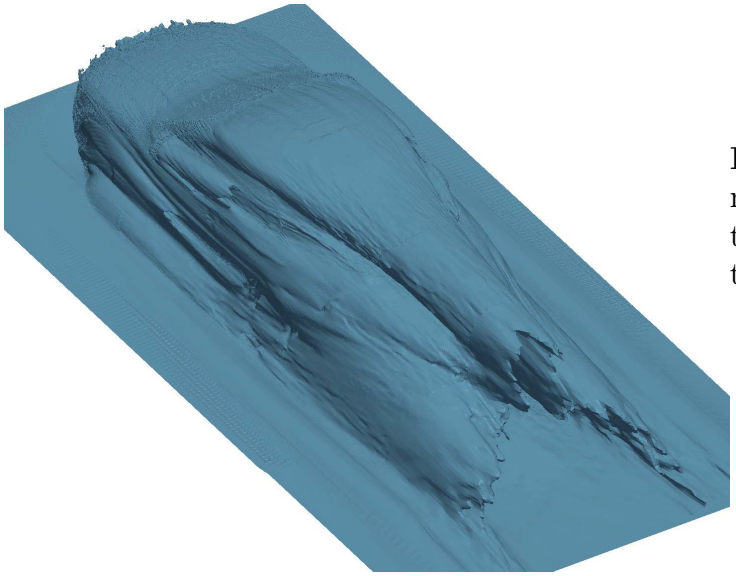

Figure 3.62: Isosurface of the magnitude of the shear rate tensor from the Shear Maximizing Decomposition, $||(\nabla U)_{SH}|| = 50\,s^{-1}$.

The shearing motion in the flow is shown by isosurfaces of the magnitude of the rate of shear tensor $||(\nabla U)_{SH}||$ in Fig. 3.62. Three large shear layers are visible, the shear layer at the upper edge of the windshield and two tubular shear layers from the back of the car geometry. The shear layer of the windshield rolls up at its edges to one tubular structure. Below this shear layer, the shear layers of the car body form as two tubes, comparable to the shear layer in the near wake of the DrivAer car body (Fig. 3.42). Compared with the flow around the DrivAer car body, the downwash behind the car is considerably weaker, here. Other, smaller shear layers develop at the front wheels and the side mirrors.

Unsteady Flow

The unsteady fluctuations of the flow in the passenger compartment of the convertible car model are investigated and linked to force fluctuations on the surface of the anthropomorphic dummies. A weak, low frequency fluctuation of aprrox. $1\,Hz$, found in preceding wind tunnel tests, is investigated with the Dynamic Mode Decomposition of the velocity vector field and the vector field of forces on the geometry.

Dynamic Mode Decomposition The DMD is executed with $N_{DMD} = 800$ time steps, a time step length of $\Delta t_{DMD} = 0.01\,s$ and a total time span of $T_{DMD} = 8\,s$. As in the previous test cases, the time step data is filtered with a 4th order low-pass filter with a ratio of cut-off frequency to Nyquist frequency of 0.1. After the singular value decomposition in the DMD algorithm, the projection basis is restricted to modes with a relative contribution of more than $1 \times 10^{-4}\,\%$ to the total variance of the flow. Prior to the analysis, the fields of forces and velocities are scaled independently to unit variance.

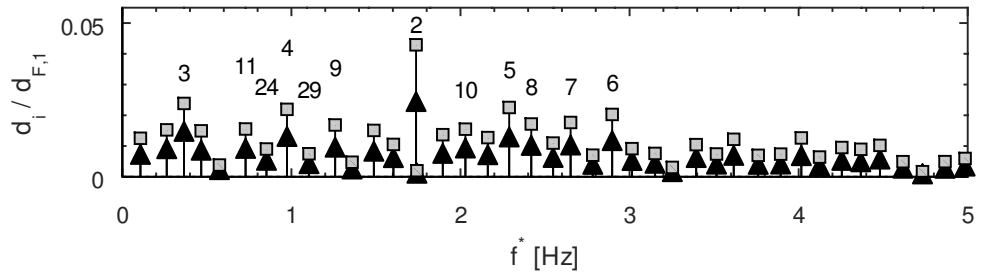

Figure 3.63: Relative amplitude over full scale frequency. Spatially weighted amplitudes of the dynamic modes normalized by amplitude of the first mode of forces on the surface. Squares: velocity, triangles: force.

The spectrum of the relative mode amplitudes for frequencies up to $5\,Hz$ is shown in Fig. 3.63. The dominant oscillations are described by mode 2 with a frequency of $1.74\,Hz$ and mode 3 with a frequency of $0.36\,Hz$. Fluctuations around $1\,Hz$ are described by

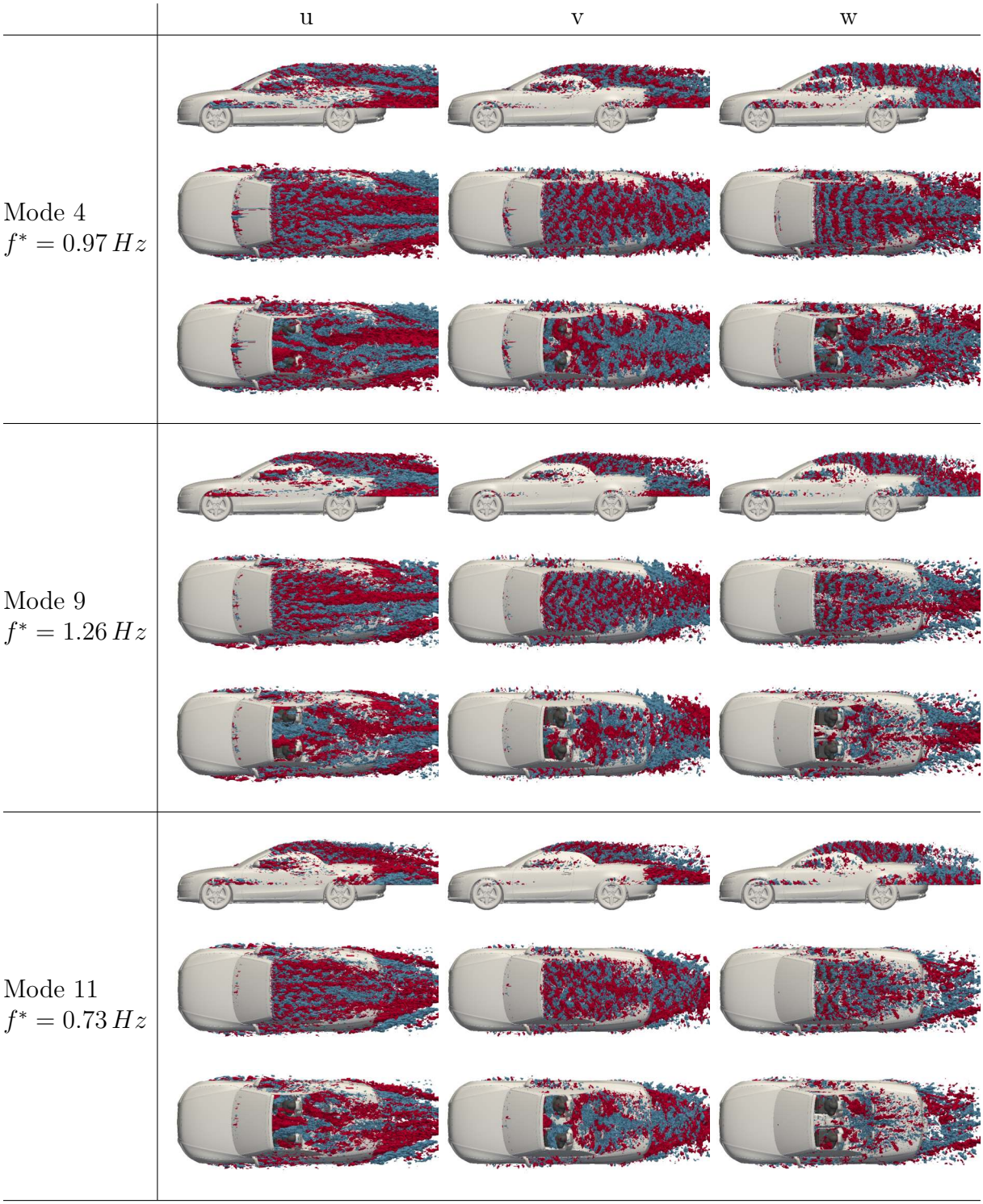

Figure 3.64: Individual DMD Modes 4, 9 and 11. Positive (red) and negative (blue) isosurfaces of the velocity components $u = v = w = \pm 1\,m/s$.

modes 4, 9, 11, 24 and 29. These five modes represent the fluctuations found in the passenger compartment in preceding wind tunnel tests.

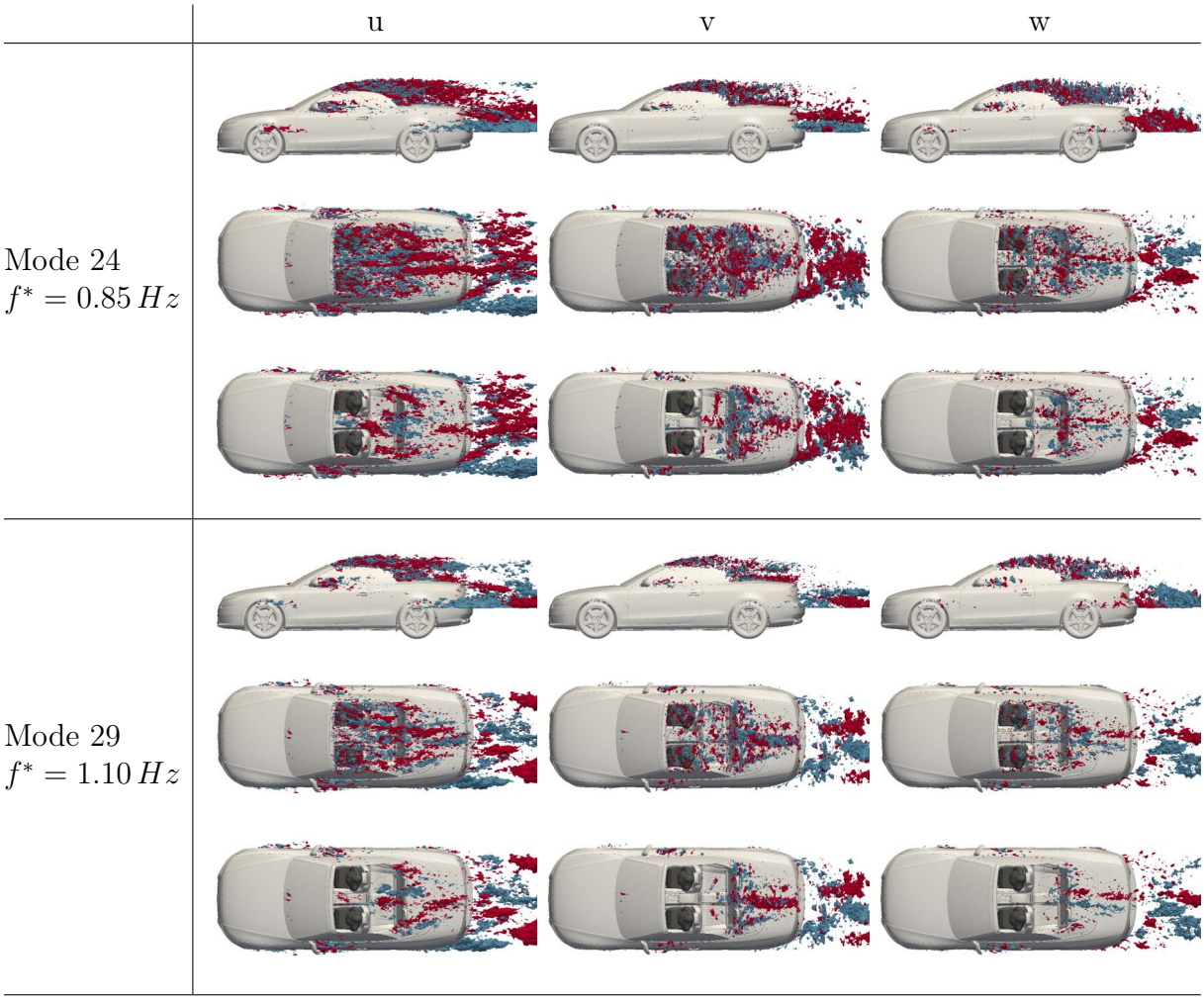

Figure 3.65: Individual DMD Modes 24 and 29. Positive (red) and negative (blue) isosurfaces of the velocity components $u = v = w = \pm 1\,m/s$.

Isosurfaces of the velocity components of the individual modes are shown in Fig. 3.64 and 3.65. The upper picture in the rows is the side view of the geometry, the middle picture the top view and the lower picture shows a top view of the isosurfaces were the shear layer of the windshield is clipped to allow for a visualization of the flow in the passenger compartment. The dominant mode of the chosen modes is mode 4 with a frequency of $0.97\,Hz$. The side view of the model (top pictures in row) as well as the top view (middle pictures in row) show small scale fluctuations in the shear layer of the windshield and large scale fluctuations in the near wake of the model. In the top view with clipped shear layer (bottom picture in row), the large scale fluctuations of the wake can be seen to reach over the rear of the car into the passenger compartment. The same phenomenon can be found in the isosurface pictures of modes 9 and 11. The contribution of modes 24 and 29 to the fluctuations in the passenger compartment are already very weak. The fluctuations

in these modes are mainly restricted to the shear layer of the windshield and the near wake of the car geometry.

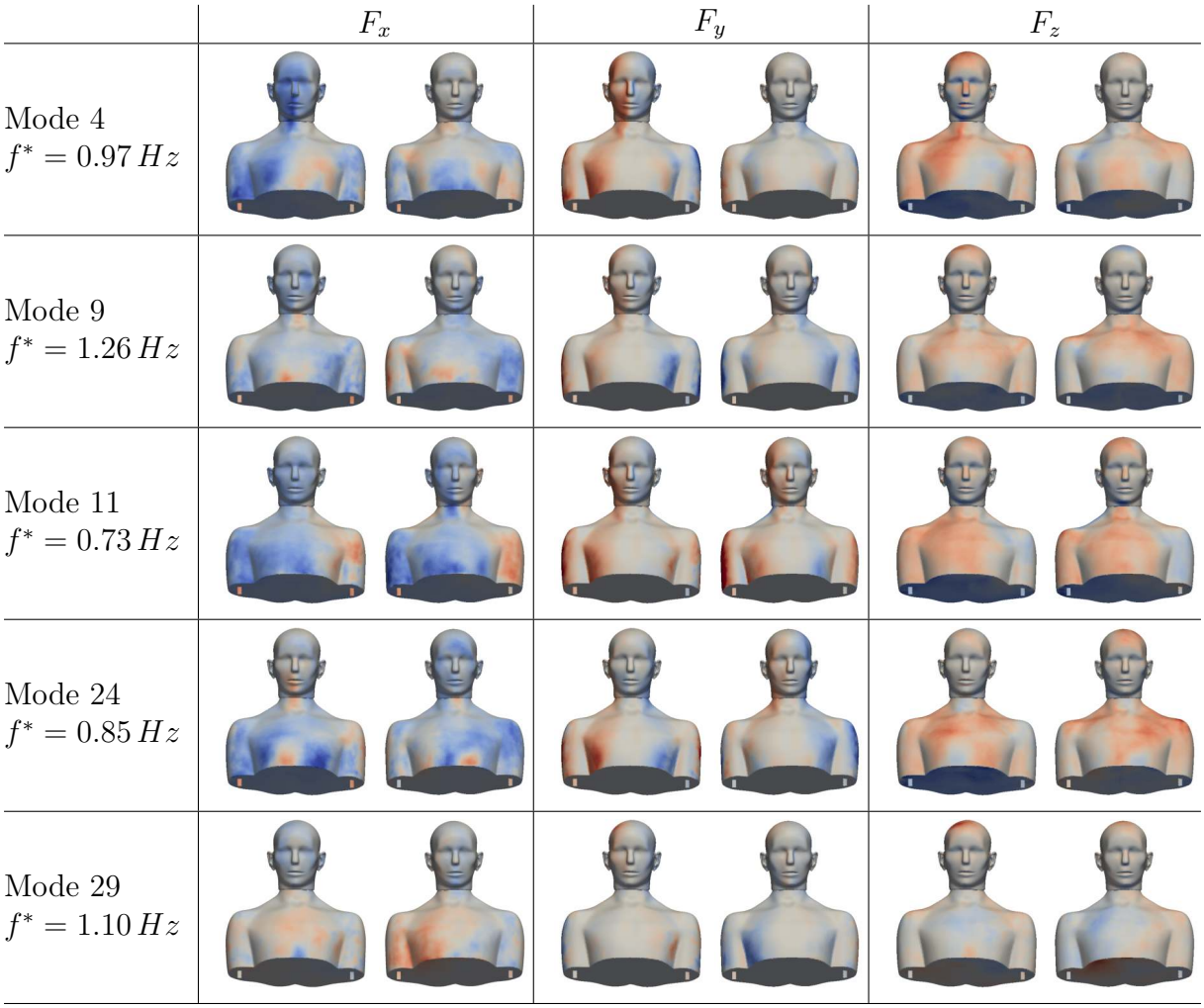

Figure 3.66: Individual DMD Modes 4, 9, 11, 24 and 29. Normalized force $(F_i/A)/(p_\infty + \frac{\rho}{2}U_\infty^2)$ values ranging from $-7 \cdot 10^{-4}$ (blue) to $+7 \cdot 10^{-4}$ (red) for mode 4, $-5 \cdot 10^{-4}$ (blue) to $+5 \cdot 10^{-4}$ (red) for modes 9 and 11 and $-3 \cdot 10^{-4}$ (blue) to $+3 \cdot 10^{-4}$ (red) for modes 24 and 29. Left: co-driver dummy, right: driver dummy.

The force components of the individual modes are shown in Fig. 3.66. In mode 4, the force level is weaker on the driver side dummy (right picture). On the co-driver side dummy, the force fluctuation is concentrated on the left side (window side) of the dummy geometry. The force fluctuations of modes 9, 11 and 24 are similar on the driver and co-driver side dummies respectively. The side force component F_y of modes 9 and 24 is negative on both arms of the driver side dummy but positive on the window side arm of the co-driver dummy. In mode 11, the side force is positive on both sides of the co-driver and negative on the window side of the chest of the driver side dummy. The force fluctuations of mode 29 are comparatively weak.

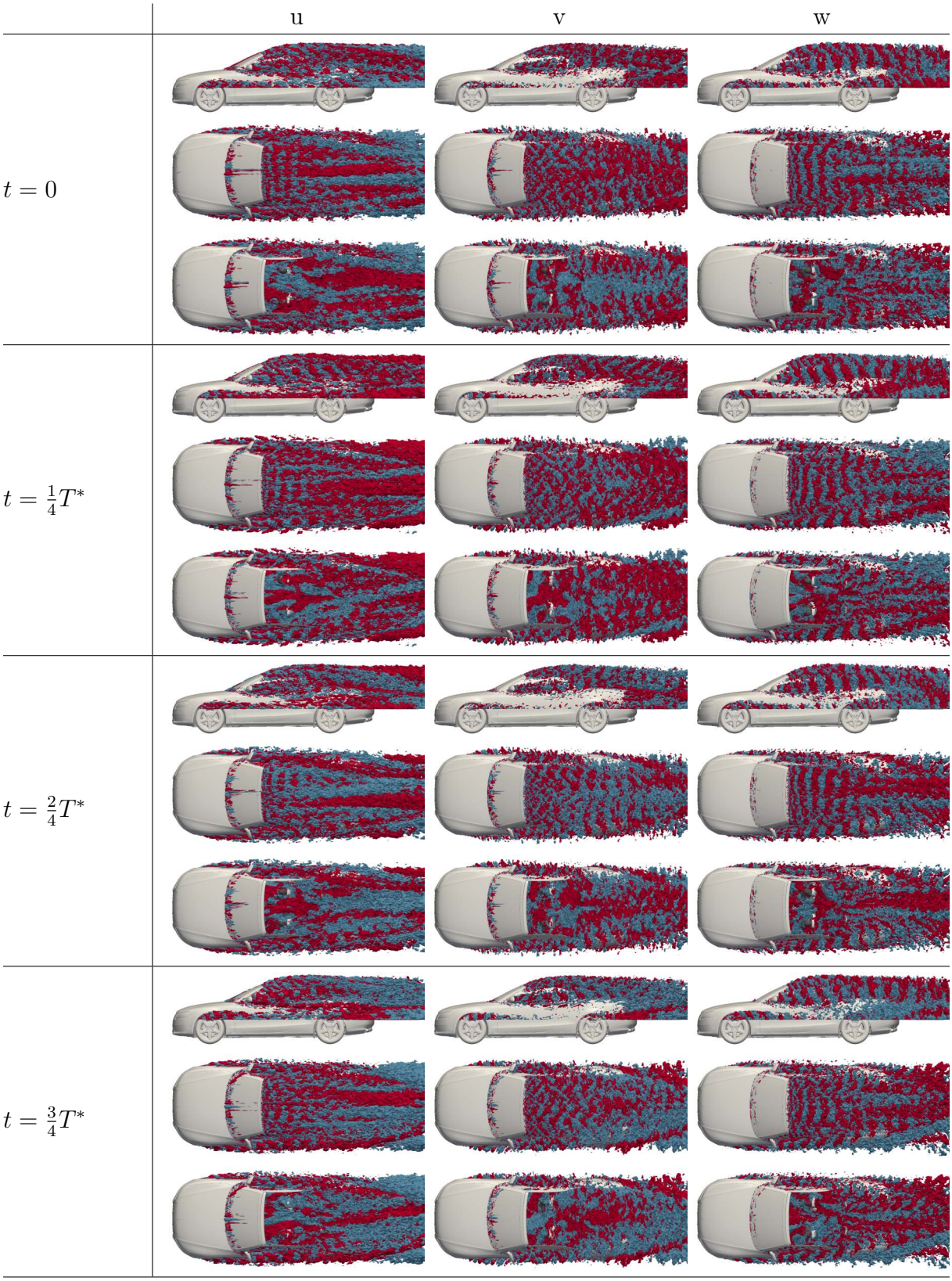

Figure 3.67: Reconstruction of $T^* = 1.03\,s$ (one period of mode 4) with the modes 4, 9, 11, 24 and 29. Positive (red) and negative (blue) isosurfaces of the velocity components $u = v = w = \pm 1\,m/s$.

The flow is reconstructed with the five selected modes. Isosurfaces of the velocity components of a period of $T^* = 1.03\,s$ (one period of mode 4) are shown in Fig. 3.67. Here, small scale structures can be found in the shear layers of the windshield and the side mirrors for all three velocity components. The large scale structures of the near wake, previously found in the individual modes, are most pronounced in the streamwise velocity component u. Two counter oscillating regions can be found at the center line of the model. Most clearly visible in middle picture at $t = \frac{2}{4}T^*$ with a positive motion (red) and a negative motion (blue). These two structures reach far into the passenger compartment and appear to induce a fluid motion in front of the anthropomorphic dummies. Other longitudinal structures extend from the side mirrors into the wake of the car model. No clear longitudinal structures can be found in the spanwise velocity component v. Here, the small scale fluctuations dominate the flow. A larger coherent motion can be found behind the car geometry, were the whole flow is in a spanwise oscillating motion. The small scale fluctuations also dominate the upward velocity component w. The longitudinal structures found here correspond to the structures found in the streamwise component u and describe the upward oscillation of the larger structures.

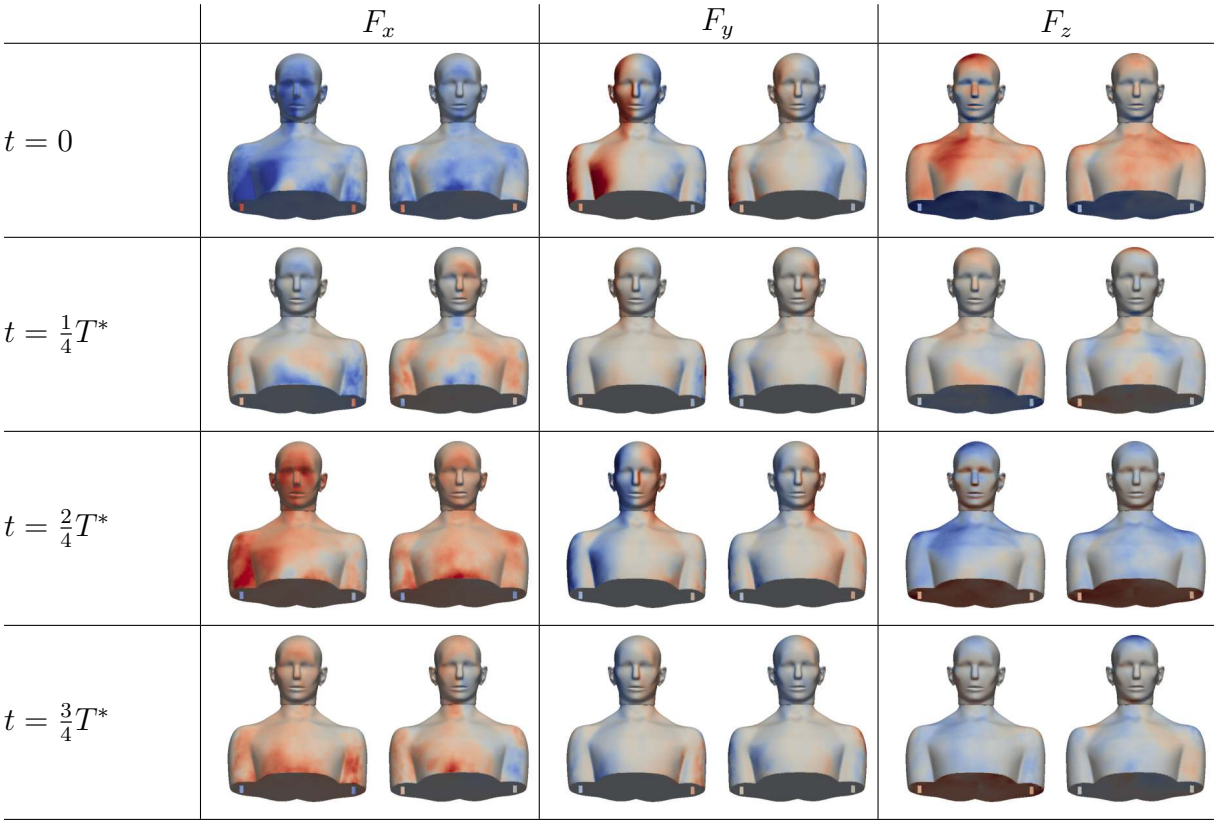

Figure 3.68: Reconstruction of $T^* = 1.03\,s$ (one period of mode 4) with the modes 4, 9, 11, 24 and 29. Normalized force $(F_i/A)/(p_\infty + \frac{\rho}{2}U_\infty^2)$ values ranging from -10^{-3} (blue) to $+10^{-3}$ (red). Left: co-driver dummy, right: driver dummy.

The force components on the anthropomorphic dummies are shown in Fig. 3.68. The maximum amplitude of the streamwise force component F_x is weaker on the driver side dummy. The highest force amplitudes on the driver side dummy can be found on the lower chest. The highest amplitude on the co-driver side are on the window side of the chest, the arm and in the face. Apart from different regions of maximum force, the pattern of streamwise force is similar on the two dummies. The sideward force component F_y oscillates with a phase shift of half a period on both sides of the dummies with lower amplitudes on the driver side dummy geometry. The highest amplitudes of the upward force component F_z can be found on the top of the heads and on the shoulders of the dummy geometries. Again, the amplitudes on the driver side dummy are lower. A phase shift of approx. a quarter period between the oscillation of F_z on the heads of the dummies is present.

3.4.3 Conclusion

The time averaged and unsteady flow around a car geometry of convertible type was investigated in this test case. The time averaged flow was analyzed with Line Integral Convolutions of the time averaged wall shear stress and time averaged velocity fields. The topology of the time averaged flow was documented with a Shear Maximizing Decomposition of the velocity gradient tensor field.

The unsteady flow was investigated with a Dynamic Mode Decomposition of the velocity field and the field of forces on the surface of the geometry for frequencies below $5\,Hz$. A force fluctuation on the anthropomorphic dummies of approx. $1\,Hz$, previously found in wind tunnel tests, could be retraced with the simulation and investigated in detail. The fluctuations with frequency of approx. $1\,Hz$ were represented by the DMD with 5 different modes. The modes were investigated separately and reconstructed together for the velocity and the force field. The velocity fields show strong vortex shedding at the top of the windshield at the investigated frequencies around $1\,Hz$. The lengthscale of the vortex shedding indicates that the shedding is not induced by the local flow. It is assumed that the shedding process is triggered by large scale fluctuations in the near wake of the car with a much larger lengthscale. These larger structures were found to reach into the passenger compartment and are responsible for the oscillating flow around, and the force fluctuation on the anthropomorphic dummies. As high energy fluctuations of $1\,Hz$ frequency from the top of the windshield will also have a driving effect on the fluctuations in the passenger compartment, the entire process can be described as a feedback loop. Large scale fluctuations are induced in the near wake, the oscillation triggers the shedding process of high energy at the top of the windshield, the vortices are convected into the wake and influence the large scale fluctuations. Both processes drive the fluctuations in the passenger compartment.

4 Conclusion

This thesis investigated the applicability of selected methods to the analysis of coherent structures in unsteady car aerodynamics. The approach of the thesis was to rely on extensive investigations of the unsteady flow to identify and isolate its underlying mechanisms. In contrast to variation studies, where transferable mechanisms are searched for by reducing the complexity of the geometry, this approach allows for investigations of arbitrarily complex geometries. A thorough theoretical assessment of selected vortex identification schemes as well as an assessment of two modal decompositions was executed. The methods were applied to test cases with different degree of geometry complexity and were analyzed for their applicability in the car aerodynamics development process.

Vortex identification schemes were assessed in chapter 2.4 for their applicability in car aerodynamics. The most common vortex detection methods; Q-criterion, Δ-criterion, λ_2-criterion and λ_{ci}-criterion as well as the less well known Shear Maximizing Decomposition of the velocity gradient tensor (also called the Triple Decomposition of Motion) were tested on simple, canonical flow examples. By applying the Q, Δ, λ_2 and λ_{ci}-criterion onto the tensor fields of the Shear Maximizing Decomposition, the behavior of the vortex detection methods applied to car aerodynamics flow fields was investigated.

It was shown that none of the investigated vortex criteria can be used for quantitative investigations of vortices and all criteria can even fail completely in some special cases. The Q, Δ, λ_2 and λ_{ci}-criterion as well as the magnitude of the rate of rotation tensor $||(\nabla U)_{RR}||$ from the Shear Maximizing Decomposition only show the core region of Rankine type vortices. The outer parts of vortices with an increasing amount of simple shear rate and rate of irrotational straining are strongly underpredicted or not shown by the criteria. Nonetheless, vortex criteria are used with success in a large number of fluid mechanics and car aerodynamics projects. The reason for the success of vortex criteria, despite their shortcomings, is their ability to visualize the topology of the flow rather than extracting and quantifying individual vortices. With this in mind, the Shear Maximizing Decomposition (SMD) appears to be the most useful of the investigated methods. The SMD decomposes the flow and retains the full information of the velocity gradient tensor. By using all three result tensors of the SMD, the topology of the flow can be analyzed without the restriction to the inner core region of vortices. The SMD allows for a description of the flow topology based on relative motions in general rather than on vortical motions only.

The Proper Orthogonal Decomposition (POD) and Dynamic Mode Decomposition (DMD) were discussed in chapter 2.5. It was pointed out that the proper orthogonal modes of the POD are sign indeterminate. An algorithm for a reconstruction of the sign information was found in literature and was briefly introduced. The reconstruction of the sign information was found to be computationally expensive when compared to the computation of the Singular Value Decomposition. Considering the computational resources needed for the unsteady CFD simulations, the resource requirements of the POD with sign correction is still acceptable.

For the Dynamic Mode Decomposition, pre and post-processing procedures were proposed. It was found that the standard Dynamic Mode Decomposition with the filtering step based on the Singular Value Decomposition as proposed in [92] is not applicable in most car aerodynamics applications without a pre-filtering of the flow field data. The filtering based on the Singular Value Decomposition in the standard DMD assumes a relation between the total variance and the time scale of fluctuations. In the velocity field around simple objects, high frequency oscillations generally have low total variance and can be filtered out by the Singular Value Decomposition in the DMD algorithm. In the flow around complex geometries as the geometries of car aerodynamics, high frequency oscillations with high total variance can be present in the velocity field. An example for the production of high energy and high frequency fluctuations would be the vortex shedding from the side mirrors of a car. The fluctuations from the side mirrors have higher kinetic energy (and therefore higher total variance) than other fluctuations around the car with considerably lower frequency. In a standard DMD, the fluctuations of high total variance from the side mirrors would have to be resolved with a sufficiently small time step length of the DMD, or the fluctuations from the side mirrors as well as all fluctuations with lower kinetic energy

would have to be filtered out by the Singular Value Decomposition. Due to memory restrictions, resolving the high frequencies is usually not possible when investigating low frequency oscillations. Filtering the high energy high frequency oscillations would discard most of the information in the DMD. The same problem arises when processing fields with no or weak relation between total variance and time scale as vorticity fields or force fields. Here, the filtering based on the Singular Value Decomposition is also not able to remove high frequency fluctuations from the flow field data. To avoid the described problems, the flow field data is filtered with a low-pass filter prior to the DMD analysis. The low-pass filter removes all fluctuations that cannot be resolved by the DMD independent of total variance. It was found that a combination of a low-pass filtering prior to the DMD and a very moderate filtering with the Singular Value Decomposition in the DMD produces the best results. The SVD filter accounts for a rank deficiency in the snapshot matrix and removes noise due to numerical errors. The threshold for the SVD filtering can be universally set to a very low value and the cut-off frequency of the low-pass filter can be determined by the time step length of the DMD. This allows for an execution of the DMD without user specified parameters.

Comparing the Proper Orthogonal Decomposition with the Dynamic Mode Decomposition, the DMD was found to be superior for investigations of coherent structures in car aerodynamics. In the DMD, an unsteady flow phenomenon like a vortex shedding process is represented typically with one complex mode. In the POD, the same flow phenomenon is typically represented by several modes. To reconstruct the flow phenomenon, the correct modes have to be found and reconstructed together. As the Proper Orthogonal Modes typically consist of more than one flow phenomenon, the reconstruction will still not be as clear as the reconstruction of the DMD in most cases. Another disadvantage of the POD is the sign indifference of the modes. Although an estimation of the sign is possible, computing the POD with sign estimation for a reasonable number of modes is more expensive than the computation of the DMD. The DMD is especially advantageous for investigations based on the frequency of a fluctuation. In this case, the related coherent structures can usually easily be isolated.

The vortex detection methods and modal decompositions were applied to test cases with different degree of geometry complexity and realism. To allow for a fast execution, all methods were implemented for distributed memory parallel execution. As a basis for the unsteady investigations, the time averaged flow of each test case was investigated and the dominant coherent structures of the time averaged flows were described in detail. Subsequently, the modal decompositions were applied to the unsteady flows.

To allow for a comparison of the results of the methods to results already present in the literature, a cube mounted on the surface of a channel was investigated as a first test case. The flow structures of the time averaged flow, described by Line Integral Convolution pictures, matched the structures described in the literature. The results of the

Shear Maximizing Decomposition also reproduced the published structures and provided additional insight into the topology of the flow. The dominant Proper Orthogonal modes were also found to match the modes from POD results in the literature. With the sign estimation, additional information about the modes could be acquired. A comparison of the modes from the POD with the modes of the DMD found strong similarities for the dominant modes. The DMD was found to be able to extract distinct unsteady flow processes like a vortex shedding or an oscillation of a horse shoe vortex. In addition to the DMD on velocity vector fields, the DMD was applied to the fields of the magnitudes of the SMD tensors. These investigations would not have been possible without the described pre-filtering of the data.

As a second test case, the methods were applied to four configurations of the SAE body. A closed notchback and a closed estate configuration as well as the notchback and estate configurations with a highly simplified, generic engine compartment. Here, the field of static pressure and the velocity vector field were processed in one DMD analysis to visualize the connections between the flow variables in the unsteady flow. In this analysis, a strong vortex shedding in the frequency of the wake oscillation from the struts of the model was found. As the struts were too thin to produce a low frequency, high energy fluctuation solely by the instability of the local flow, the fluctuation was interpreted to be induced by oscillations of the whole flow around the car caused by the strong wake oscillation.

The flow around the DrivAer body, as an example of a realistic generic vehicle, was investigated as a third test case. In this case, the DMD was applied to the velocity vector field in the volume around the car and on the force vector field on the surface of the car in one analysis. This approach allows establishing a connection between the unsteady coherent structures in the flow and the unsteady forces acting on the car. By computing the force and moment coefficients of the dominant dynamic modes, the main source of flow induced car body oscillations could be identified. The flow fields of the respective modes provide the connection of car body oscillations to the unsteady coherent structures in the flow. In addition, the motion of a vortex system and the shedding of vortices from the near wake of the car were described in detail and compared to a description of a vortex shedding process from the near wake of a car of similar geometry in literature. Again, it was found that structures with relatively small length scale contributed to modes with relatively long time scale.

As an example of a detailed vehicle geometry, the flow around an open roof convertible type car model based on a state of production vehicle was investigated. Two anthropomorphic dummies were included in the car geometry to investigate the effect of flow oscillations on ride comfort of the driver and co-driver. The unsteady flow in this test case was, again, investigated with a DMD of the velocity vector field in the volume around the car and the force vector field on the surface of the car in one analysis. A low frequency

fluctuation of approx. 1 Hz, previously found in wind tunnel experiments, could be reproduced and explained by the DMD results. The oscillating flow structure in the passenger compartment, responsible for a force fluctuation on the anthropomorphic dummies, was found to reach into the wake flow of the car. A strong contribution of the shear layer oscillation from the top of the windshield to the mode of the oscillation in the passenger compartment pointed to a driving effect of the shear layer oscillation to the fluctuation in the passenger compartment. As the time scale of the fluctuation is larger than the typical time scale of the fluctuations induced by the shear layer of the windshield, the oscillation is interpreted to be induced by an oscillation in the wake of the car. The wake oscillation provokes an oscillation of the whole flow around the car and causes the oscillation of the windshield shear layer. As the flow from the windshield shear layer is convected into the wake, a feedback loop is established. Based on this interpretation, a stabilization of the flow in the passenger compartment would be possible with a geometry modification at the top of the windshield, to influence the shear layer, with a wind screen to disconnect the flow in the passenger compartment from the wake flow or with a measure to suppress the fluctuation of the wake.

Future Work

The concept of *coherent structures* as a method to structure, characterize and interpret the flow has a long history in bluff body and car aerodynamics. The concept is most useful to develop an understanding of the topology of a complex flow and to make predictions of how a change in the geometry could affect the flow and its forces on the geometry. Nonetheless, there are drawbacks to this concept for unsteady aerodynamics. As the coherent structures are part of the flow (rather than objects in the flow) and are defined by their spacial and temporal velocity distribution, they are inherently dependent on a reference system. Visualizing a coherent structure in a different reference system can considerably change its interpretation. An objective and commonly accepted definition of coherent structures is yet to be found.

The Dynamic Mode Decomposition with its ability to isolate unsteady coherent structures was shown to be of great value in the investigation of the unsteady flow around complex car geometries. However, there are some open questions: The parameters of the DMD such as time step length, number of time steps in the analysis or the total time span of the investigation have an influence on the accuracy of the decomposition. A thorough investigation of the error in the analysis and its dependency on the parameters of the DMD is not yet available for complex use cases. It has also been noted that the result of the decomposition can be sensitive to small changes of the input data in some cases. A small change of input data can cause flow processes to be represented by nearby modes. This effect can considerably change the mode spectrum in its current form.

While the DMD was shown to be of great value in the investigation of practical engineering problems, it also has a large potential to be used in exploratory analysis of flow field data. A challenge in the exploratory analysis of flow fields, using the DMD, is to choose the important DMD modes. Here, a more sophisticated definition of the modes amplitudes is necessary.

As the Dynamic Mode Decomposition has gained a considerable amount of attention in the fluid dynamics research community, a number of variants to the original DMD algorithm proposed by Schmid in [92] can be found in literature, addressing the resource requirements of the original DMD algorithm. A recent overview of the most popular variants is given in Dawson et al. [24].

5 Bibliography

[1] S. Ahmed, G. Ramm, and G. Faitin. Some salient features of the time-averaged ground vehicle wake. *SAE Technical Paper*, 840300, 1984.

[2] Giancarlo Alfonsi, Carlo Restano, and Leonardo Primavera. Coherent structures of the flow around a surface-mounted cubic obstacle in turbulent channel flow. *Journal of Wind Engineering and Industrial Aerodynamics*, 91(4):495 – 511, 2003.

[3] G. A. Ashford. *An Unstructured Grid Generation and Adaptive Solution Technique for High-Reynolds-Number Compressible Flows*. PhD thesis, University of Michigan, 1996.

[4] Nadine Aubry, Philip Holmes, John L. Lumley, and Emily Stone. The dynamics of coherent structures in the wall region of a turbulent boundary layer. *Journal of Fluid Mechanics*, 192:115–173, 7 1988.

[5] C. J. Barnes, M. R. Visbal, and P. G. Huang. On the effects of vertical offset and core structure in streamwise-oriented vortex–wing interactions. *Journal of Fluid Mechanics*, 799:128–158, 7 2016.

[6] G. K. Batchelor. *An Introduction to Fluid Dynamics*. Cambridge University Press, 2000.

[7] Dirk Bäder. *Aerodynamische Optimierung der Kühlluftdurchströmung von Kraftfahrzeugen*. PhD thesis, TU München, 2012.

[8] L. S. Blackford, J. Choi, A. Cleary, E. D'Azevedo, J. Demmel, I. Dhillon, J. Dongarra, S. Hammarling, G. Henry, A. Petitet, K. Stanley, D. Walker, and R. C. Whaley. *ScaLAPACK Users' Guide*. Society for Industrial and Applied Mathematics, Philadelphia, PA, 1997.

[9] S. Bonitz, L. Larsson, L. Lofdahl, and A. Broniewicz. Structures of flow separation on a passenger car. *SAE Int. J. Passeng. Cars - Mech. Syst.*, 8(1):177–185, 2015.

[10] J. P. Bonnet, J. Delville, M. N. Glauser, R. A. Antonia, D. K. Bisset, D. R. Cole, H. E. Fiedler, J. H. Garem, D. Hilberg, J. Jeong, N. K. R. Kevlahan, L. S. Ukeiley, and E. Vincendeau. Collaborative testing of eddy structure identification methods in free turbulent shear flows. *Experiments in Fluids*, 25:197–225, 1998.

[11] R. Bro, E. Acar, and Tamara G. Kolda. Resolving the sign ambiguity in the singular value decomposition. *Journal of Chemometrics*, 22(2):135–140, 2008.

[12] I. P. Castro and A. G. Robins. The flow around a surface-mounted cube in uniform and turbulent streams. *Journal of Fluid Mechanics*, 79:307–335, 2 1977.

[13] P. Chakraborty, S Balachandar, and R. J. Adrian. On the relationships between local vortex identification schemes. *Journal of Fluid Mechanics*, 535(-1):189–214, 2005.

[14] Y. M. Chen, Z. Li, and F. He. Evaluation of vortex criteria using triple decomposition and quadruple decomposition of motion. *AIP Conference Proceedings*, 1376(1):635–638, 2011.

[15] S. Y. Cheng, M. Tsubokura, T. Nakashima, T. Nouzawa, and Y. Okada. A numerical analysis of transient flow past road vehicles subjected to pitching oscillation. *Journal of Wind Engineering and Industrial Aerodynamics*, 99(5):511 – 522, 2011.

[16] S. Y. Cheng, M. Tsubokura, T. Nakashima, Y. Okada, and T. Nouzawa. Numerical quantification of aerodynamic damping on pitching of vehicle-inspired bluff body. *Journal of Fluids and Structures*, 30(0):188 – 204, 2012.

[17] S. Y. Cheng, M. Tsubokura, Y. Okada, T. Nouzawa, T. Nakashima, and D. H. Doh. Aerodynamic stability of road vehicles in dynamic pitching motion. *Journal of Wind Engineering and Industrial Aerodynamics*, 122:146 – 156, 2013. The Seventh International Colloquium on Bluff Body Aerodynamics and Applications (BBAA7).

[18] M. S. Chong, A. E. Perry, and B. J. Cantwell. A general classification of three-dimensional flow fields. *Physics of Fluids A: Fluid Dynamics (1989-1993)*, 2(5):765–777, 1990.

[19] A. Cogotti. A parametric study on the ground effect of a simplified car model. *SAE Technical Paper*, 980031, 1998.

[20] R. Courant, K. Friedrichs, and H. Lewy. Über die partiellen Differenzengleichungen der mathematischen Physik. *Mathematische Annalen*, 100:32–74, 1928.

[21] Emma Croner, Hervé Bézard, Christophe Sicot, and Guillaume Mothay. Aerodynamic characterization of the wake of an isolated rolling wheel. *International Journal of Heat and Fluid Flow*, 43:233 – 243, 2013.

[22] R. Cucitore, M. Quadrio, and A. Baron. On the effectiveness and limitations of local criteria for the identification of a vortex. *European Journal of Mechanics - B/Fluids*, 18(2):261 – 282, 1999.

[23] Lars Davidson. Large eddy simulation: A dynamic one-equation subgrid model for three-dimensional recirculating flow. *11th Int. Symp. on Turbulent Shear Flow, Grenoble*, 1997.

[24] S. T. M. Dawson, M. S. Hemati, M. O. Williams, and C. W. Rowley. Characterizing and correcting for the effect of sensor noise in the dynamic mode decomposition. *Experiments in Fluids*, 57(3), 2016.

[25] E. de Villiers. *The Potential of Large Eddy Simulation for the Modeling of Wall Bounded Flows*. PhD thesis, Imperial College of Science, Technology and Medicine, London, 2006.

[26] D. Duke, J. Soria, and D. Honnery. An error analysis of the dynamic mode decomposition. *Experiments in Fluids*, 52:529–542, 2012. 10.1007/s00348-011-1235-7.

[27] R. Elavarasan and Hui Meng. Flow visualization study of role of coherent structures in a tab wake. *Fluid Dynamics Research*, 27(3):183 – 197, 2000.

[28] Joel H. Ferziger and Milovan Peric. *Numerische Strömungsmechanik*. Springer, 2008.

[29] Michael Frewer. More clarity on the concept of material frame-indifference in classical continuum mechanics. *Acta Mechanica*, 202(1):213–246, 2008.

[30] Joshua Fuller and Martin A. Passmore. The importance of rear pillar geometry on fastback wake structures. *Journal of Wind Engineering and Industrial Aerodynamics*, 125:111 – 120, 2014.

[31] Michael Gestrich. Hybride RANS/LES - Methoden in der Fahrzeugaerodynamik. Master's thesis, Technische Universität München, 2014.

[32] B. Gilhome, J. Saunders, and J. Sheridan. Time averaged and unsteady near-wake analysis of cars. *SAE Technical Papers*, 2001-01-1040, 2001.

[33] Patrick Gilliéron, Annie Leroy, Sandrine Aubrun, and Pierre Audier. Influence of the slant angle of 3d bluff bodies on longitudinal vortex formation. *Journal of Fluids Engineering*, 132, 2010.

[34] Aswin Gnanaskandan and Krishnan Mahesh. Numerical investigation of near-wake characteristics of cavitating flow over a circular cylinder. *Journal of Fluid Mechanics*, 790:453–491, 3 2016.

[35] Emmanuel Guilmineau. Computational study of flow around a simplified car body. *Journal of Wind Engineering and Industrial Aerodynamics*, 96(6–7):1207 – 1217, 2008.

[36] R. Haimes and D. Kenwright. On the velocity gradient tensor and fluid feature extraction. *AIAA 14th Computational Fluid Dynamics Conference*, 99:3288–3297, 1999.

[37] George Haller. Lagrangian coherent structures. *Annual Review of Fluid Mechanics*, 47(1):137–162, 2015.

[38] A. Heft, T. Indinger, and N. Adams. Introduction of a new realistic generic car model for aerodynamic investigations. *SAE Technical Paper*, 2012-01-0168, 2012.

[39] Angelina Heft. *Aerodynamic Investigation of the Cooling Requirements of Electric Vehicles*. Dissertation, Technische Universität München, München, 2014.

[40] C. Hoarau, J. Borée, J. Laumonier, and Y. Gervais. Unsteady wall pressure field of a model a-pillar conical vortex. *International Journal of Heat and Fluid Flow*, 29(3):812 – 819, 2008. The Fifth International Symposium on Turbulence and Shear Flow Phenomena (TSFP5).

[41] J. C. R. Hunt, C. J. Abell, J. A. Peterka, and H. Woo. Kinematical studies of the flows around free or surface-mounted obstacles; applying topology to flow visualization. *Journal of Fluid Mechanics*, 86:179–200, 5 1978.

[42] J. C. R. Hunt, A. A. Wray, and P. Moin. Eddies, streams, and convergence zones in turbulent flows. *2. Proceedings of the 1988 Summer Program*, 1988.

[43] H. J. Hussein and R. J. Martinuzzi. Energy balance for turbulent flow around a surface mounted cube placed in a channel. *Physics of Fluids*, 8(3):764–780, 1996.

[44] M. Islam, F. Decker, E. de Villiers, A. Jackson, J. Gines, T. Grahs, A. Gitt-Gehrke, and J. Comas i Font. Application of detached-eddy simulation for automotive aerodynamics development. *SAE Technical Paper*, 2009-01-0333, 2009.

[45] R. I. Issa. Solution of the implicitly discretised fluid flow equations by operator-splitting. *Journal of Computational Physics*, 62(1):40 – 65, 1986.

[46] Hrvoje Jasak. *Error analysis and estimation for the finite volume method with applications to fluid flows.* PhD thesis, Imperial College, University of London, 1996.

[47] Jinhee Jeong and Fazle Hussain. On the identification of a vortex. *Journal of Fluid Mechanics*, 285(-1):69–94, 1995.

[48] Fengjian Jiang, Helge I. Andersson, José P. Gallardo, and Valery L. Okulov. On the peculiar structure of a helical wake vortex behind an inclined prolate spheroid. *Journal of Fluid Mechanics*, 801:1–12, 8 2016.

[49] Hongyi Jiang, Liang Cheng, Scott Draper, Hongwei An, and Feifei Tong. Three-dimensional direct numerical simulation of wake transitions of a circular cylinder. *Journal of Fluid Mechanics*, 801:353–391, 8 2016.

[50] Ming Jiang, Raghu Machiraju, and David Thompson. Detection and visualization of vortices. *The Visualization Handbook*, pages 295–309, 2005.

[51] Jeong-Hyun Kim and Yong Oun Han. Experimental investigation of wake structure around an external rear view mirror of a passenger car. *Journal of Wind Engineering and Industrial Aerodynamics*, 99(12):1197 – 1206, 2011.

[52] I. Kohri, T. Yamanashi, T. Nasu, Y. Hashizume, and D. Katoh. Study on the transient behaviour of the vortex structure behind ahmed body. *SAE Int. J. Passeng. Cars - Mech. Syst.*, 7(2):586–602, 2014.

[53] Václav Kolář. 2d velocity-field analysis using triple decomposition of motion. *Proceedings of the Fifteenth Australasian Fluid Mechanics Conference*, 2004.

[54] Václav Kolář. Some basic aspects of the triple decomposition of the relative motion near a point. *16th Australasian Fluid Mechanics Conference (AFMC)*, 2007.

[55] Václav Kolář. Vortex identification: New requirements and limitations. *International Journal of Heat and Fluid Flow*, 28(4):638 – 652, 2007.

[56] Václav Kolář. A note on integral vortex strength. *Journal of Hydrology and Hydromechanics*, 58(1):23–28, March 2010.

[57] Václav Kolář, Jakub Šístek, Fehmi Cirak, and Pavel Moses. Average corotation of line segments near a point and vortex identification. *AIAA Journal*, 51:11:2678–2694, 2013.

[58] Václav Kolár. Compressibility effect in vortex identification. *AIAA Journal*, 47(2):473–475, 2009.

[59] Siniša Krajnović. Large eddy simulation exploration of passive flow control around an ahmed body. *Journal of Fluids Engineering*, 136:10, 2014.

[60] Siniša Krajnović and Lars Davidson. Large-eddy simulation of the flow around a bluff body. *AIAA Journal*, 40(5):927–936, 2002.

[61] Siniša Krajnović and Lars Davidson. Flow around a simplified car, part 1: Large eddy simulation. *Journal of Fluids Engineering*, 127:907–918, 2005.

[62] Siniša Krajnović and Lars Davidson. Flow around a simplified car, part 2: Understanding the flow. *Journal of Fluids Engineering*, 127:919–928, 2005.

[63] A. Larousse, R. Martinuzzi, and C. Tropea. Flow around surface-mounted, three-dimensional obstacles. *Turbulent Shear Flows 8*, pages 127–139, 1993.

[64] Benjamin Levy and Pierre Brancher. Topology and dynamics of the a-pillar vortex. *Physics of Fluids*, 25(3):037102, 2013.

[65] I-Shih Liu and Rubens Sampaio. Remarks on material frame-indifference controversy. *Acta Mechanica*, 225(2):331–348, 2013.

[66] J. L. Lumley. *Stochastic Tools in Turbulence - Applied Mathematics and Mechanics Series : Volume 12*. Academic Press, New York, 1970.

[67] S. Mack, T. Indinger, N. Adams, and P. Unterlechner. The ground simulation upgrade of the large wind tunnel at the technische universität münchen. *SAE Technical Paper*, 2012-01-0299, 2012.

[68] S. Mack, T. Indinger, N. A. Adams, S. Blume, and P. Unterlechner. The interior design of a 40% scaled drivaer body and first experimental results. *ASME 2012 Fluids Engineering Division Summer Meeting*, 2012.

[69] M. Manhart and H. Wengle. A spatiotemporal decomposition of a fully inhomogeneous turbulent flow field. *Theoretical and Computational Fluid Dynamics*, 5:223–242, 1993.

[70] R. Martinuzzi and C. Tropea. The flow around surface-mounted, prismatic obstacles placed in a fully developed channel flow (data bank contribution). *Journal of Fluids Engineering*, 115:85–92, 1993.

[71] S. Menon and W.-W. Kim. High reynolds number flow simulations using the localized dynamic subgrid-scale model. *AIAA 34th Aerospace Sciences Meeting and Exhibit*, 1996.

[72] F. R. Menter. Best practice: Scale-resolving simulations in ansys cfd - version 1.0. Technical report, ANSYS Germany GmbH, 2012.

[73] F. R. Menter and M. Kuntz. Adaptation of eddy-viscosity turbulence models to unsteady separated flow behind vehicles. *The Aerodynamics of Heavy Vehicles: Trucks, Busses and Trains*, 2002.

[74] Tomas Muld, Gunilla Efraimsson, and Dan Henningson. Mode decomposition on surface-mounted cube. *Flow, Turbulence and Combustion*, 88:279–310, 2012. 10.1007/s10494-011-9355-y.

[75] T. Nakashima, M. Tsubokura, T. Nouzawa, and T. Nakamura. Flow structures above the trunk deck of sedan-type vehicles and their influence on high-speed vehicle stability 2nd report: Numerical investigation on simplified vehicle models using large-eddy simulation. *SAE Int. J. Passeng. Cars - Mech. Syst.*, 2(1):157–167, 2009.

[76] Walter Noll. A frame-free formulation of elasticity. *Journal of Elasticity*, 83(3):291–307, 2006.

[77] Y. Okada, T. Nouzawa, T. Nakamura, and S. Okamoto. Flow structures above the trunk deck of sedan-type vehicles and their influence on high-speed vehicle stability 1st report: On-road and wind-tunnel studies on unsteady flow characteristics that stabilize vehicle behavior. *SAE Int. J. Passeng. Cars – Mech. Syst.*, 2(1):138–156, 2009.

[78] Akira Okubo. Horizontal dispersion of floatable particles in the vicinity of velocity singularities such as convergences. *Deep Sea Research and Oceanographic Abstracts*, 17(3):445 – 454, 1970.

[79] OpenFOAM Foundation. *OpenFOAM 2.2.2 - Programmer's Guide*, 2.2.2 edition, 2013.

[80] Alan V. Oppenheim, Ronald W. Schafer, and John R. Buck. *Discrete-time Signal Processing (2Nd Ed.)*. Prentice-Hall, Inc., Upper Saddle River, NJ, USA, 1999.

[81] Carsten Othmer. Adjoint methods for car aerodynamics. *Journal of Mathematics in Industry*, 4:6, 2014.

[82] Karl Pearson. Liii. on lines and planes of closest fit to systems of points in space. *Philosophical Magazine Series 6*, 2(11):559–572, 1901.

[83] M. Peichl and T. Indinger. Modal investigation of the flow around a generic car. *Haus der Technik (HDT), Munich, Germany*, 2014.

[84] M. Peichl, S. Mack, T. Indinger, and F. Decker. Numerical investigation of the flow around a generic car using dynamic mode decomposition. *Proceedings of the ASME 2014 Fluids Engineering Summer Meeting, Chicago, USA*, 2014.

[85] Armin Pobitzer, Ronald Peikert, Raphael Fuchs, Benjamin Schindler, Alexander Kuhn, Holger Theisel, Krešimir Matković, and Helwig Hauser. The state of the art in topology-based visualization of unsteady flow. *Computer Graphics Forum*, 30(6):1789–1811, 2011.

[86] Tamas Regert and Tamas Lajos. Description of flow field in the wheelhouses of cars. *International Journal of Heat and Fluid Flow*, 28(4):616 – 629, 2007.

[87] W. Rodi, J.H. Ferziger, M. Breuer, and M. Pourquié. Status of large-eddy simulation: Results of a workshop. *Journal Fluids Engineering*, 119:248–262, 1997.

[88] Martin Roth. *Automatic Extraction of Vortex Core Lines and Other Line-Type Features for Scientific Visualization*. PhD Dissertation No. 13673, ETH Zurich, 2000. published by Hartung-Gorre Verlag, Konstanz, ISBN 3-89649-582-8.

[89] C. W. Rowley, I. Mezic, S. Bagheri, P. Schlatter, and D. S. Henningson. Spectral analysis of nonlinear flows. *Journal of Fluid Mechanics*, 641:115–127, 2009.

[90] Christopher L. Rumsey. Turbulence model behavior in low reynolds number regions of aerodynamic flowfields. *AIAA Journal*, 47(4):982–993, 2009.

[91] P. Sagaut, S. Deck, and M. Terracol. *Multiscale and Multiresolution Approaches in Turbulence*. Imperial College Press, 2nd edition edition, 2013.

[92] Peter J. Schmid. Dynamic mode decomposition of numerical and experimental data. *Journal of Fluid Mechanics*, 656:5–28, 2010.

[93] Thomas Schütz, editor. *Hucho - Aerodynamik des Automobils*. Springer Vieweg, 6 edition, 2013. pp. 262.

[94] Kishan B. Shah and Joel H. Ferziger. A fluid mechanicians view of wind engineering: Large eddy simulation of flow past a cubic obstacle. *Journal of Wind Engineering and Industrial Aerodynamics*, 67 68(0):211 – 224, 1997. Computational Wind Engineering.

[95] M. L. Shur, P. R. Spalart, M. Strelets, and A. K. Travin. Detached-eddy simulation of an airfoil at high angle of attack. *Engineering Turbulence Modelling and Experiments*, 4:669–678, 1999.

[96] L. Sirovich. Turbulence and the dynamics of coherent structures parts i–iii. *Q. Appl. Math.*, 45(3):561–590, 1987.

[97] P. R. Spalart and S. R. Allmaras. A one-equation turbulence model for aerodynamic flows. *AIAA Paper*, 92-0439, 1992.

[98] P. R. Spalart, W.-H. Jou, M. Strelets, and S. R. Allmaras. Comments on the feasibility of les for wings and on a hybrid rans/les approach. *Advances in DNS/LES*, pages 137–147, 1997.

[99] Philippe R. Spalart. Detached-eddy simulation. *Annual Review of Fluid Mechanics*, 41(1):181–202, 2009.

[100] P.R. Spalart, S. Deck, M.L. Shur, K.D. Squires, M.Kh. Strelets, and A. Travin. A new version of detached-eddy simulation, resistant to ambiguous grid densities. *Theoretical and Computational Fluid Dynamics*, 20(3):181–195, 2006.

[101] D. B. Spalding. A single formula for the "law of the wall". *Journal of Applied Mechanics*, 28:455–458, 1961.

[102] R. K. Strachan, K. Knowles, and N. J. Lawson. The vortex structure behind an ahmed reference model in the presence of a moving ground plane. *Experiments in Fluids*, 42(5):659–669, 2007.

[103] A. Thacker, S. Aubrun, A. Leroy, and P. Devinant. Effects of suppressing the 3d separation on the rear slant on the flow structures around an ahmed body. *Journal of Wind Engineering and Industrial Aerodynamics*, 107-108:237 – 243, 2012.

[104] T. Theodorsen. Mechanism of turbulence. *Proceedings of the Midwestern Conference on Fluid Mechanics, Ohio State University, Columbus, OH*, 1952.

[105] C. Truesdell and W. Noll. *The Non-Linear Field Theories of Mechanics*. Springer-Verlag Berlin Heidelberg, 2004.

[106] J. H. Tu. *Dynamic mode decomposition: theory and applications*. PhD thesis, Princeton University, 2013.

[107] G. Vino, S. Watkins, P. Mousley, J. Watmuff, and S. Prasad. Flow structures in the near-wake of the ahmed model. *Journal of Fluids and Structures*, 20(5):673 – 695, 2005.

[108] X. W. Wang, Y. Zhou, Y. F. Pin, and T. L. Chan. Turbulent near wake of an ahmed vehicle model. *Experiments in Fluids*, 54(4):1–19, 2013.

[109] John Weiss. The dynamics of enstrophy transfer in two-dimensional hydrodynamics. *Physica D: Nonlinear Phenomena*, 48(2):273 – 294, 1991.

[110] H. G. Weller, G. Tabor, H. Jasak, and C. Fureby. A tensorial approach to computational continuum mechanics using object-oriented techniques. *Computers in Physics*, 12(6):620–631, 1998.

[111] G. Wickern and N. Lindener. The audi aeroacoustic wind tunnel: Final design and first operational experience. *SAE Technical Paper*, 2000-01-0868, 2000.

[112] J. Zhou, R. J. Adrian, S. Balachandar, and T. M. Kendall. Mechanisms for generating coherent packets of hairpin vortices in channel flow. *Journal of Fluid Mechanics*, 387:353–396, 1999.